



**INTERNATIONAL EFFICIENCY CHALLENGE  
ELECTRIC VEHICLE**

**TECHNICAL DESIGN REPORT**  
*Deadline: August 4<sup>th</sup>, 2021*

**VEHICLE AND TEAM NAME: ISTIKLAL – ULUDAG ELEKTROMOBİL TEAM**

**UNIVERSITY: BURSA ULUDAG UNIVERSITY**

**ACADEMIC ADVISOR, IF ANY:**

**TEAM CAPTAIN: CAGATAY ÇAKMAK**

**VEHICLE TYPE:    X ELECTROMOBILE     HYDROMOBILE**

## CONTENT

<b>Vehicle and Team Name: Istiklal .....</b>	<b>1</b>
<b>University: Bursa Uludag University.....</b>	<b>1</b>
<b>Academic Advisor, if any:.....</b>	<b>1</b>
<b>Team Captain: Cagatay Çakmak .....</b>	<b>1</b>
<b>1. Vehicle Specifications Table.....</b>	<b>8</b>
<b>2. Vehicle Dynamic Testing .....</b>	<b>9</b>
<b>3. Domestic Sub-Components.....</b>	<b>9</b>
<b>4. Motor.....</b>	<b>10</b>
4.1. Electrical Design and Analysis.....	11
4.2. Magnetic Design and Analysis.....	16
4.3. Mechanical Design and Analysis .....	18
4.4. Production studies .....	20
<b>5. Motor Driver .....</b>	<b>25</b>
5.1. Circuit Design .....	25
5.1.1. MOSFET gate driver.....	25
5.1.2. Current sense .....	26
5.1.3. Voltage sense.....	26
5.1.4. Capacitor bank.....	27
5.1.5. Hall sensor.....	27
5.1.6. Temperature sensor .....	27
5.1.7. Isolated CAN Communication.....	28
5.2. Control Algorithm .....	28
5.3. Power Efficiency .....	30
5.4. Simulation Studies .....	31
5.4.1. Inverter Simulation.....	31
5.4.2. Simulation of Isolated Current Sense .....	35

5.4.3. Simulation of Isolated Voltage Sense .....	36
5.4.4. Simulation of Gate Driver.....	37
5.5. Cost Table .....	38
5.6. PCB Design .....	38
5.7. Comparison Table .....	40
<b>6. Battery Management System (BMS) .....</b>	<b>41</b>
6.1. Circuit Designs.....	41
6.1.1. Microprocessor Selection.....	41
6.1.2. VDD-VDDA LC Filter .....	42
6.1.3. Cell Voltage Reading Circuit .....	43
6.1.4. Temperature Measurement .....	44
6.1.5. Cooling Fan .....	45
6.1.6. Isolated CAN Communication Protocol.....	46
6.2. Cell Balancing Method.....	47
6.3. DC to DC Converters.....	48
6.3.1. Isolated DC to DC Converter .....	48
6.3.2. Voltage Regulator .....	48
6.4. Control Algorithm .....	49
6.5. PCB Designs .....	49
<b>7. Embedded Recharging Unit.....</b>	<b>52</b>
7.1. Circuit Design .....	52
7.1.1. EMI Filter .....	52
7.1.1.1. Differential Mode.....	52
7.1.1.2. Common Mode .....	53
7.1.2. Active PFC.....	53
7.1.3. Full Bridge Converter.....	55
7.1.3.1. ZVS Control Topology .....	56
7.1.3.2. Dead Time .....	57
7.1.3.3. Transformer Calculations.....	57

7.1.3.4. Secondary Side Calculations .....	58
7.1.3.5. Output Choke Calculation .....	58
7.1.3.6. Voltage and Current Measures .....	58
7.1.4. Predrive Card.....	60
7.1.5. Control Card .....	61
7.1.5.1. Microprocessor Selection.....	61
7.1.5.2. Isolated CAN Communication .....	61
7.1.5.3. Isolated UART Communication.....	62
7.1.6. Control Algorithm .....	62
7.2. Simulation Studies .....	64
7.2.1. EMI Filter .....	64
7.2.2. Full Bridge Rectifier .....	65
7.2.3. DC-DC Converter Card.....	66
7.3. Production Studies.....	68
7.4. Test Results.....	69
7.5. PCB Designs .....	69
<b>8. Energy Management System .....</b>	<b>71</b>
<b>9. Battery Packaging .....</b>	<b>72</b>
9.1. Properties of Cells .....	72
9.1.1. Electrical Properties of Cells .....	72
9.1.2. Thermal Properties of Cells .....	72
9.1.3. Mechanical Properties of Cells .....	73
9.2. Battery Pack Features .....	73
9.3. Material Specifications of Battery Pack.....	74
9.3.1. Electrical Characteristics of Battery Pack Material.....	74
9.3.2. Thermal Properties of Battery Pack Material .....	74
9.3.3. Mechanical Properties of Battery Pack Material .....	75
9.4. Layout and Isolation of Modules and Package .....	76
9.5. Battery Cooling System Design .....	77
9.6. Precharge Circuit Design.....	78

<b>10. Electronic Differential Application .....</b>	<b>79</b>
10.1. Reading steering wheel angle information .....	79
10.2. Reading accelerator pedal information .....	79
10.3. Analog Signal Generation for Motor Drivers .....	80
10.4. Control Algorithm .....	81
10.5. PCB Design .....	81
10.5.1. Electronic Differential Mechanical Details .....	81
<b>11. Vehicle Control Unit (VCU).....</b>	<b>85</b>
11.1. Main Control Card.....	85
11.1.1. Microcontroller Selection.....	85
11.1.2. Isolated CAN Communication.....	86
11.1.3. RF Communication with XBEE/LoRa/SIM808 .....	86
11.1.4. Isolated UART Communication.....	87
11.1.5. Regulators .....	88
11.1.6. In Car Monitor (Dashboard) .....	88
11.1.7. Control Algorithm .....	90
11.1.8. PCB Designs .....	91
11.2. VCU I/O Card.....	92
11.2.1. Input and Output .....	92
11.2.2. Analog Inputs.....	92
11.2.3. Digital Inputs.....	92
11.2.4. Digital Outputs .....	93
11.2.5. Regulators .....	93
11.2.6. PCB Designs .....	93
11.3. Telemetry.....	94
11.3.1. Regulators .....	94
11.3.2. SD Card.....	95
11.3.3. PCB Design .....	96
11.4. Energy meter .....	96
11.4.1. Microcontroller Selection.....	96
11.4.2. Isolated Voltage and Current Measurement .....	97

11.4.3. Isolated Power Supply for OPAMPs .....	98
11.4.4. DS3231 RTC and SD Card.....	98
11.4.5. Isolated UART Communication.....	99
11.4.6. Regulators .....	100
11.4.7. Control Algorithm .....	100
11.4.8. Production Studies.....	101
<b>12. Insulation Monitoring Device.....</b>	<b>101</b>
<b>13. Steering System.....</b>	<b>102</b>
13.1. Caster angle .....	102
13.2. Camber angle .....	102
13.3. King-pim angle.....	103
<b>14. Door Mechanism (optional).....</b>	<b>111</b>
<b>15. Mechanical Details.....</b>	<b>113</b>
15.1. Technical drawings .....	113
15.2. Outer shell production.....	118
15.3. Chassis Design.....	132
<b>16. Fuel Cell.....</b>	<b>138</b>
<b>17. Fuel Cell Control System .....</b>	<b>138</b>
<b>18. Vehicle Electric Scheme .....</b>	<b>138</b>
<b>19. Unique Design by Team .....</b>	<b>139</b>
19.1. Control Arm Made of Metal Reinforced Composite Material .....	139
19.2. Energy meter .....	142
19.2.1. Microcontroller Selection.....	142
19.2.2. Isolated Voltage and Current Measurement .....	143
19.2.3. Isolated Power Supply for OPAMPs .....	144
19.2.4. DS3231 RTC and SD Card.....	144
19.2.5. Isolated UART Communication.....	145

19.2.6. Regulators ..... 146  
19.2.7. Control Algorithm ..... 146  
19.2.8. Production Studies..... 147  
Comparison Table ..... 147  
19.3. Cost Calculation..... 148

## CONTENT

### 1. Vehicle Specifications Table

<b>Feature</b>	<b>Unit</b>	<b>Value</b>
<b>Length</b>	mm	3575
<b>Width</b>	mm	1600
<b>Height</b>	mm	1200
<b>Chassis</b>	material	6063 T6 Aluminum
<b>Shell</b>	material	Glass Fyber
<b>The brake system</b>	hydraulic disc, front, rear, hand brake	Hydraulic Disc
<b>Motor</b>	type	PM Synchronous Motor
<b>Motor driver</b>	self-designed, ready-made product	Self-designed
<b>Motor power</b>	kW	3
<b>Motor efficiency</b>	%	%96
<b>Engine weight</b>	kg	12
<b>Battery</b>	type	Li-ion
<b>Battery pack nominal voltage</b>	V	115,2
<b>Battery pack capacity</b>	Ah	26,4
<b>Battery pack Maximum voltage</b>	V	115,2
<b>Battery pack energy</b>	Wh	3041
<b>Fuel cell power</b>	kW	
<b>Number of hydrogen cylinders</b>	#	
<b>Hydrogen cylinder pressure</b>	bar	
<b>Super capacitor</b>	yes/no	No
<b>You must fill in the fields related to your category.</b>		

## 2. Vehicle Dynamic Testing

<https://www.youtube.com/watch?v=BXEXunprihg>

## 3. Domestic Sub-Components

<b>Motor</b>	<b>Mandatory for Electromobile/Hydromobile</b>	<b>X</b>
<b>Motor driver</b>	<b>Mandatory for Electromobile/Hydromobile</b>	<b>X</b>
<b>Battery management system (BMS)</b>	<b>Mandatory for Electromobile/Hydromobile</b>	<b>X</b>
<b>Embedded recharging unit</b>	<b>Mandatory for Electromobile</b>	<b>X</b>
<b>Energy management system (EMS)*</b>	<b>Mandatory for Hydromobile</b>	<input type="checkbox"/>
<b>Battery packaging</b>	<b>Optional</b>	<b>X</b>
<b>Electronic differential application</b>	<b>Optional</b>	<b>X</b>
<b>Vehicle control unit (VCU)</b>	<b>Optional</b>	<b>X</b>
<b>Fuel cell*</b>	<b>Optional</b>	<input type="checkbox"/>
<b>Fuel cell control system (circuit)*</b>	<b>Optional</b>	<input type="checkbox"/>
<b>Insulation monitoring device</b>	<b>Optional</b>	<input type="checkbox"/>
<b>Steering system</b>	<b>Optional</b>	<b>X</b>
<b>Door mechanism</b>	<b>Optional</b>	<b>X</b>

\* Hydromobile category only

#### 4. Motor

One of the most basic parts of electric vehicles is the electric motor. The electric motor, where the electromagnetic energy conversion takes place, is seen as the component that most affects the performance and efficiency of the system. Therefore, determining the appropriate electric motor is an important issue in the design of electric motor driven vehicles. The parameters needed were determined before selecting the motor type. A literature review was conducted on motor types suitable to the specified parameters. As a result of the studies and literature research, it was decided to use the type of permanent magnet synchronous motor (PMSM). The copper losses are low and their efficiency is high, since there is no winding in the rotor of permanent magnet motors. Due to the permanent magnets in their structures, their energy density is higher. Motor types are given comparatively in Table 4.1. Considering the ease of installation of the selected motor type on the vehicle and the losses caused by the drivetrain, the outer rotor motor type was decided.

Table 4.1. Comparison of electric motors

	<b>Asynchronous Motor</b>	<b>Synchronous Motor</b>	<b>Direct Current Motor</b>	<b>ARM</b>	<b>SMSM</b>
<b>Input Voltage</b>	Alternative Voltage	Alternative Voltage	Direct Voltage	Direct Voltage	Direct Voltage
<b>Trigger Status</b>	No Trigger Required	Direct Voltage	Direct Voltage	No Trigger Required	No Trigger Required
<b>Driver</b>	Required in variable speed application.	Required in variable speed application.	Required in variable speed application.	Requires continuity.	Requires continuity.
<b>Operation and Maintenance Cost</b>	Very Low	Low	Medium	Very Low	Very Low
<b>Motor Cost</b>	Cheap	Expensive	Expensive	Cheap	Middle
<b>Driver Cost</b>	Expensive	Expensive	Middle	Middle	Middle
<b>Efficiency</b>	Good	Good	Middle	Good	Perfect
<b>Working Environment</b>	Works in all environment	Works in all environment	Not used in explosive environment	Works in all environment	Works in all environment
<b>Stability</b>	Good	Good	Good	Good	Good

#### 4.1. Electrical Design and Analysis

Design needs are determined before starting motor design. Target 10 kg motor and 2.8 kWh battery pack including the empty weight of 200 kg, Cd coefficient (vehicle aerodynamic coefficient) of 0.21, surface area 1.4 m<sup>2</sup>, Crr coefficient (coefficient of resistance formed on the road wheel) 0.015 and wheel diameter is 571.8 mm. Speed was obtained in line with these values and requirements. Forces on the vehicle; tire friction (Fr), bearing friction (Fb), drag force (Fw) and slope resistance if the vehicle is coming uphill. It should be ensured that the torque of the motor meets the forces acting on the vehicle at the maximum vehicle speed. Based on these forces and dynamic parameters of the vehicle, basic motor parameters such as required motor torque and power have been obtained. Since the motor will be designed as a hub motor, no differential ratio will be used. Therefore, the speed and torque required by the vehicle are the values that must be obtained directly at the output of the motor. The vehicle speed must be 60-70 km / h in order to take a 60 km road in about an hour. The motor speed was calculated as 620 rpm so that the vehicle could reach this speed value. The torque needed by the vehicle was calculated as 36 Nm. Two motors will be used on the vehicle.

A battery pack with a nominal voltage of 120 V was designed as a power source. In accordance with the needs, the rated output power of the motor is determined as 1.5 kW.

In the analytical design process, the main dimensions need to be determined based on the volumes on the vehicle and this process has been determined in accordance with Equation 4.1.

$$TRV = \frac{T}{\frac{\pi D^2 L}{4}} \tag{4.1}$$

TRV is the moment value that can be taken from a specific rotor volume. Its unit is kNm/m<sup>3</sup>. 'T' is the moment value. 'D' is the rotor diameter and 'L' is the rotor axial length. Moment values that can be taken from a specific rotor volume are given in Table 4.2. Motor height is 25 mm, motor outer diameter is 292 mm.

Table 4.2. TRV values by motor type

Class of machine	TRV kNm/m <sup>3</sup>
Small totally-enclosed motors (Ferrite magnets)	7 - 14
Totally-enclosed motors (sintered Rare Earth or NdFeB magnets)	14 - 42
Totally-enclosed motors (Bonded NdFeB magnets)	20
Integral-hp industrial motors	7 - 30
High-performance servomotors	15 - 50
Aerospace machines	30 - 75
Large liquid-cooled machines (e.g. turbine-generators)	100 - 250

When the relation between the electrical frequency of the motor and the mechanical rotation speed of the magnetic field, that is, the synchronous speed, is examined, it is seen that the number of poles and the rotation speed of the motor are inversely proportional.

$$n_s = 120 \cdot f / 2p \quad (4.2)$$

Therefore, while high speed motors are usually manufactured with 2 to 4 poles, the number of poles should be selected high for the motor to be used in an application that requires low speed and high moment. The number of pole pairs is determined as 14. The magnet thickness to be used can generally be preferred as 10 times the air gap.

The air gap is another parameter to be determined, the typical radial air gap length for synchronous motors is given in Equation 4.3. From equation 4.3, the air gap length ( $\delta$ ) was obtained as 0.5 mm.

$$\delta = k \cdot \tau_{kutup} \cdot \frac{A_s}{b_\delta} \quad (4.3)$$

The stator core is produced by pressing a 0.3-0.5 mm thick laminated silicon steel sheet, in order to reduce the circulation current, and the slots on which the conductors are placed are opened. The number of stator slots is determined depending on the rotor poles, the number of phases and the winding shape. Number of stator slots;

$$N_s = P \cdot m \cdot q \quad (4.4)$$

' $N_s$ ' slot number, 'm' phase number, 'q' is the number of slots per pole-phase. The number of phases is 3, the number of poles and the number of slots per pole-phase is 0.7, where the number of slots is 30. In SMPM motors, it is possible to use circular and rectangular slot types depending on slot number and winding structure. In the manufacture of the winding, the slot occupancy rates were taken into consideration in order to fit the windings into the slots, the slot height, slot tooth thickness, conductor cross sections and current densities were determined accordingly. Equal length gutter teeth and open gutter mouth are used for ease of production.

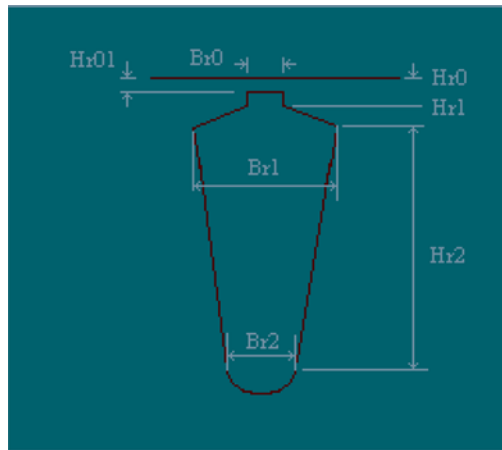


Figure 4.1. Slot Structure

Winding is an important parameter for the motor. The copper losses from the losses in the motor disappear over the windings here. The greater the winding resistance, the greater the copper losses. Winding length should be determined for winding resistance. The average length of a winding is calculated from approximately equation 4.4.

$$l_{mt} = 2L + 2,3\tau_p + 0,1 \text{ (m)} \quad (4.5)$$

There are different combinations of pole and slot number in the motor as well as winding shapes. The windings should be symmetrical to avoid unbalanced magnetic attraction. In this context, the shape of the winding we consider; For the 3 phase motor, the form of winding is preferred, with all slots full and the number of slots is 3 times, each coil has an equal number of turns, so each phase has the same resistance and inductance. Winding types were examined to determine the winding type of the windings. With the concentric winding, the volume of the coil ends is reduced, so that the area actively used increases and has a higher power density than the distributed winding. Efficiency is particularly high at low speeds (when copper losses are higher than core losses) when using concentric winding. However, at high speeds, iron core losses are proportional to the square of the frequency and the flux density passing through the iron, so it is not beneficial to reduce copper losses by using concentric winding and efficiency decreases. The concentric winding offers low knock moment, low iron core losses and contributes to the stator being wrapped piece by piece afterwards. A lower knock moment and moment fluctuation occurs in the fractional slot winding, but the average moment acquisition decreases, and the fractional number of slots per pole increases harmonic components. In concentric wound motors, the length of the winding head is 1/3 shorter compared to conventional wound motors with the same slot number. Therefore, the motor becomes lighter as the copper volume decreases, the copper losses decrease and the efficiency increases due to the decrease in the conductor length

and the conductor resistance. In low speed-high moment applications where copper losses are dominant, the use of concentric-wound permanent magnet motors is seen as a solution. In addition, reducing the volume of copper, which is an expensive material, in the motor will provide a great advantage in terms of cost. In Figure 4.2, overflow amounts occurring at the winding heads are compared according to the winding types.

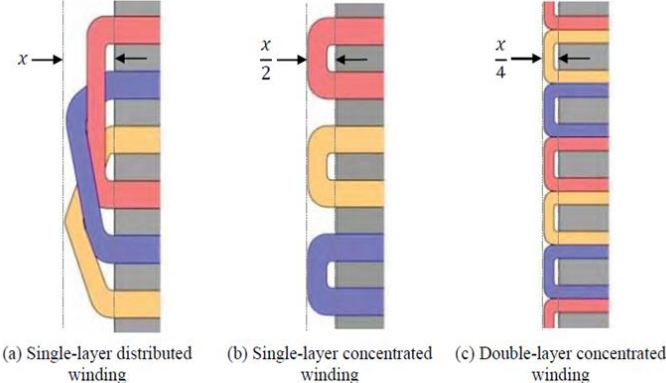


Figure 4.2. Estimated Reduction In End Winding Length

To reduce copper losses, it is necessary to reduce phase resistances. The phase resistance can be reduced by increasing the conductor cross section, by making an intermittent winding or by reducing the number of turns. However, when the conductor cross section is increased, the current density will decrease. The number of turns of a phase is calculated by the expression given in Equation 4.5 and it is obtained as 13 turns. The winding shape is shown in Figure 4.3.

$$w_a = E / \frac{2\pi}{\sqrt{2}} \cdot k_{w1} \cdot f \cdot \Phi \tag{4.6}$$

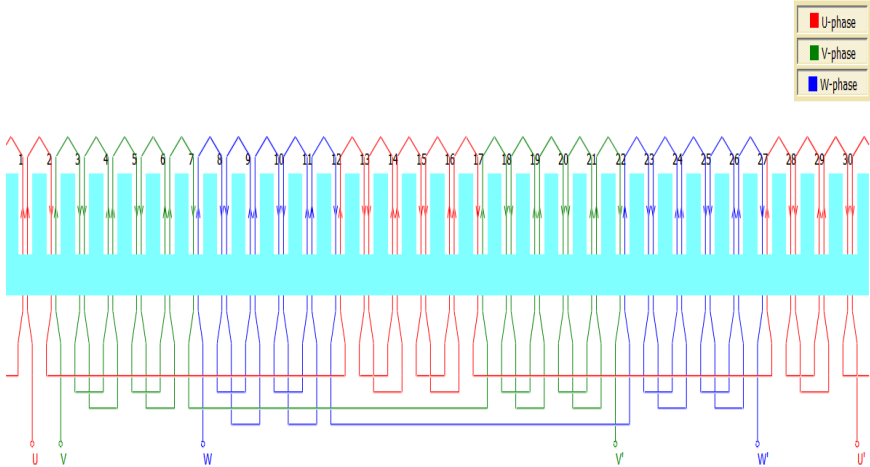


Figure 4.3. Slot Diagram

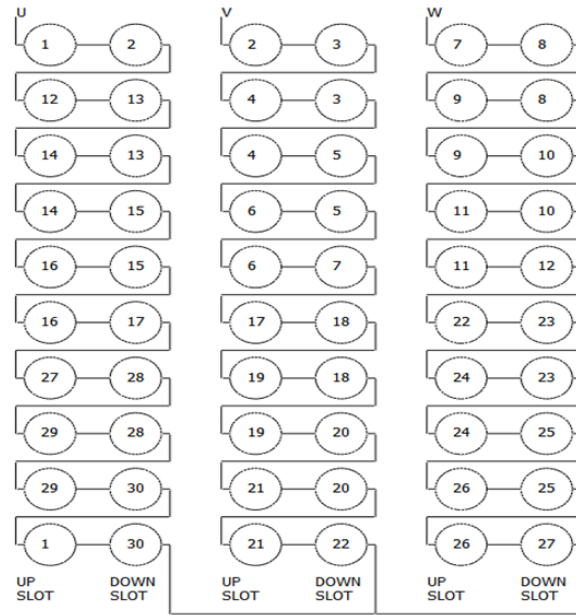


Figure 4.4. Winding Diagram

After analyzing the motor's analytical calculations and design parameters, JMAG-Designer, one of the commercial prepackage programs, was used in the numerical analysis of the model created.

The backemf value that occurs when the motor rotates at 620 RPM is shown in Figure 4.5. The maximum value in the graph is the rms value of the resulting voltage.

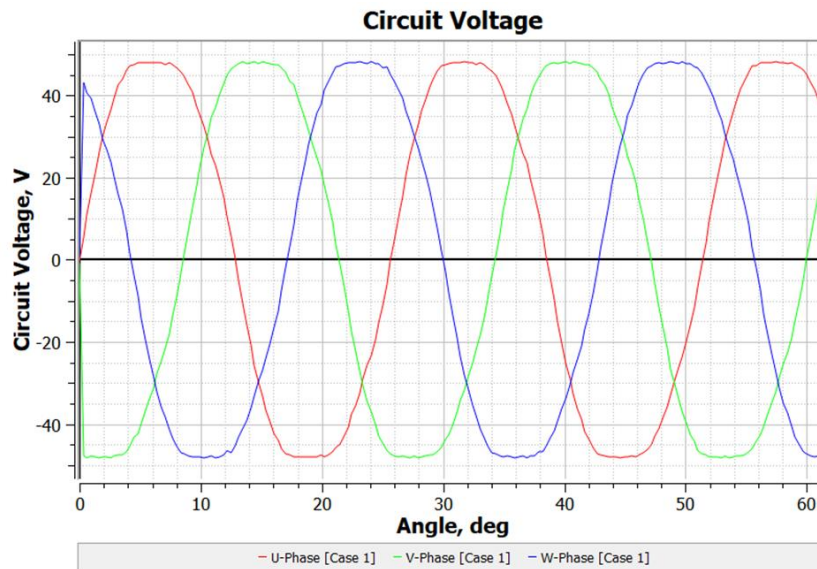


Figure 4.5. Circuit Voltage

In motors with three-phase sinusoidal opposite-EMK, the torque fluctuation should not exceed 15%. Torque vibrations and cogging moment are shifting the stator sheet package or rotor shocking area at an angle, gutter opening, concentric and fractional gutter pitched winding etc. can be reduced by design approaches or software active control structures. The cogging moment graph is given in Figure 4.7.

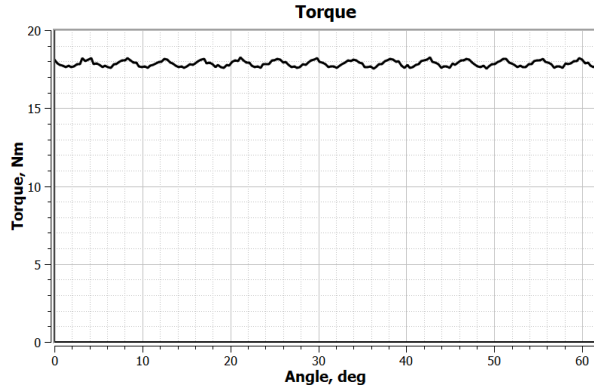


Figure 4.6. Torque

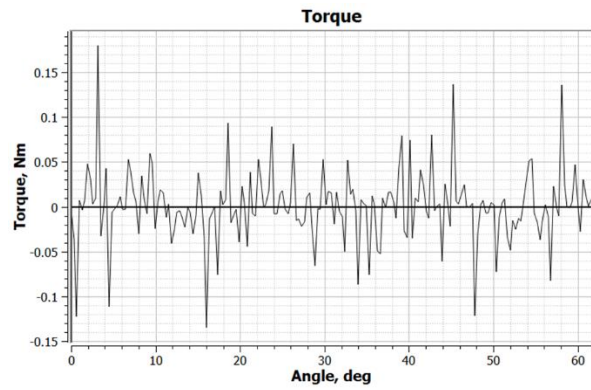


Figure 4.7. Cogging Torque

## 4.2. Magnetic Design and Analysis

After the electrical design was completed, magnetic analysis was performed in the model Jmag Designer. Material selection is an important factor in magnetic analysis. In order to keep the iron losses at a low level, the best quality sheet metal material is preferred. A quality sheet material is a motor sheet which has a small loss of iron, which can generate large magnetic flux density at low magnetic field strength. Therefore, the magnetic permeability of the sheets is high. M330-35A type sheet material with a thickness of 0.35 mm was used in the designs.

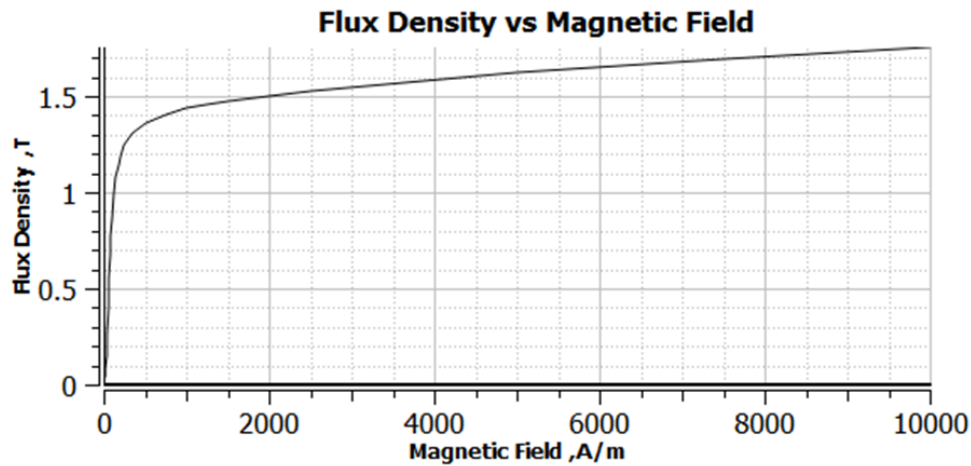


Figure 4.8. B/H Curve

Along with improvements in material and production technology, the energy intensities of permanent magnets are increasing and their use in electric motors is becoming widespread. Various permanent magnet materials such as AlNiCo, ferrite, SmCo, NdFeB are widely used for electric motors. Although AlNiCo magnets provide high flux density and Curie temperature advantages, they limit magnet placement due to the low coercive value. Ferrite magnets can withstand high temperatures due to their ceramic structure. In addition, they are often preferred for low cost motor production because of their low cost and durability. On the other hand, AlNiCo and NdFeB magnets, which are rare earth elements, are expensive materials, but they are preferred for high performance applications because they can provide high flux density and field strength. Demagnetization in the SMPM motor is due to the effect of the magnetic field generated by the current flowing through the stator windings of the current supplied by the permanent magnets on the track. B/H curves of magnet materials are given comparatively in Figure 4.9. Among the NdFeB type permanent magnets, the N35 type magnet produced by Arnold was chosen.

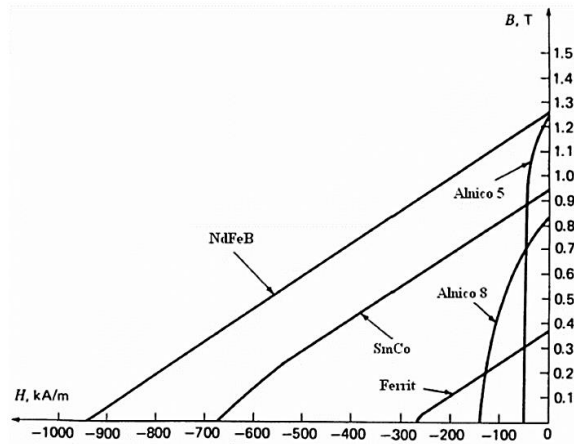


Figure 4.9. Magnet B/H Curve

In the Jmag Designer program, the magnetic analysis of the motor was performed using FEM (finite element method) analysis. Figure 4.10 and Figure 4.11 shows how the magnetic flux will follow on the motor geometry and the amount of magnetic field that will form in the stator core.

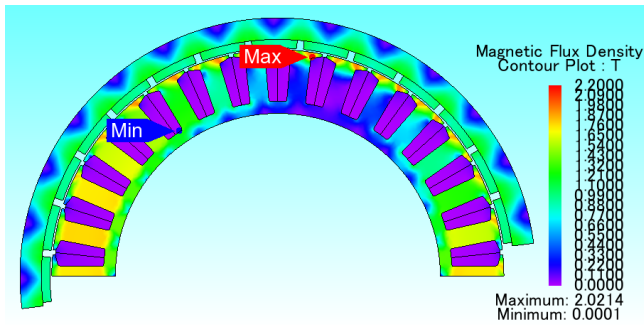


Figure 4.10. Magnetic Flux Density Distribution

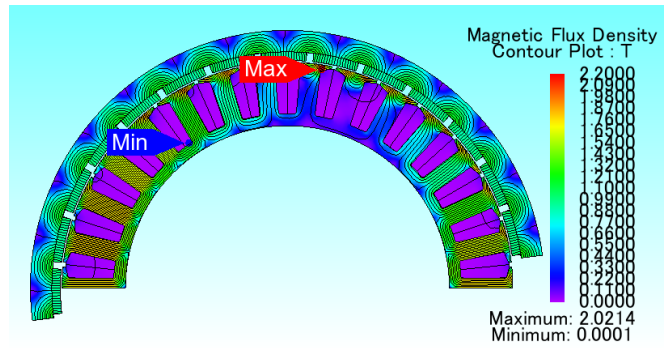


Figure 4.11. Magnetic Flux Density Distribution and Magnetic Flux Line

### 4.3. Mechanical Design and Analysis

The motor cover also acts as a rotor. Since the motor is a constantly rotating part, it is constantly exposed to vibration. Therefore, the first frequency value should be calculated so that the part does not resonate.

As shown in Figure 4.12, a mass has been added to the center of gravity of the other parts associated with the cover, as the modal analysis model is considered to be supported by the rim connection parts. As a result of the analysis, a large initial frequency value of 321 Hz was obtained.

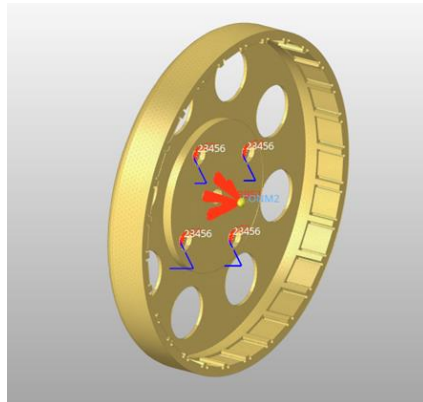


Figure 4.12. Motor Cover Modal Analysis Model

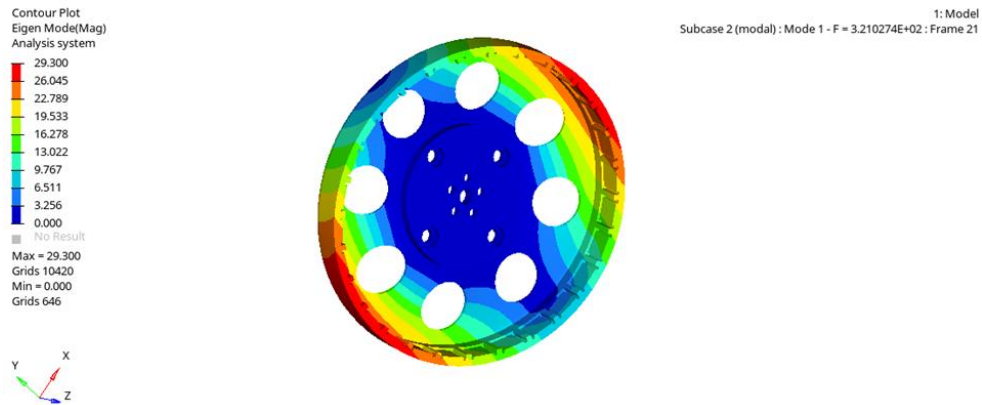


Figure 4.13. Modal Analysis Result

A static analysis was performed on the motor shaft and the engine cover. The motor shaft is connected to the cover with 5 holes M8. Stress value and amount of deformation formed by applying a force of 1500 N to force the shaft to bend were examined. These values are in Figure 4.15. The part has been found to be safe according to the resulting stress value.

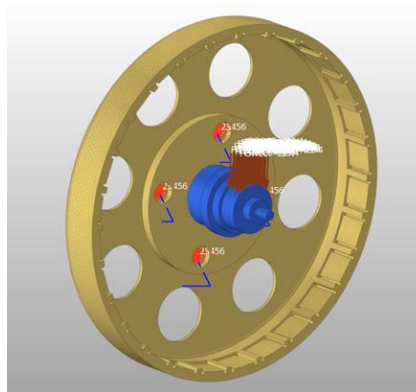


Figure 4.14. Static Analysis Model

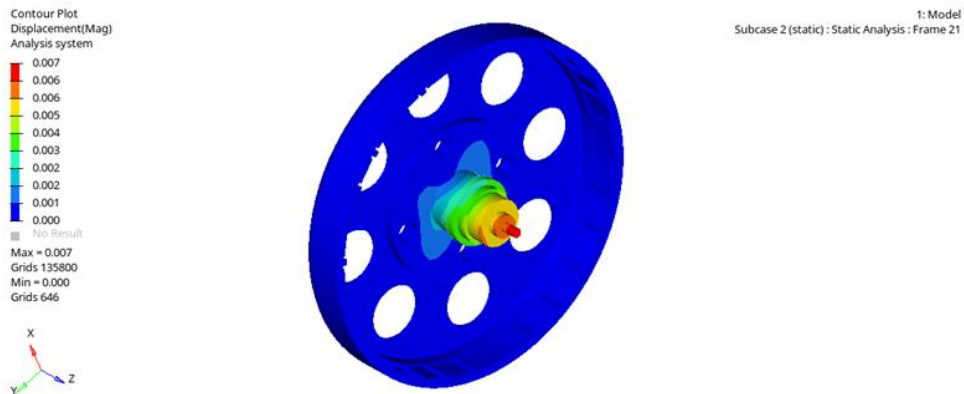


Figure 4.15. Static Analysis Displacement

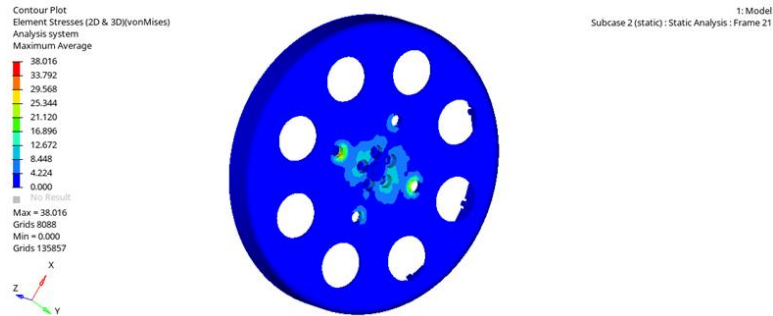


Figure 4.16. Static Analysis Von Mises Stress



Figure 4.17. Motor Assembly Design

#### 4.4. Production studies

We assembled 0.35mm thick steel sheets cut with wire erosion and turned them into stators. The bearing housings and connection parts required for the bearing of the motor were produced using cnc lathe and cnc milling machines in accordance with the designs. Before the coil winding process, the centering problems that occurred during the assembly of the stator sheets with the help of a grinding machine were eliminated and the coil was made ready for the winding process.



Figure 4.18.



Figure 4.19.



Figure 4.20.

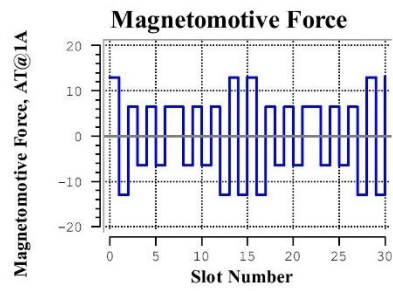
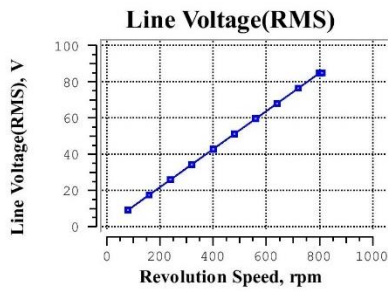
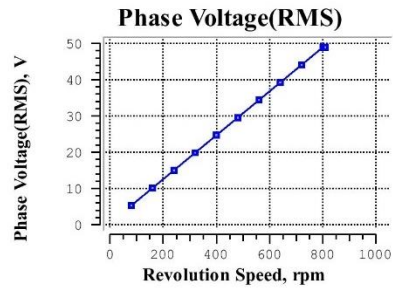
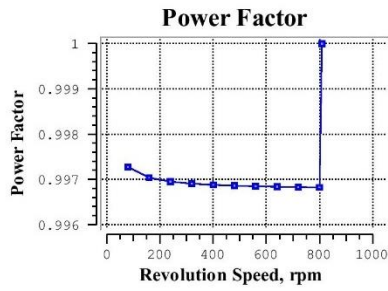
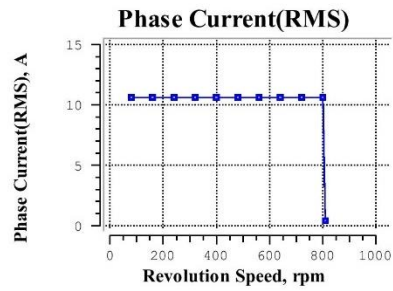
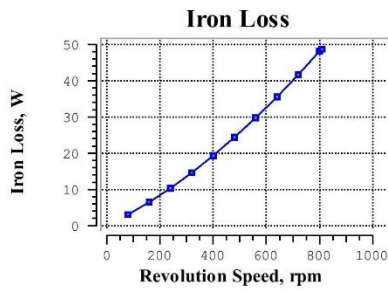
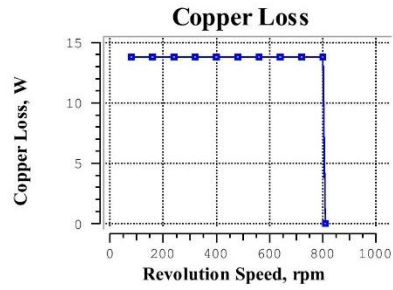
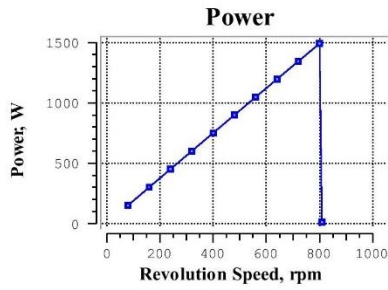
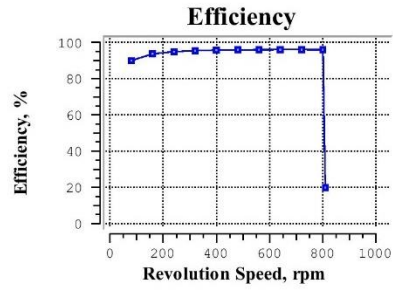
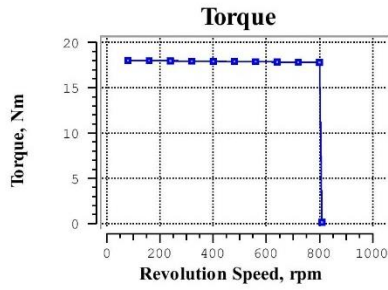


Figure 4.21. Motor Design Features Charts

Machine Constant		
Revolution Speed	N, rpm	800
Inductance	Ld, H	2.805e-04
	Lq, H	3.137e-04
	Self Inductance, H	1.981e-04
	Mutual Inductance, H	-9.903e-05
Torque Constant	Kt, Nm/A	1.258
Voltage Constant	Ke, V s/rad	1.452
Magnetic Circuit	Average Teeth Flux Density, T	1.072
	Average Back Yoke Flux Density, T	0.8414
	Average Gap Flux Density, T	0.7375
Electric Part	Phase Current(RMS), A	10.61
	Wire Current Density, A/mm <sup>2</sup>	1.929e+06
Power	Torque, Nm	17.8
	Efficiency, %	96.01
	Power, W	1491
	Power Factor	0.9968
Loss	Copper Loss, W	13.79
	Iron Loss, W	48.17
Electric Circuit	Phase Voltage(RMS), V	48.97
	Line Voltage(RMS), V	84.82
Dimension		
All	Outer Diameter, mm	300
	Gap Length, mm	1
	Stack Length, mm	25
inner_stator : si_011	Number of Slots	30
	Stator Outside Diameter, mm	263
	Stator Bore Diameter, mm	189
	Angle of Slot, deg	10.1
	Depth of Stator Slot, mm	30
	Width of Stator Slot-top, mm	15
	Width of Stator Slot-opening, mm	2.7
	Height of Stator Tooth-lang, mm	1.5
	Angle of Stator Tooth-lang, deg	20
	Filet Radius at Stator Slot-bottom, mm	1
	Filet Radius at Stator Slot-top, mm	1
spm_outer_rotor : rsp_104	Number of Poles	28
	Outside Diameter, mm	300
	Inside Diameter, mm	265
	Magnet Thickness, mm	5
	Magnet Interval, mm	4
	Magnet Corner R, mm	0.286
Materials		
Stator Core	Category	ArcekorMital
	Type	M330-35A
	Density, kg/m <sup>3</sup>	7650
Coil	Category	Copper
	Density, kg/m <sup>3</sup>	8960
	Temperature, degC	20
	Base Temperature, degC	20
Rotor Core	Temperature Correction Factor, ppm/degC	0
	Category	ArcekorMital
	Type	M330-35A
	Density, kg/m <sup>3</sup>	7650
	Category	Arnold - Nd-Fe-B Magnet
Rotor Magnet	Type	N35
	Temperature, degC	80
	Temperature Correction Factor, %/degC	0
	Magnetization Pattern	Parallel
Common Material Properties	Density, kg/m <sup>3</sup>	7500
	Iron Loss Correction Factor	1
Mass Property		
Total	Total Weight, kg	8.208
	Total Volume, mm <sup>3</sup>	1.023e+06
	Stator Core - Mass, kg	2.978
	Stator Core - Volume, mm <sup>3</sup>	3.893e+05
Stator	Coil - Mass, kg	2.381
	Coil - Volume, mm <sup>3</sup>	2.657e+05
	Part Weight(si_011)	5.359
	Rotor Core - Mass, kg	2.159
Rotor	Rotor Core - Volume, mm <sup>3</sup>	2.823e+05
	Rotor Magnet - Mass, kg	0.69
	Rotor Magnet - Volume, mm <sup>3</sup>	9.2e+04
	Part Weight(rsp_104)	2.849
Inertia, kg m <sup>2</sup>	Rotor Core	0.0447
	Rotor Magnet	0.01258
	Total	0.05728
Winding		
Connection Type	Star Connection	
Series Number		10
Parallel Number		1
Number of Turns		13
Setting Type	Round Wire Dimension	
Wire Diameter, mm		1
Film Thickness, mm		0
Number of Strands		7
Insulation Thickness, mm		0
Slot Fill Factor, %		40.54
Max Slot Fill Factor, %		75
Correction Factor		1
Slot Area, mm <sup>2</sup>		352.6
Conductor Area, mm <sup>2</sup>		10.21
Phase Resistance, ohm		0.04087
Winding	Auto Winding	
Number of Layers		2
Coil Pitch		1
Coil Current Density(@1A), A/mm <sup>2</sup>		0.1819
Drive		
Mode	Voltage(Sin)	
Line Voltage(Amp), V		120
Current Phase, deg		0
Maximum Line Current(Amp), A		15
X-axis	Revolution Speed, rpm	

Figure 4.22. Motor Design Features Tables

	Previous Design	Current Design
Motor Type	<b>PMSM</b>	<b>PSMS</b>
Motor Phase Voltage	<b>60</b>	<b>120</b>
Motor Power	<b>1.5KW</b>	<b>1.5KW</b>
Motor Speed	<b>720 RPM</b>	<b>720 RPM</b>
Motor Dimensions	<b>300mm</b>	<b>300mm</b>
Motor Weight	<b>8,208 kg</b>	<b>8,208 kg</b>
Motor Efficiency	<b>%96</b>	<b>%96</b>
Motor Main Dimension	<b>300mm</b>	<b>300mm</b>
Stator Dimension	<b>263mm</b>	<b>263mm</b>
Rotor Dimension	<b>300mm</b>	<b>300mm</b>
Winding Scheme	<b>Star</b>	<b>Star</b>
Motor Optimization	-	-
Magnetic Design and Analysis Model	<b>JMAG</b>	<b>JMAG</b>
Thermal Design and Analysis Model	-	-
Mechanical Design and Analysis Model	<b>ANSYS</b>	<b>ANSYS</b>
Motor Test Methods and Results	-	-

<https://we.tl/t-TOhk8561Vi>



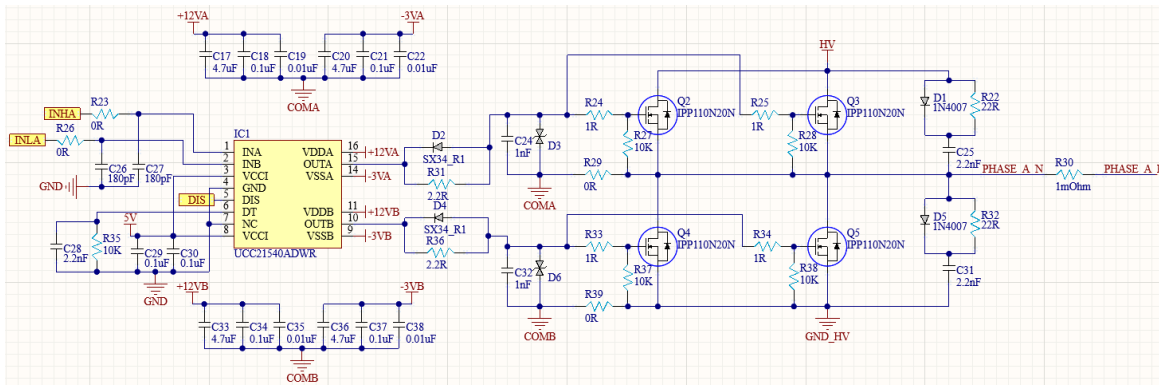


Figure 5.2. Half bridge MOSFET and MOSFET driver circuit

### 5.1.2. Current sense

AMC1301 is used for isolated current measurement. The power supply of this OPAMP is provided from the power supply of the gate drivers. The 12 volts from the driver were reduced to 5 volts with TL431. AMC1301 provides differential analog output. OPA4377 OPAMP is used to convert to single ended signal. 1.65 Volt reference is given to read negative currents. Detailed schematic and PCB files are attached as PDF file.

$$V_{shunt} = I_{phase} \times R_{shunt} \quad (5.1)$$

$$I_{phase} = \left(\frac{10K}{9.4K}\right) \times 8.2 \times V_{shunt} + 1.65 \quad (5.2)$$

The microcontroller operating range is between 0 -3.3 volts. The designed motor driver can easily read phase currents of more than  $\pm 50A$ .

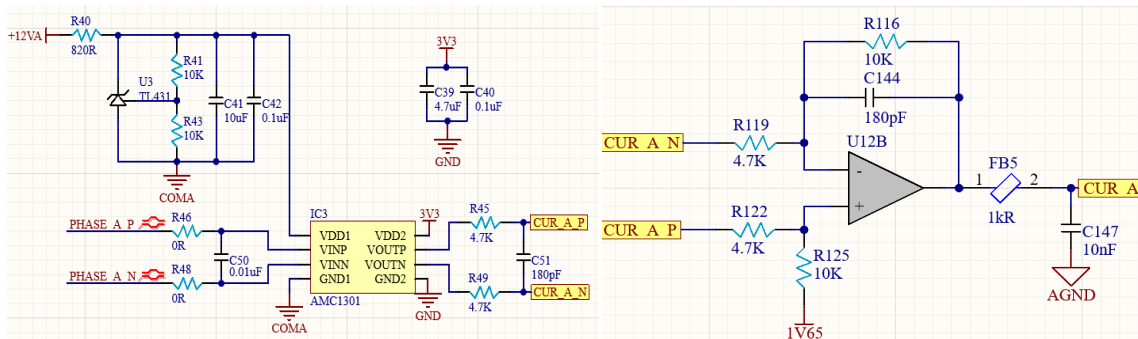


Figure 5.3. AMC1301 Current sense

### 5.1.3. Voltage sense

AMC1311 is used for isolated voltage measurement. The power supply of this OPAMP is provided from the power supply of the gate drivers. The 12 volts coming from the driver have been reduced to 5 volts with TL431. AMC1311 provides differential analog output. OPA4377 OPAMP is used to convert to single ended signal. 1.65 Volt reference is given to read negative voltage. Detailed schematic and PCB files are attached as PDF file.

$$V_{in} = V_{bus} \times \left(\frac{4.7K}{1M+4.7K}\right) + 1.65 \quad (5.3)$$

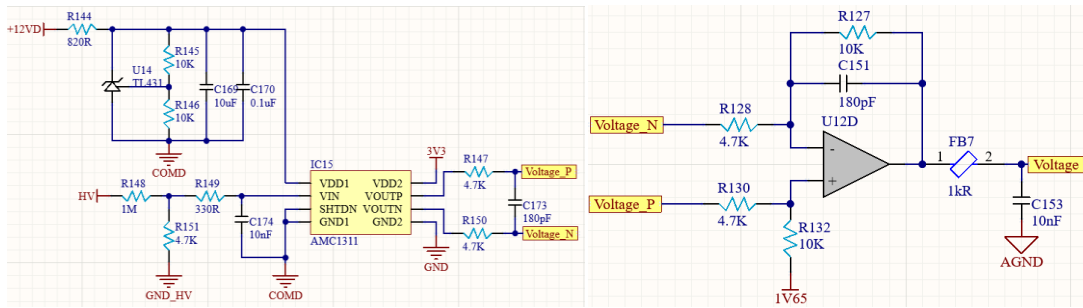


Figure 5.4. AMC1311 Voltage sense

### 5.1.4. Capacitor bank

100V 1000uF capacitors are used for motor driver capacitor bank. It is provided to work at 120V voltage by connecting in series. Total input capacity is 1500uF. 3 TVS diodes are connected in parallel to absorb transient voltages.

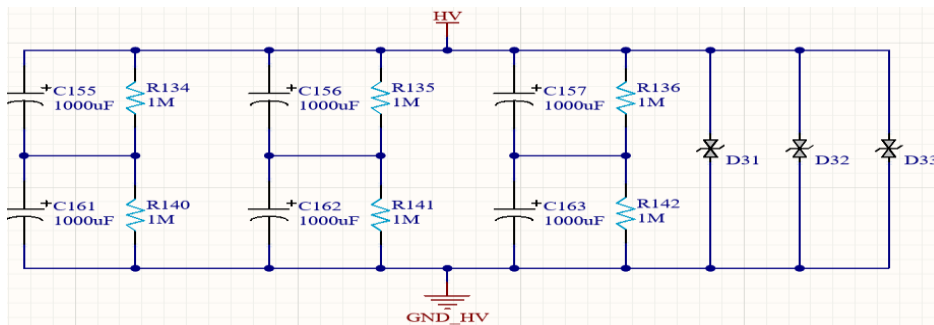


Figure 5.5. AMC1311 Capacitor bank

### 5.1.5. Hall sensor

UGN3177 hall sensors are used to read the motor position. A low pass filter was used as the input filter.

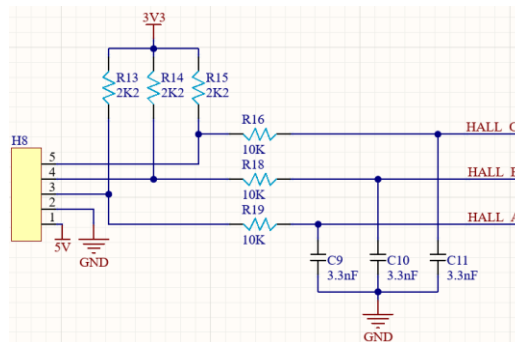


Figure 5.6. Hall sensor circuit

### 5.1.6. Temperature sensor

10 NTC sensors used to read temperature are read with the help of voltage divider. A low pass filter was used as the input filter. Air cooling system is used to dissipate the heat on the motor driver.

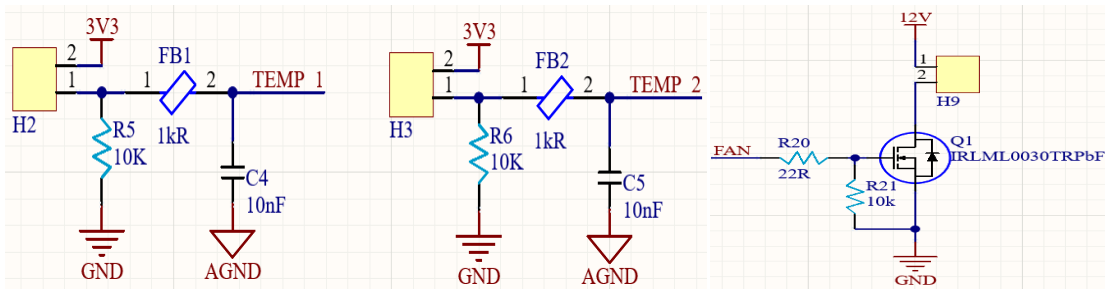


Figure 5.7. Temperature sensor and fan circuit

### 5.1.7. Isolated CAN Communication

Together with SN6505 transformer driver, isolated 760390012 SMPS transformer, TPS76350-Q1 voltage regulator, ISO1050 isolated CAN transfer IC, an isolated CAN communication system was created from other components of the card. The schematic of the mentioned CAN Communication circuit is shown in Figure 5.8.

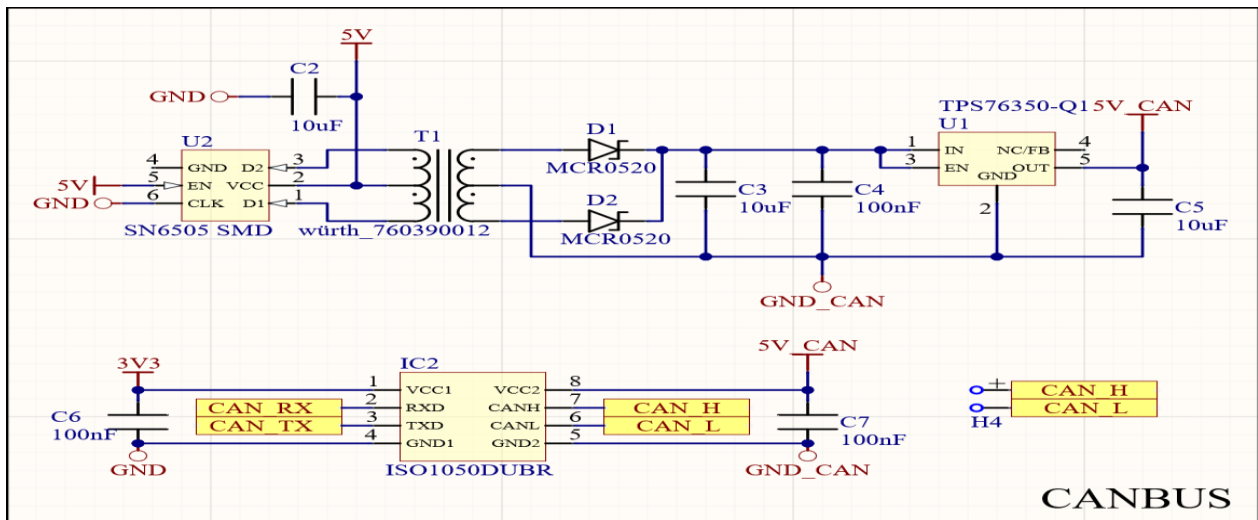


Figure 5.8. Isolated CAN Communication Schematic

### 5.2. Control Algorithm

STM32F302C8 microcontroller from STM32 series is used to control the motor driver. Thanks to the advanced timer in it, the complementary output is hardware-created. Another timer that reads the Hall sensors as a master, gives a command to the advanced slave timer.

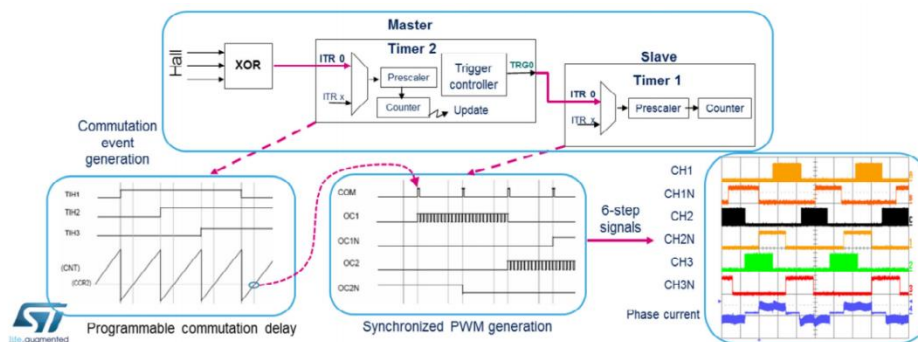


Figure 5.9. STM32 Timer link system

While the motor driver reads the signal from the accelerator pedal, the motor currents are read in connection with the timer. According to the motor position, the current can be read at twice the switching frequency from the shunt resistors in that position. The microcontroller has the ability to convert 5 MSPS ADC. Fast response of the driver in case of short circuit is possible thanks to this step-by-step current reading. In case of short circuit or over current draw, the inverter will trip.

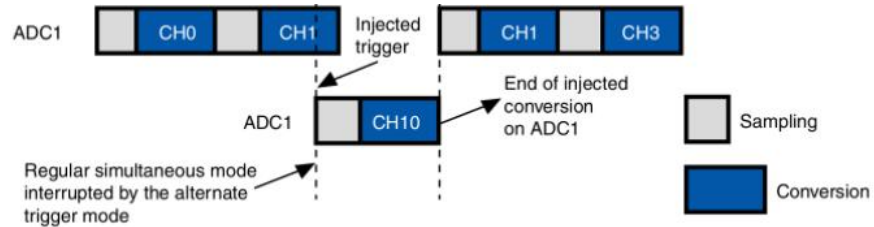


Figure 5.10. STM32 ADC injected system

Error codes have been created in order for the device to protect itself and give information to the outside. When the system fails, it generates an error code and informs the VCU via CAN BUS.

FAULT	ERROR CODE	DB LED BLINK
DRIVER_NO_ERROR	0x0000	0
DRIVER_OVER_VOLTAGE	0x0001	1
DRIVER_SHORT_CIRCUIT	0x0002	2
DRIVER_OVER_CURRENT	0x0003	3
DRIVER_OVER_TEMP	0x0004	4
DRIVER_UNDER_VOLTAGE	0x0005	5
DRIVER_HALL_SENSOR_ERR	0x0006	6
CANBUS_COMM_ERR	0x0007	7

Figure 5.11. Fault Code Table

The driver makes the presets when it is first opened. If the settings have been made successfully, it will start. If there are situations that will prevent the system from working, the system will crash and turn itself off.

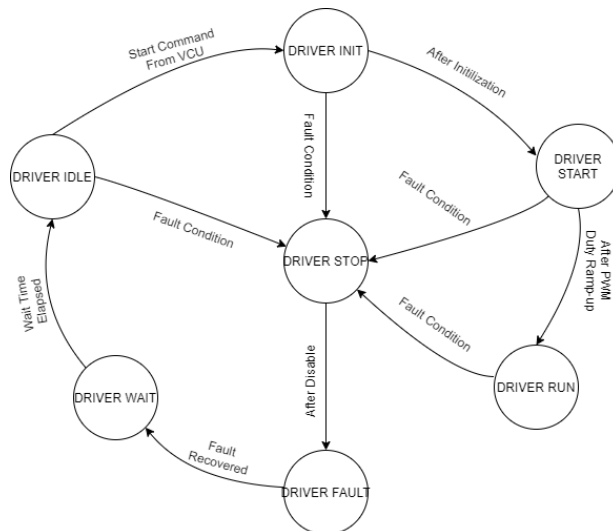


Figure 5.12. State Machine

ADC1 unit reads current and voltage while ADC2 unit reads temperature data. If the temperature is too high, the system will turn itself off again.

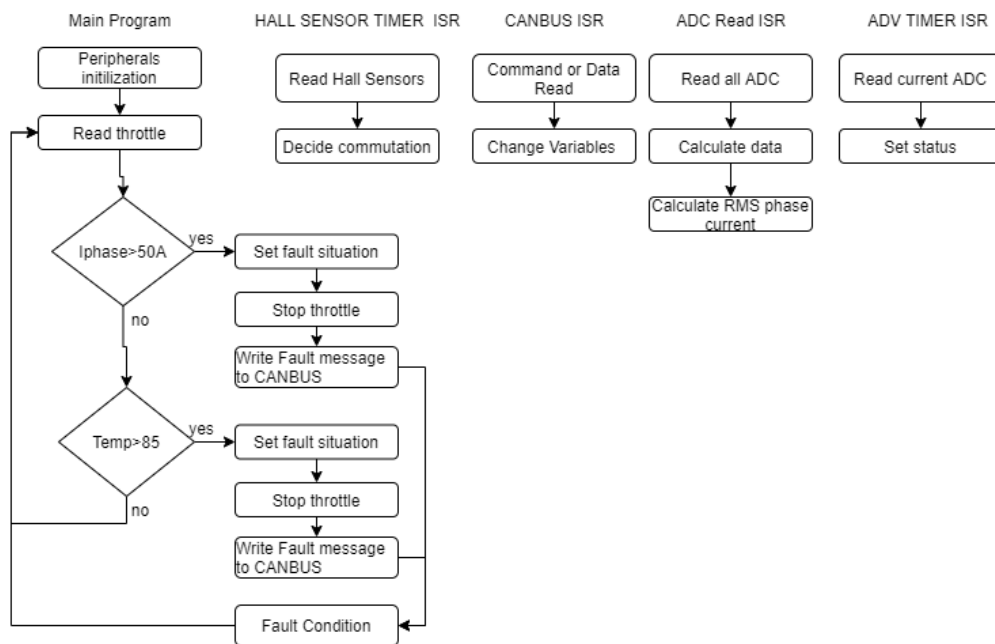


Figure 5.13. Control algorithm

### 5.3. Power Efficiency

The losses in the motor driver are the losses caused by the power switches. Two types of losses occur on MOSFETs. These are transmission losses and switching losses.

$$P_{loss} = P_{cond} + P_{on} + P_{off} \tag{5.4}$$

IPP110N20N3G MOSFET internal resistor  $R_{DS(on)} = 9.9m\Omega$  dur. When a maximum of 30 A continuous current is drawn, there are 2 parallel MOSFETs, and each MOSFET drops a current of 15A. If the High and Low side MOSFETs are taken into account together, the conduction losses are;

$$P_{cond} = I_{D(on)}^2 \times R_{DS(on)} \times D \quad (5.5)$$

$$P_{cond} = 4 \times 15A^2 \times 9.9m\Omega \times 0.9 = 8.01W \quad (5.6)$$

The high side MOSFET switches and the low side MOSFET on the other side stays on until the phase change. In this case, the switching losses are only seen on the high side MOSFET. In this case, for the switching losses;

$$P_{on} = I_{D(on)} \times V_{DD} \times \left(\frac{t_{fv}+t_{ri}}{2}\right) \times F_{sw} \quad (5.7)$$

$t_{fv}$  is the drain-source voltage drop time.  $t_{ri}$  is the rise time of the current flowing through the MOSFET. In this case, 50ns is taken for the rise and fall times experimentally. If calculated according to 2 parallel MOSFETs;

$$P_{on} = 2 \times 15A \times 120V \times \left(\frac{50ns+50ns}{2}\right) \times 20kHz = 3.6W \quad (5.8)$$

$$P_{off} = I_{D(on)} \times V_{DD} \times \left(\frac{t_{ri}+t_{fv}}{2}\right) \times F_{sw} \quad (5.9)$$

$t_{ri}$  is the rise time of the drain-source voltage.  $t_{fv}$  is the time for the current flowing through the MOSFET to fall. In this case, 50ns is taken for the rise and fall times experimentally. If calculated according to 2 parallel MOSFETs;

$$P_{off} = 2 \times 15A \times 120V \times \left(\frac{50ns+50ns}{2}\right) \times 20kHz = 3.6W \quad (5.10)$$

$$P_{loss} = 8.01W + 3.6W + 3.6W = 15.2W \quad (5.11)$$

Since the total losses are 15.2W and the total transferred power is 3600W;

$$P_{\%loss} = \left(\frac{15.2W}{3600W}\right) = \%0.42 \text{ olduğu görülmüştür.}$$

## 5.4. Simulation Studies

In this section, simulation results of inverter, gate driver, current and voltage measurement circuits of Motor Driver circuit were shown. Simulation and circuit analyzes were done in MATLAB Simulink and TINA. Detailed files are attached.

### 5.4.1. Inverter Simulation

Inverter simulation was performed using a 3-phase electric motor defined in MATLAB Simulink Electrical program. It is adjusted according to the parameters of the electric motor designed for the selected motor. The motor parameters were shown in Figure 5.14.

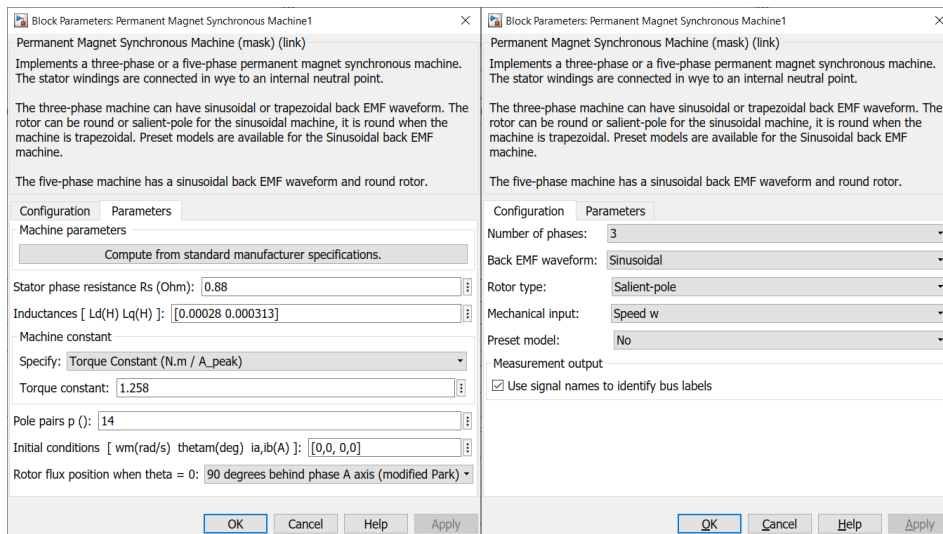


Figure 5.14. Motor Parameters

After the motor parameters were determined, a reference speed of 52 rad/sec (500 RPM) was given. A 120 Volt supply voltage is supplied to the 3-phase Inverter. Gate signals was 20kHz at 50%. After the parameters were determined, the circuit was simulated. The block diagram of the simulated circuit was shown in figure 5.15.

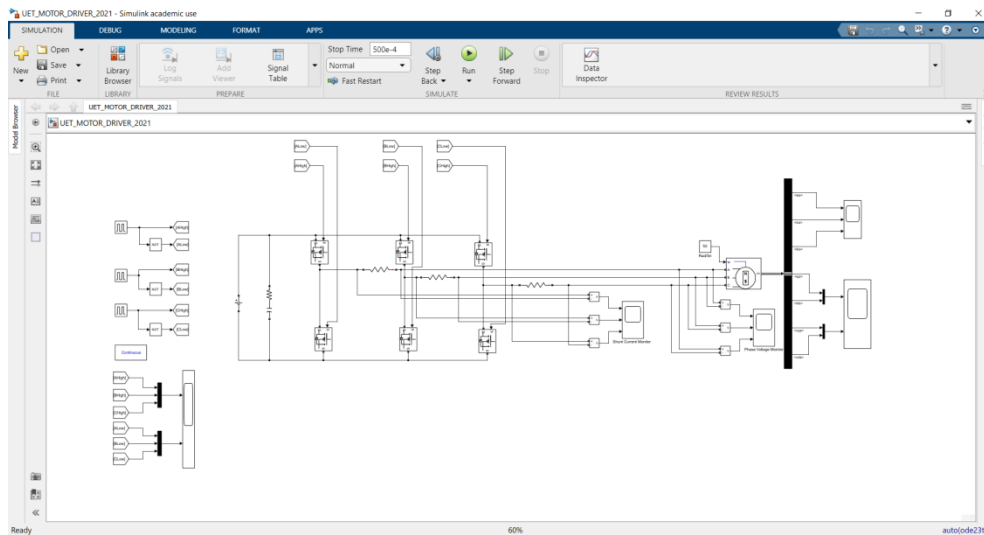


Figure 5.15. Inverter Block Diagram

Gate signals were shown in figure 3. Signals are 20 khz. Signals have a 50% duty cycle. And there is a phase difference of 120 degrees between the signals. Gate signals were shown in Figure 5.16.

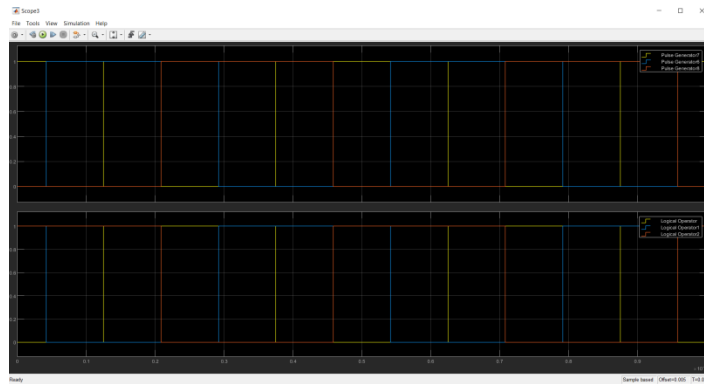


Figure 5.16. MOSFET's Gate Signal

Phase voltages of the simulated inverter were shown in figure 5.17. Signals were formed in a trapezoidal form. Phase voltages were  $V_{pp} = 120$  Volts.

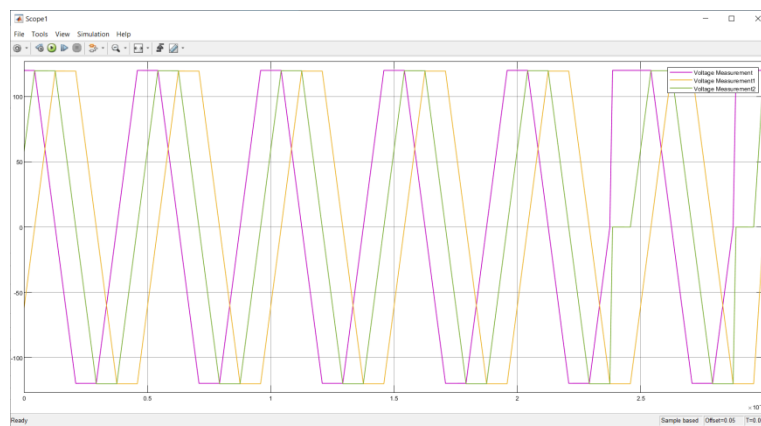


Figure 5.17. Phase Voltage

The electrical torque was shown in figure 5.18.

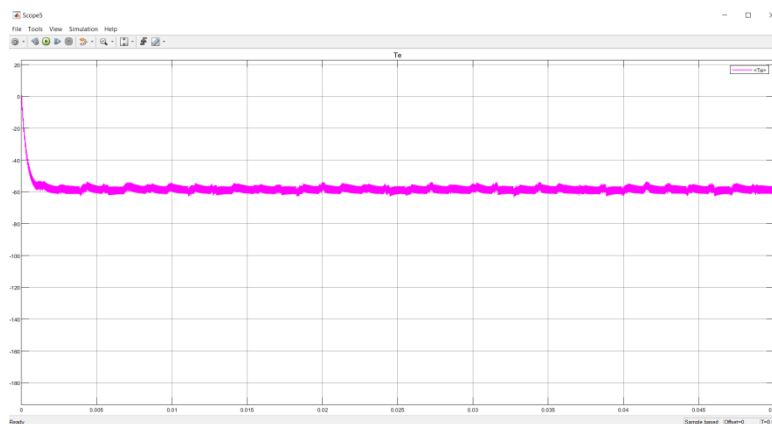


Figure 5.18. Electrical Torque

Phase currents of the circuit were shown in figure 5.19.



Figure 5.19. Phase Current of Motor Driver

The voltage across the  $1m\Omega$  shunt resistors was read. The voltage on the shunt was measured by the microprocessor. The voltage graph of the shunt resistors was shown in Figure 5.20.

$$V_{shunt} = 1,65 - \left( 8,2 \times \left( \frac{10k}{4,7k} \right) (I \times R_{shunt}) \right) \quad (5.12)$$

$$V_{shunt} = 1,65 - 17,44 \times I \times 1m\Omega \quad (5.13)$$

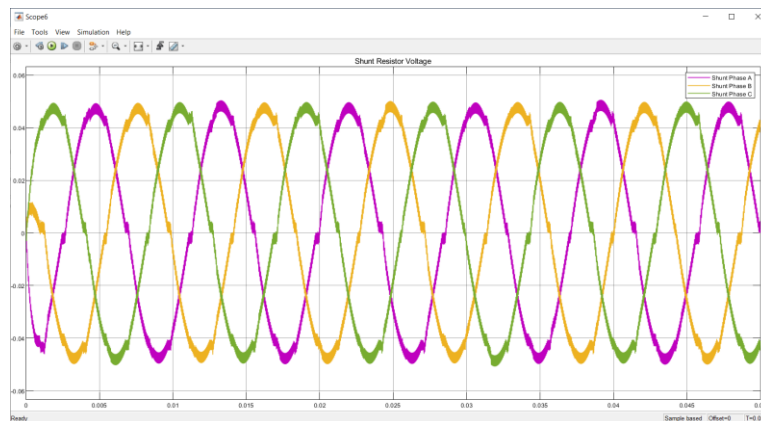


Figure 5.20. Voltage of Shunt Resistors

The currents and voltages of the motor driver in the Q and D axis were shown in figure 5.21.

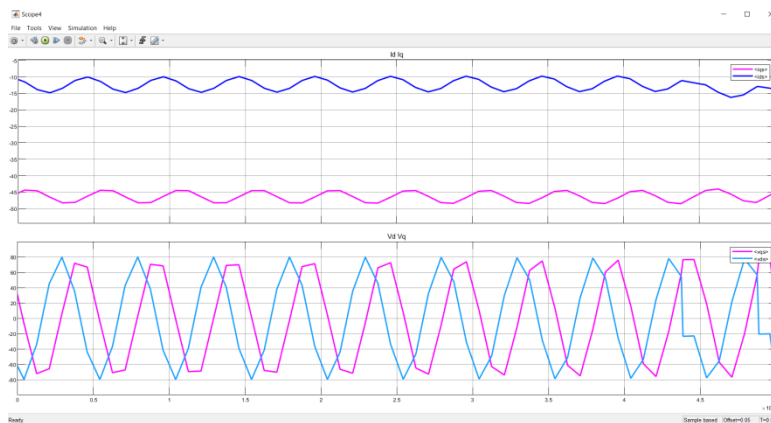


Figure 5.21. Voltage and current of Q axis and D axis

### 5.4.2. Simulation of Isolated Current Sense

Circuit analysis was done at TINA. AMC1301 isolated Op-Amp is used. The gain of the AMC1301 OpAmp is 8,2. Differential amplifier is made with LMV324 IC. The gain of the difference amplifier is 2,12.

Equation;

$$V_{shunt} = V_{ref} - (8,2 \times \left(\frac{10k}{4,7k}\right) (I \times R_{shunt})) \quad (5.14)$$

$$V_{shunt} = 1,65 - 17,44 \times I \times 1m\Omega \quad (5.15)$$

Current sensor was shown in figure 5.22. Circuit simulations were shown in figure 5.23.

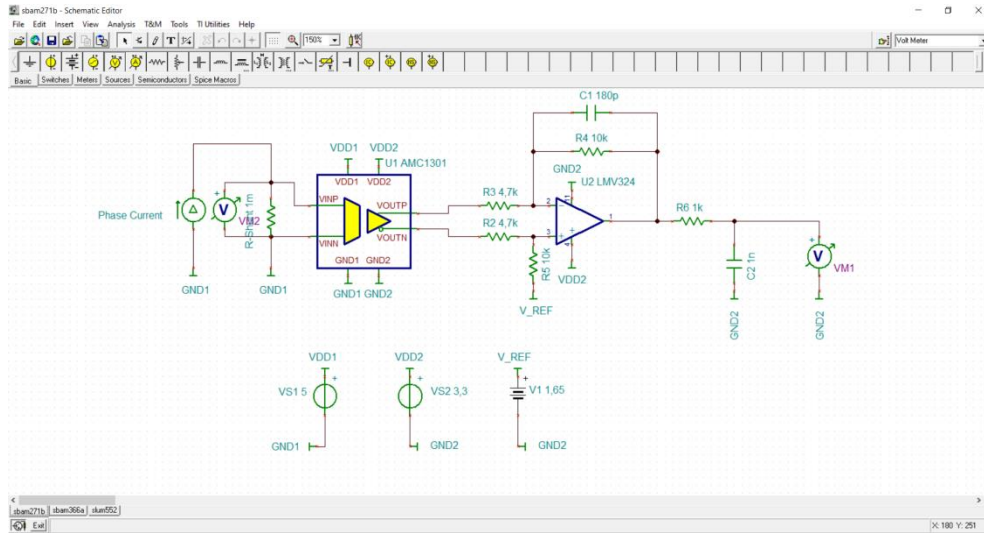


Figure 5.22. Isolated Current Sensor Circuit

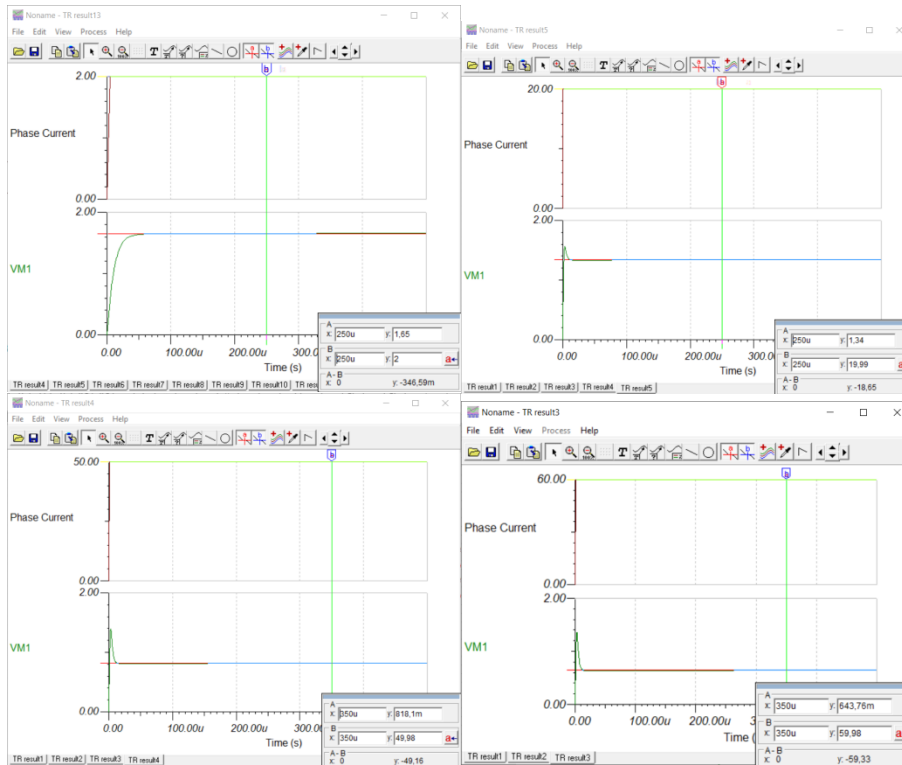


Figure 5.23. Simulation of Current Sense (+2A, +20A, +50A, +60A)

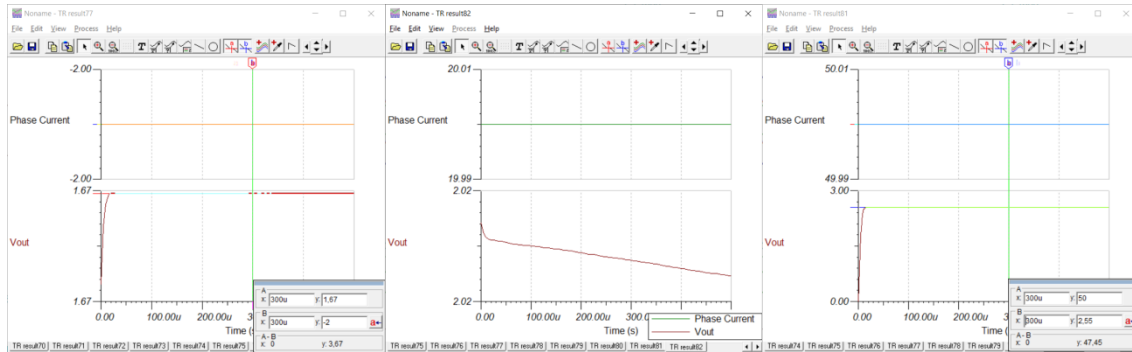


Figure 5.24. Simulation of Current Sense (-2A, -20A, -50A)

### 5.4.3. Simulation of Isolated Voltage Sense

Circuit analysis was done in TINA program. AMC1311 isolated Op-Amp is used. The circuit diagram was shown in figure 5.25. Voltage measurements were shown in figure 5.26 and figure 5.27. Equation;

$$V_{sense} = 1,65 - \left( HV \times \frac{R1}{R2} \times \frac{Rf}{R3} \right) \quad (5.16)$$

$$V_{sense} = 1,65 - \left( HV \times \frac{1M}{4,7k} \times \frac{10k}{4,7k} \right) \quad (5.17)$$

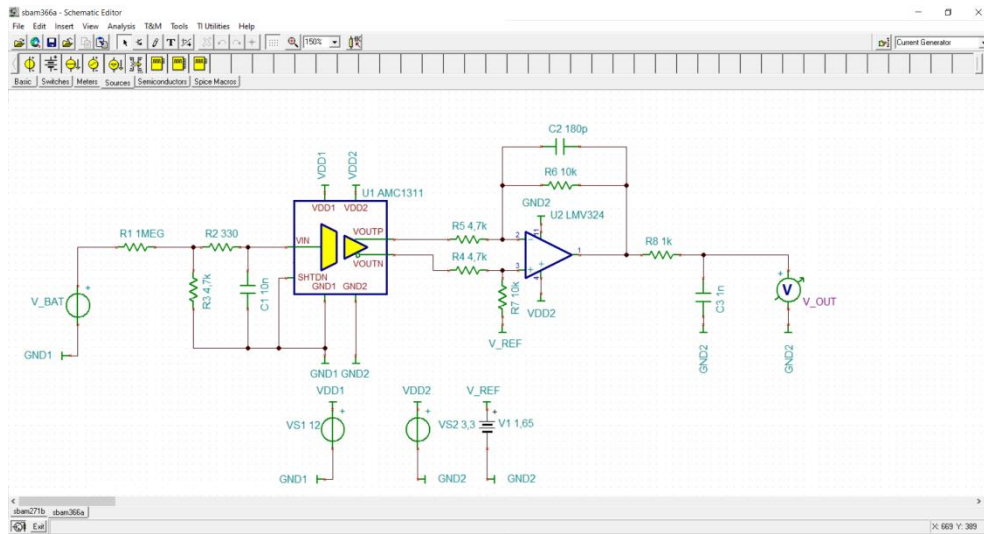


Figure 5.25. Isolated Voltage Sense Circuit

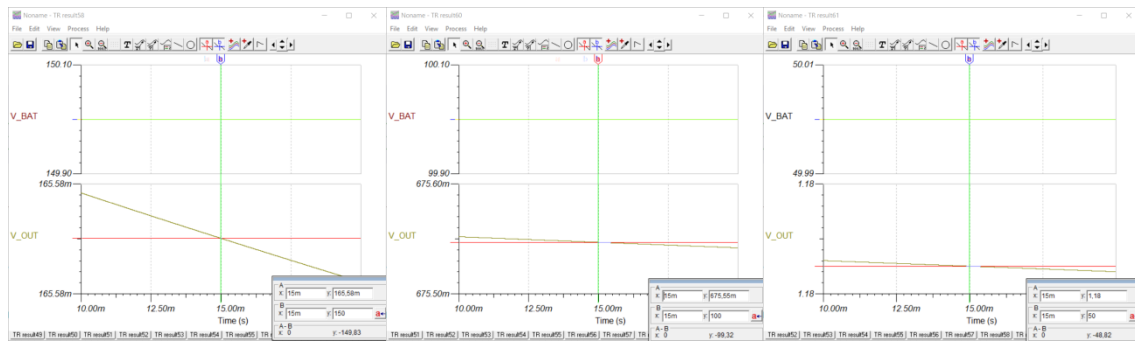


Figure 5.26. Simulation of Voltage Sense (150V, 100V, 50V)

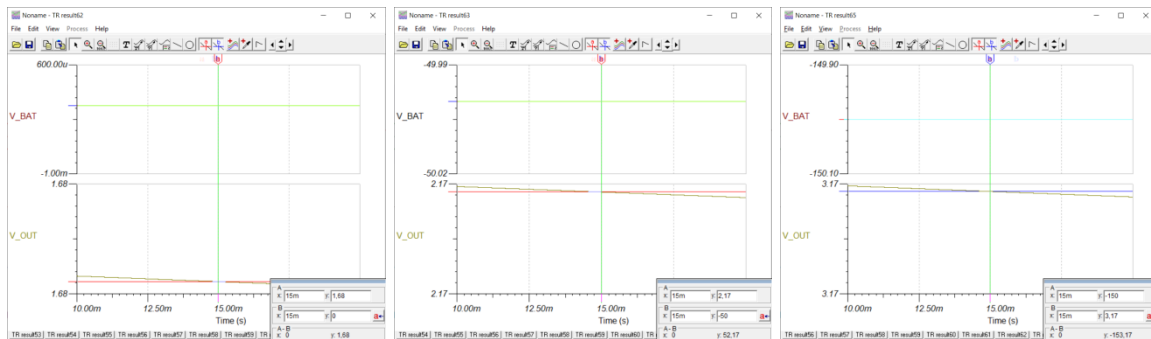


Figure 5.27. Simulation of Voltage Sense (0V, -50V, -150V)

#### 5.4.4. Simulation of Gate Driver

A simulation of the UCC21520 IC was made. Example circuit diagram was shown in figure 5.28. The simulation result was shown in figure 5.29.



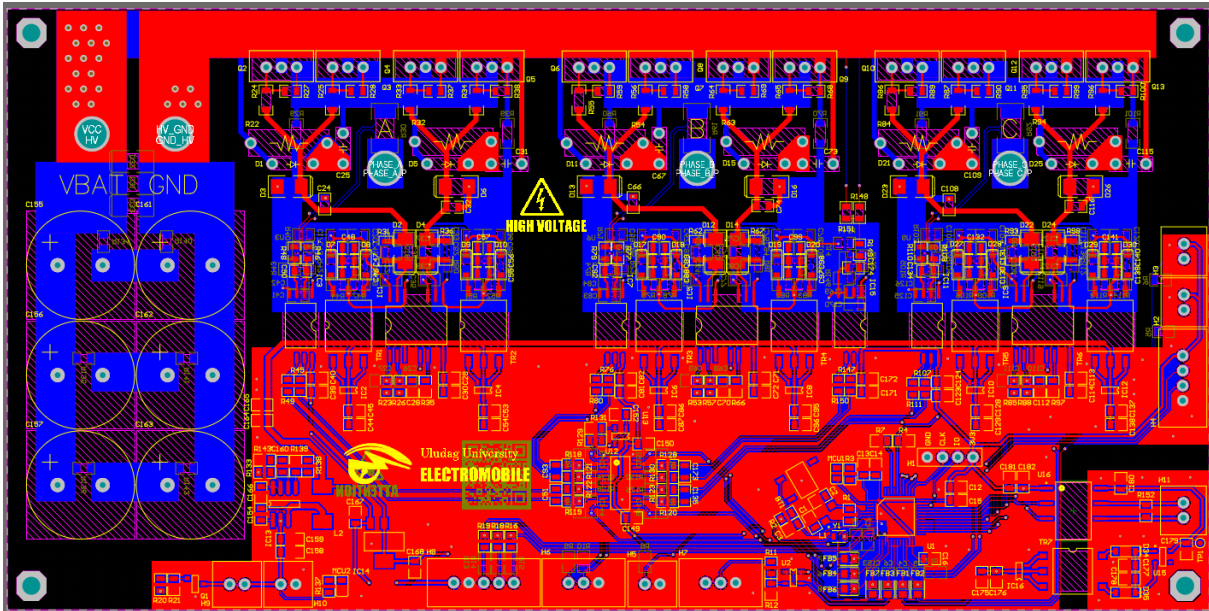


Figure 5.30. Motor Driver 2D Design

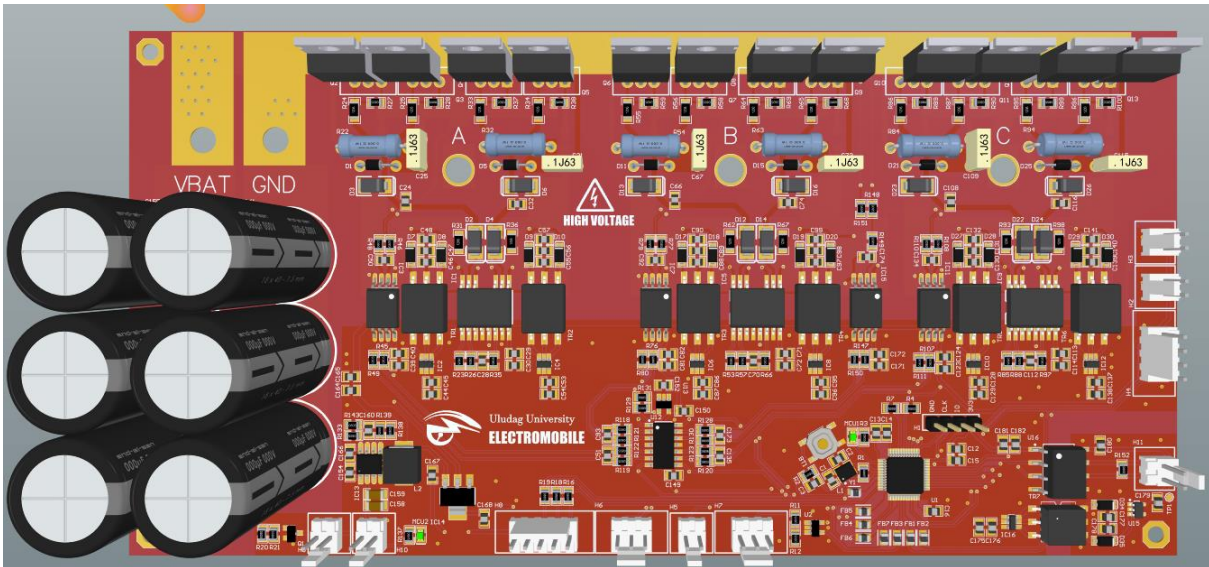


Figure 5.31. Motor Driver 3D Front Design

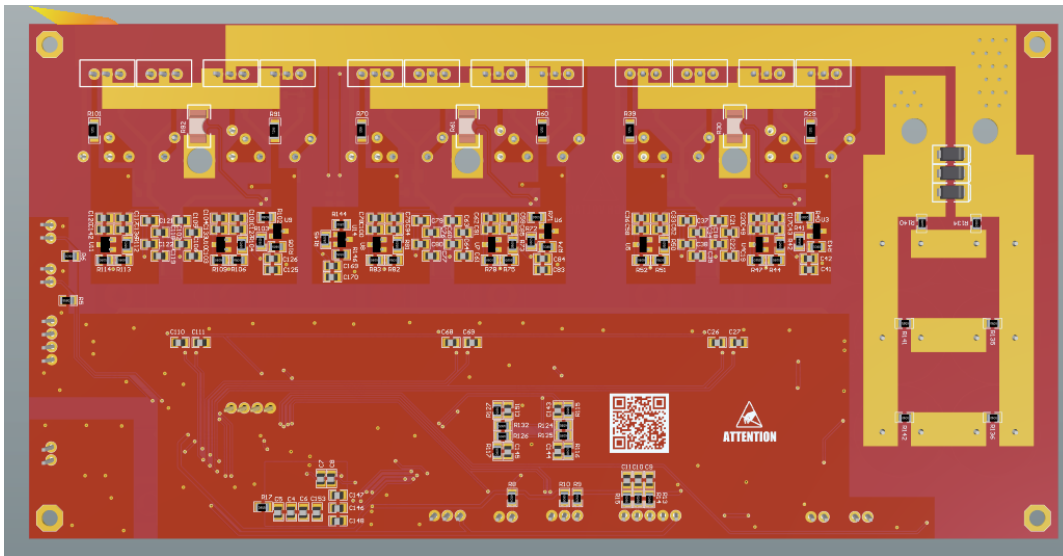


Figure 5.32. Motor Driver 3D Rear Design

### 5.7. Comparison Table

	Previous Design	Current Design
<b>Switch</b>	MOSFET	MOSFET
<b>Driver IC</b>	Infinion IR2101	TI UCC21542
<b>Controller IC</b>	Stm32f103c8t6	Stm32f302c8t6
<b>Control Algorithm</b>	Trapezoidal	Trapezoidal
<b>Protection Circuit</b>	Current and Voltage control	Current and Voltage control
<b>Electric Circuit Design</b>	Altium Designer	Altium Designer
<b>Printed Circuit Board Design</b>	Altium Designer	Altium Designer
<b>Printed Circuit Board Production</b>	JLCPCB	JLCPCB
<b>Software Algorithm</b>	Working with hall sensor	Working with hall sensor
<b>Simulation Studies</b>	MATLAB, TINA TI	MATLAB, TINA TI
<b>Experimental Studies</b>		
<b>Dimension (PCB / boxed hardware)</b>	139mm X 85mm	200mm X 100mm
<b>Power / Current / Voltage</b>	3.5KW / 30A / 120V	3.5KW / 30A / 120V
<b>Efficiency</b>		%99.6

<https://we.tl/t-orzZqq6bjb>

## 6. Battery Management System (BMS)

As a result of charge-discharge processes in the battery pack in electric vehicles, voltage difference between the cells and high temperature caused by chemicals occurs. In electric vehicles, batteries with high energy density are preferred in order to make the vehicle lighter and at the same time achieve higher range. Batteries with high energy density would cause undesirable results such as fire if not properly controlled. A Battery Management System is developed in order to use the energy stored in the battery pack effectively, efficiently and most importantly safely. The Battery Management System is the system that takes the necessary action by constantly controlling the parameters such as voltage, temperature, current of each cell.

Unbalanced and balanced cells are shown in Figure 6.1.

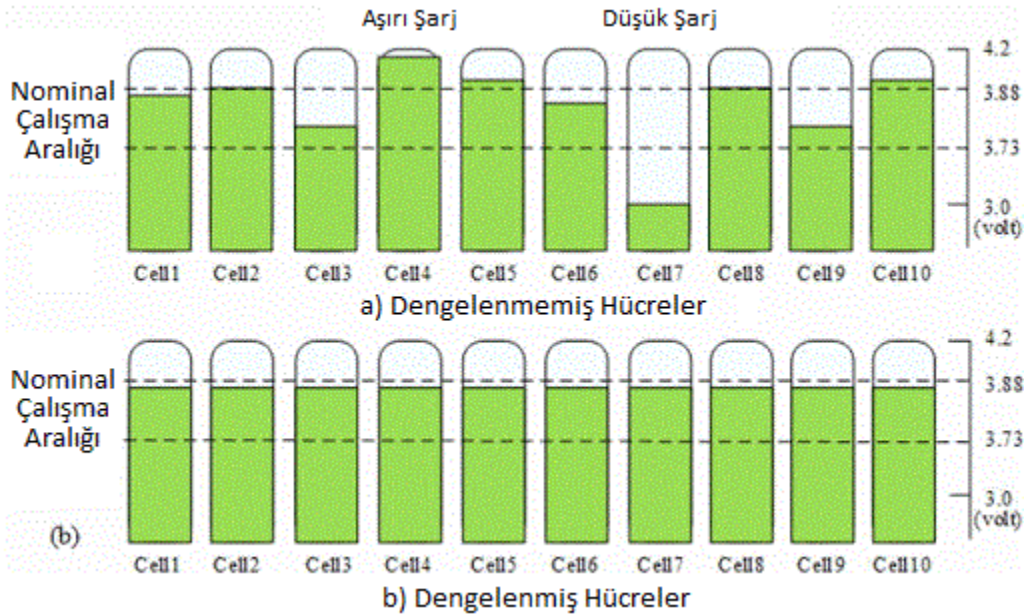


Figure 6.1. Unbalanced and Balanced Cells

Passive balancing system was preferred for the Battery Management System we designed for the 2021 race year of the TÜBİTAK Efficiency Challenge Electric Vehicle Races. The electronic board of the system was designed and drawn in Altium Designer program. TINA-TI program was used for analysis and simulations.

### 6.1. Circuit Designs

In this section, the circuit diagrams designed for the Battery Management System (BMS) will be mentioned.

#### 6.1.1. Microprocessor Selection

In the designed card, the STM32F302C8T6 microprocessor of STMicroelectronics company was preferred due to its features. The features requested and provided by the card can be

listed as CAN Communication, USART Communication, 12-bit ADC Port, GPIO Output Ports.

- CAN Communication is used for communication with other cards on the vehicle.
- USART Communication card is used to communicate with the computer.
- The 12-bit ADC Port is needed to read cell voltages and temperature data.
- GPIO Output Ports are used to activate the cell balancing circuit.

In Figure 6.2, the STM32F302C8T6 microprocessor is shown with its pin assignments performed.

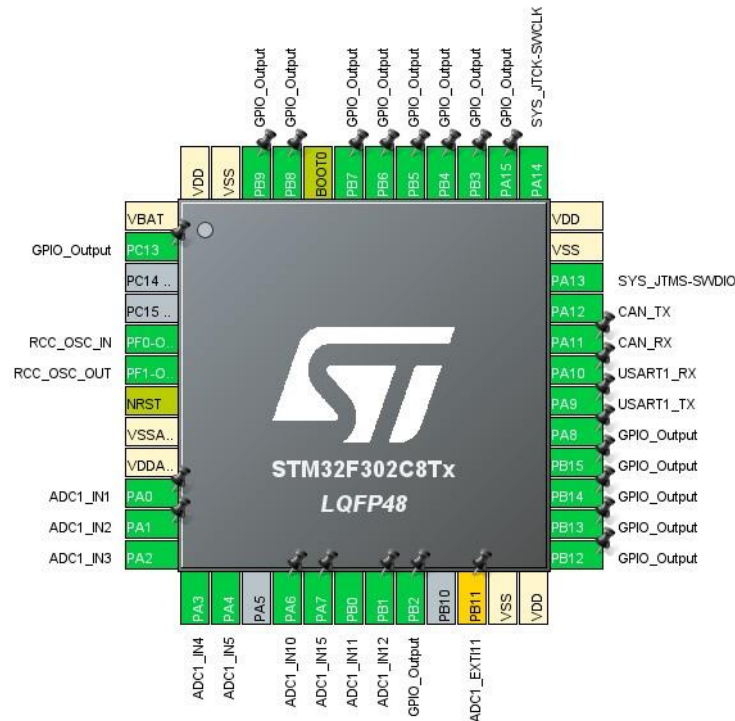


Figure 6.2. STM32F302C8T6 Microprocessor

### 6.1.2. VDD-VDDA LC Filter

LC Low-Pass Filter has been applied to prevent the analog feed of the microprocessor from factors such as interference and noise.

In Figure 6.3, VDDA LC Filter is shown.

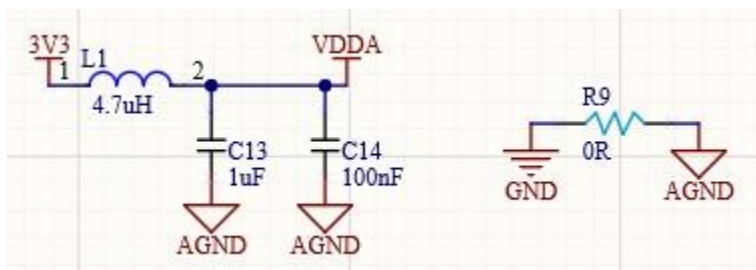


Figure 6.3. VDDA LC Filter

### 6.1.3. Cell Voltage Reading Circuit

The first step of the designed system is to read the cell voltages. Cell voltages were read using the Differential Amplifier method on the designed card. Since the voltage range of the microprocessor for ADC reading is 0 – 3.3V, the conversion ratio for the differential amplifier circuit is set to  $A_v = 1/2$ . MC33174DT Op-Amp IC, which contains 4 Op-Amps, can operate in the range of 4 – 44 V and has low input slip voltage, is used. An RC filter was applied to its output to prevent noise. Then the converted value was transmitted to the microprocessor.

Figure 6.4, shows the analysis made in TINA TI program for the voltage reading circuit of two series cells. Cell voltages sampled at 4 V were reduced to 1.94 V.

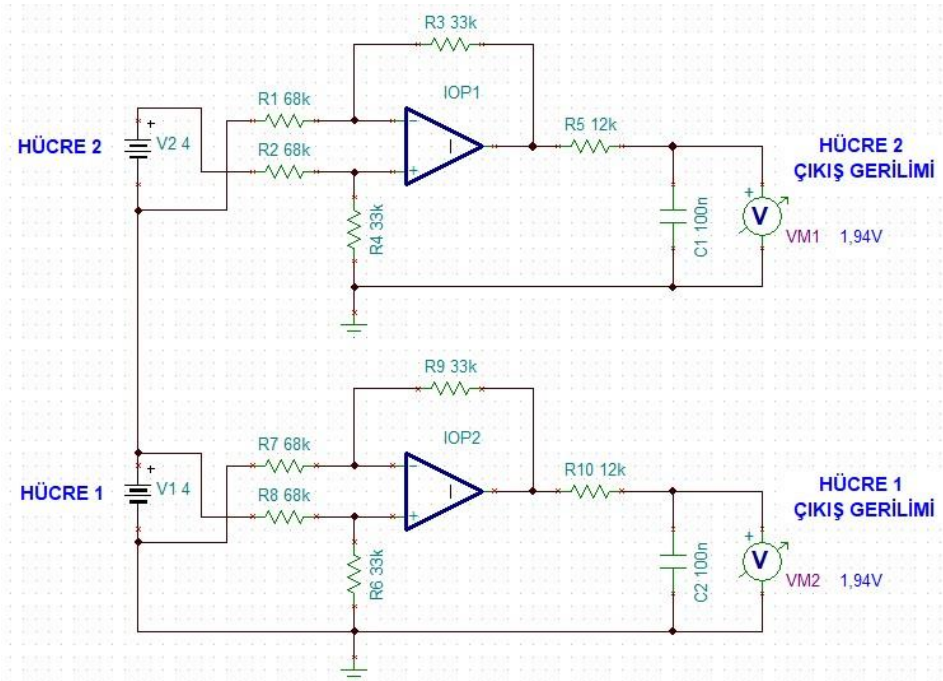


Figure 6.4. Voltage Reading Circuit of Two-Series Cell TINA TI Analysis

In Figure 6.5, the circuit design is shown in the Altium Designer program for the cell voltage reading circuit.

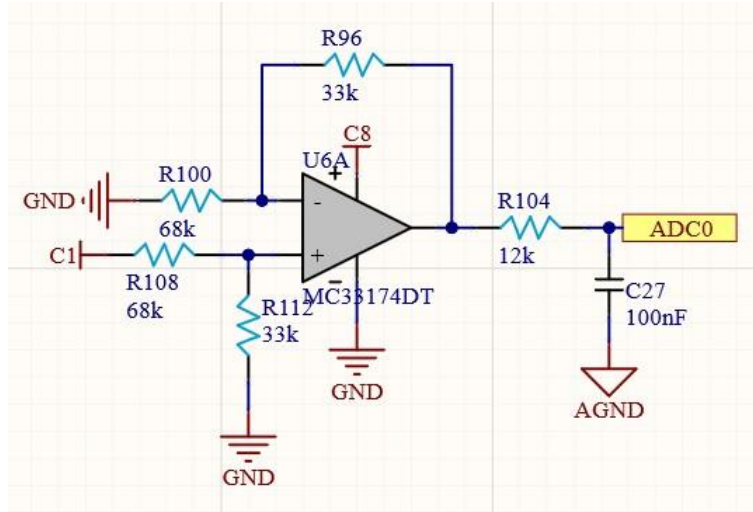


Figure 6.5. Altium Designer Drawing for Cell Voltages Readout Circuit

#### 6.1.4. Temperature Measurement

It is very important for the battery to work at the appropriate temperature in terms of efficient and healthy operation. In the designed card, 10k $\Omega$  NTC Thermistors were used to measure the temperature of the battery pack. NTC is a type of resistor that changes with temperature. As the temperature increases, the NTC resistance decreases. Added a buzzer to warn when the battery temperature reaches 55°C. In addition, when the temperature reaches 70°C, all systems connected to the vehicle are turned off for safety purposes. An optocoupler was used for the 12V buzzer. Optocouplers are circuit elements that provide electrical isolation of two circuits, consisting of an optically connected beam transmitter and photoreceiver. The optocoupler circuit is triggered by the microprocessor and then the buzzer is activated.

Figure 6.6 shows the variation of NTC resistance depending on temperature. Figure 6.7 shows the transmission of the NTC resistor to the processor with a 10k $\Omega$  resistor and a voltage divider followed by a voltage follower Op-Amp circuit. Figure 6.8 shows the optocoupler circuit set up for the Buzzer.

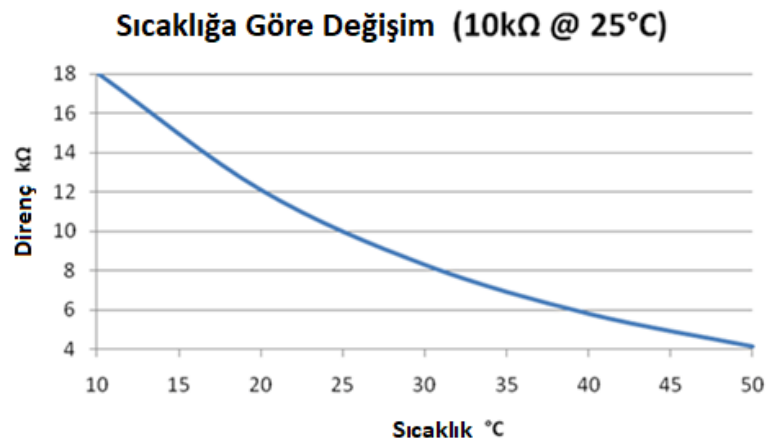


Figure 6.6. Variation of NTC Resistance with Temperature

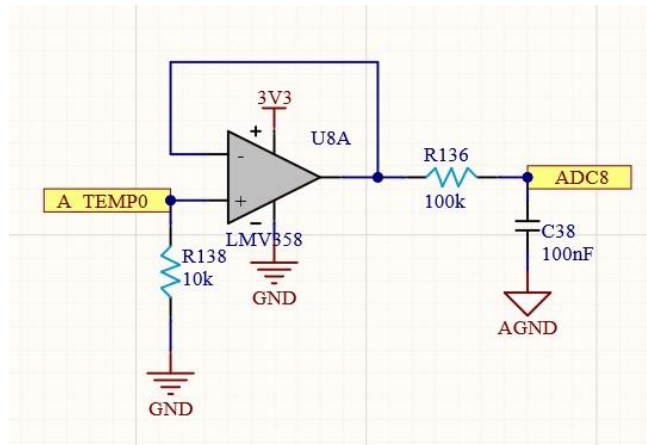


Figure 6.7. NTC Temperature Reading Circuit Altium Designer Drawing

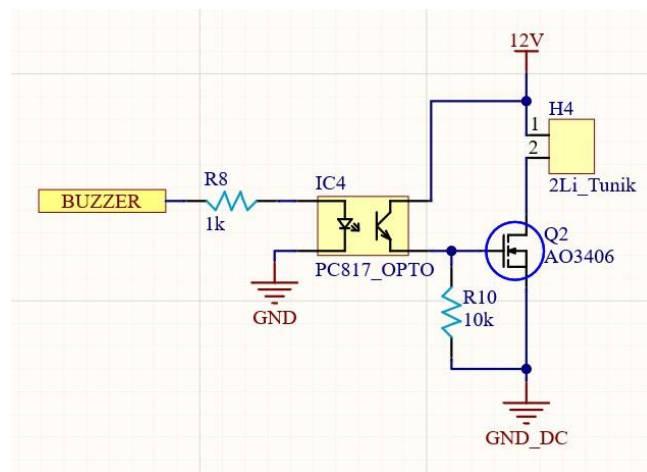


Figure 6.8. Buzzer Optocoupler Circuit Altium Designer Drawing

### 6.1.5. Cooling Fan

A fan has been added to the battery pack to cool the heated battery. Battery Management System controls the fan. When the temperature of the battery reaches 40°C, the fan activates and cools the battery. An optocoupler was used to activate the 12 V fan. PC-817 was preferred as optocoupler.

In Figure 6.9, the optocoupler circuit established for the cooling fan is shown.

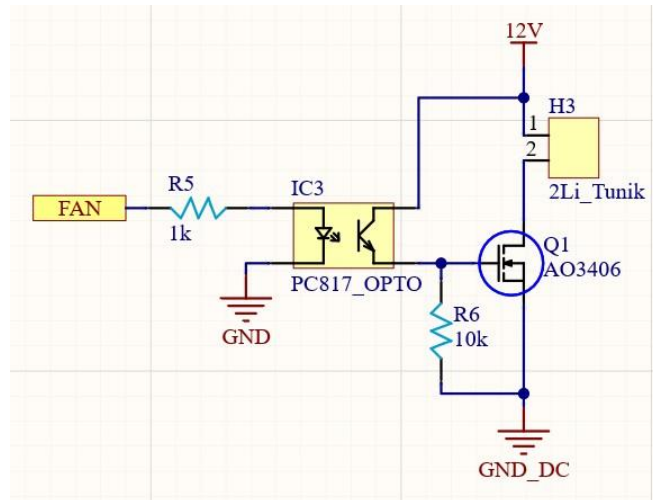


Figure 6.9. Fan Optocoupler Circuit Altium Designer Drawing

### 6.1.6. Isolated CAN Communication Protocol

CAN Communication Protocol is a serial communication protocol developed for use in the automotive industry, enabling systems to communicate with each other. It works safely and fast. It is used in our vehicle to receive data from other cards and to send data to other cards. It is very important to achieve error-free communication during data exchange. The CAN Communication circuit of the designed card is isolated from the SN6505 Transformer Driver, 760390012 Transformer, TPS76350 Voltage Regulator and ISO1050 CAN Transfer Integration and other system components.

At the same time, data such as the voltage of each cell, total voltage, state of charge (SOC) are transmitted to the VCU Main Board so that the driver of the vehicle could follow it instantly via CAN Communication.

Figure 6.10 shows the circuit designed for Isolated CAN Communication Protocol.

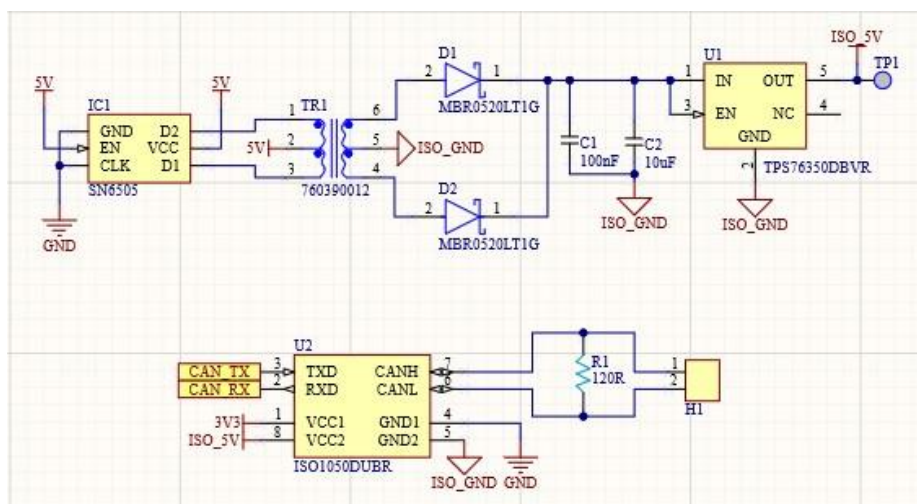


Figure 6.10. Isolated CAN Communication Protocol Circuit Altium Designer Drawing

## 6.2. Cell Balancing Method

There are two different balancing methods, passive and active, which are widely used. Passive balancing method was preferred as cell balancing method in the designed circuit. The 8 cell voltages read are transmitted to the microprocessor. Then, the processor gives a balancing command to the other cells by referring to the cell with the lowest voltage. Thanks to the switching elements that are transmitted with the command, the balancing process starts over the load resistor. The load resistor consists of 3 pieces of 1W 100 Ω resistors parallel to each other. It is converted into heat with these resistors and reduced to the reference cell level. In this way, the cells are balanced. BC817 NPN Transistor, BC857 PNP Transistor and AO3406 N-Channel MOSFET were used as switching elements.

Figure 6.11 shows the analysis of the Cell Balancing Circuit.

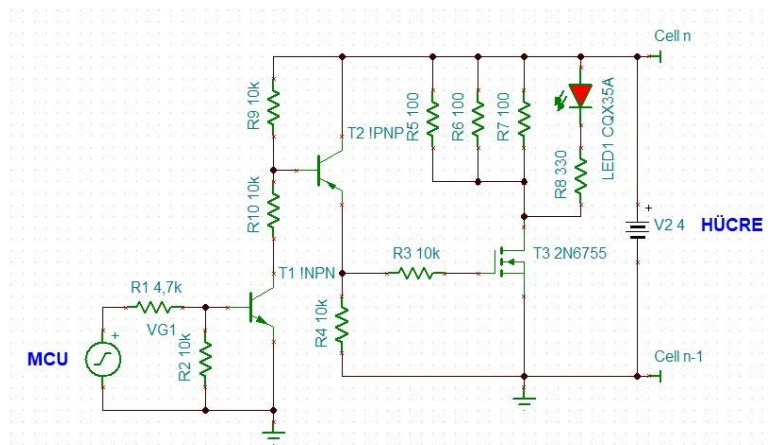


Figure 6.11. Cell Balancing Circuit Analysis TINA TI Drawing

Balancing Current;

$$V_{cell} = 3,7 \text{ V}$$

$$R_{load} = (100//100//100) = 33,3 \text{ } \Omega$$

$$I_{balancing} = \frac{V_{cell}}{R_{cell}} = \frac{3,7}{33,3} = 111 \text{ mA}$$

In Figure 6.12, the circuit design of the Cell Balancing Circuit is shown in the Altium Designer program.

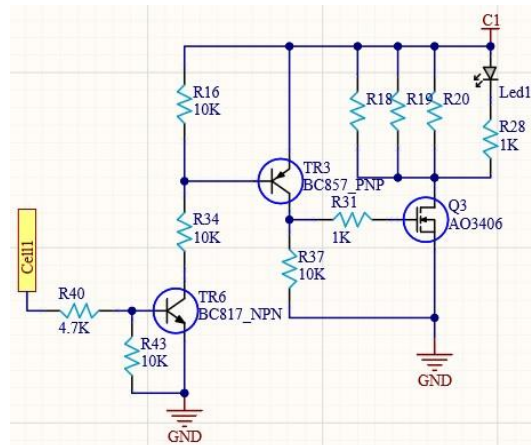


Figure 6.12. Cell Balancing Circuit Altium Designer Drawing

### 6.3. DC to DC Converters

In this section, the 5V and 3.3 V supplies required for the designed board will be mentioned.

#### 6.3.1. Isolated DC to DC Converter

The main supply of the designed card is provided by 12V from the DC-DC converter on the vehicle so that the BYS does not work when the vehicle is turned off. The CAN Communication Line is powered by 5V. TMA1205 isolated DC-DC converter is used for conversion.

Figure 6.13, shows the Isolated DC to DC converter Altium Designer drawing.

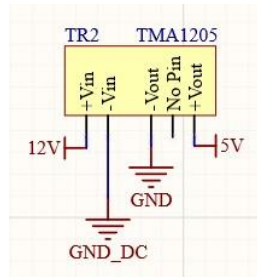


Figure 6.13. TMA120 Isolated DC to DC Converter Altium Designer Drawing

#### 6.3.2. Voltage Regulator

3.3 V is required to supply components such as the microprocessor and Op-Amp on the board. 5V from isolated DC to DC converter provided 3.3V using AMS1117 Voltage Regulator.

AMS1117 Voltage Regulator Altium Designer circuit is shown in Figure 6.14.

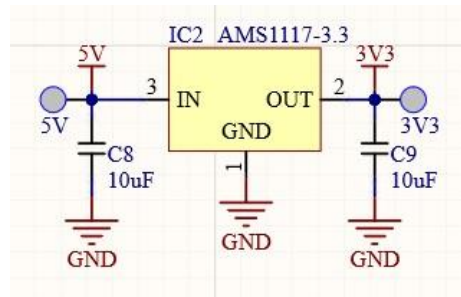


Figure 6.14. AMS1117 Voltage Regulator Altium Designer Drawing

## 6.4. Control Algorithm

After the system is started, error control is performed for high voltage, low voltage, high temperature, high current. If there is no error, cell voltage balance data is received. If the voltage level is normal, the temperature control is started. If the voltage levels are abnormal, balancing is initiated. Then the temperature control is done. If the battery temperature is above 40°C, the fan is active. When it rises above 55°C, the buzzer works for warning purposes and if it is above 70°C, all systems connected to the vehicle are turned off. If the temperature values are normal, the error control phase is returned. The Control Algorithm flow diagram is shown in Figure 6.15.

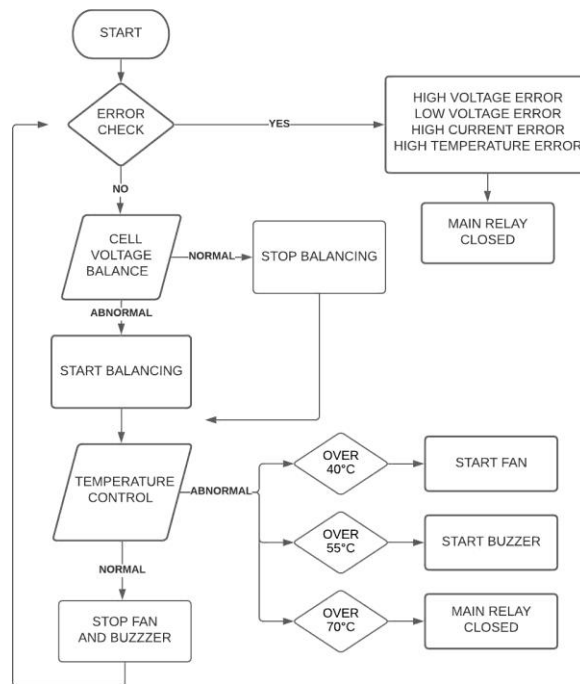


Figure 6.15 Control Algorithm Flow Chart

## 6.5. PCB Designs

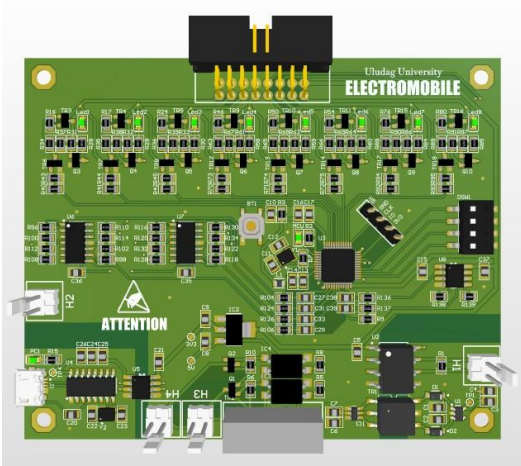


Figure 6.16. Top Layer BMS

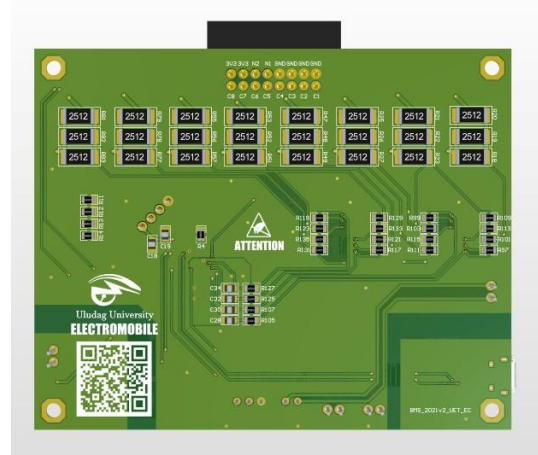


Figure 6.17. Bottom Layer BMS

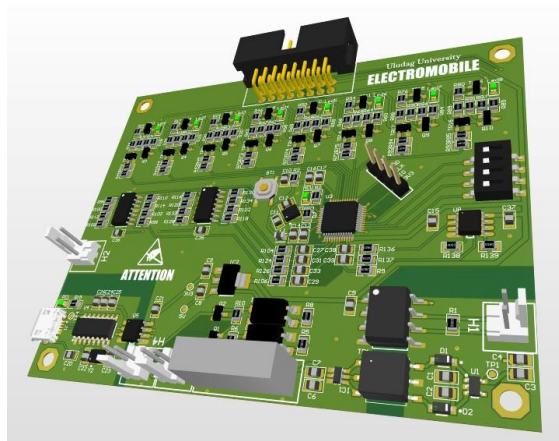


Figure 6.18. BMS 3D

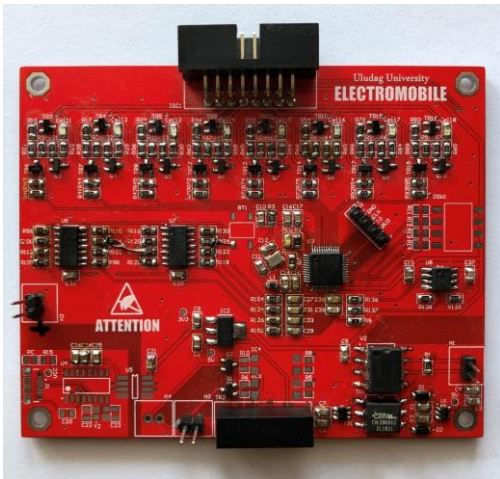


Figure 6.19. Top View



Figure 6.20. Bottom View

		<b>Previous Design</b>	<b>Current Design</b>
<b>Battery Packing Design</b>	:	32 Serial 8 Parallel	32 Serial 8 Parallel
<b>Output Voltage</b>	:	120 V	120 V
<b>Output Current</b>	:	30 A	30 A
<b>Balancing Method (active or passive)</b>	:	Passive	Passive
<b>Circuit Design Type</b>	:	PCB Board	PCB Board
<b>SOC Estimation Algorithm</b>	:		
<b>Control Algorithm</b>	:	Available	Available
<b>Domestic or Not</b>	:	Domestic	Domestic

<https://we.tl/t-9D51KernAi>

## 7. Embedded Recharging Unit

This section will explain the Embedded Recharging Unit of the Uludag University Electromobile Team UET Istiklal vehicle. The system built works with 220V AC and produces 140V DC output. Circuit designs were made in Altium Designer, circuit analyzes were made in TI Tina. This is the block diagram of the ERU in figure 7.1.

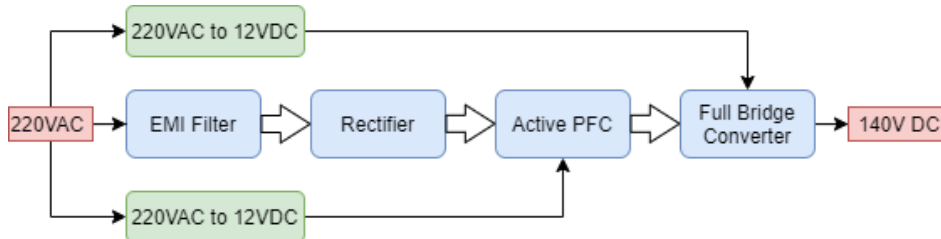


Figure 7.1. Embedded Recharging Unit Block Diagram

### 7.1. Circuit Design

Circuit schematics and calculations will be explained in this section.

#### 7.1.1. EMI Filter

Common Mode Differential Filter has been designed to prevent electromagnetic interference. The circuit diagram is shown in Figure 7.2. Detailed schematic and PCB files are attached as PDF file.

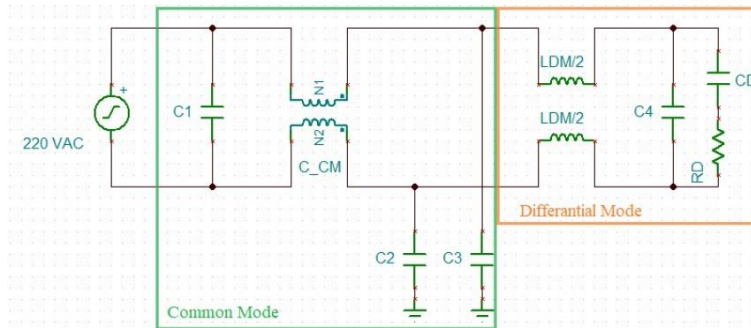


Figure 7.2. EMI Filter

#### 7.1.1.1. Differential Mode

In this section, circuit elements for differential mode filter are calculated. Impedance paper was used while making calculations. Impedance paper is shown in Figure 7.3. The red lines show the capacitor value range, the blue lines show the value range of the coil.  $Z_0 = 5\Omega$ .  $F_{cut-off} = 30kHz$ . The area scanned by the lines shows the capacitor and coil values to be selected in desired value ranges. Using the table, the capacitor value  $C_4 = 2.2\mu F$  was chosen. According to this value;

$$F_{dm} = 30kHz \quad (7.1)$$

$$F_{dm} = \frac{1}{2 \times \pi \times \sqrt{L \times C}} \quad (7.2)$$

$$30 \times 10^3 = \frac{1}{2 \times \pi \times \sqrt{L \times 2.2 \times 10^{-6}}} \quad (7.3)$$

$$L = 0.12 \mu H \quad (7.4)$$

$C_{damping}$  should be  $\geq 5 \times C4$ .  $C_{damping} = 22 \mu F$  was chosen.  $R_{damping} = R_{cesr}$  was chosen.

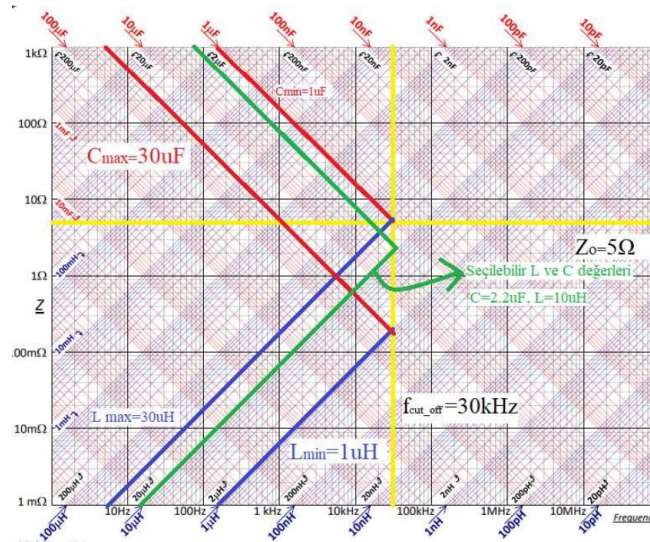


Figure 7.3. Impedance Paper

### 7.1.1.2. Common Mode

Common mode noise is observed at high frequencies.  $f_{cm\text{cutoff}} = 30 \text{ kHz}$  was chosen

$$f_{cm - cutoff} = \frac{1}{2 \times \pi \times \sqrt{L \times C}} \quad (7.5)$$

$L = 10 \text{ mH}$  was chosen

$$30 \times 10^3 = \frac{1}{2 \times \pi \times \sqrt{L \times 10 \times 10^{-3}}} \quad (7.6)$$

$C = 2.81 \text{ nF}$  was calculated.

### 7.1.2. Active PFC

In this section, PFC, full bridge rectifier, precharge and input capacity circuits and calculations are explained. The PFC circuit diagram is shown in Figure 7.4. Detailed schematic and PCB files are attached as pdf file.

UCC28070 is used as PFC controller integrated. This controller works interleaved. It reads the input and output voltages with a voltage divider. It reads the phase currents from the PA1005.100NL pulse transformer. It needs PI compensator for the control loops of the phases. UCC27211 gate driver IC is used to drive MOSFETs.



$$\tau = 1000 \times 0.003 = 3sn \tag{7.13}$$

$$\tau = 5\tau = 15sn \tag{7.14}$$

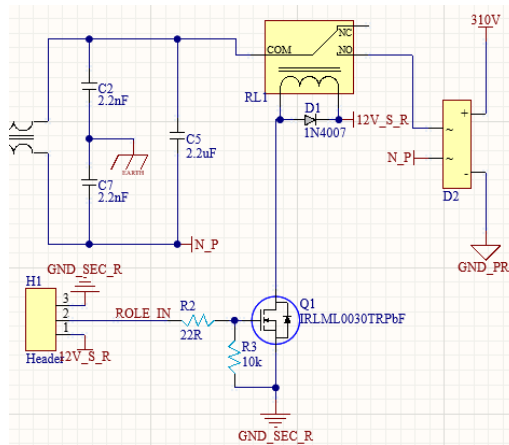


Figure 7.6. Precharge Circuit

### 7.1.3. Full Bridge Converter

A full bridge converter is a DC to DC converter topology employing four active switching components in a bridge configuration across a power transformer.

A full bridge converter is one of the commonly used configurations that offer isolation in addition to stepping up or down the input voltage. Other functions may include reversing the polarity and providing multiple output voltages simultaneously.

Figure 7.7 shows the circuit diagram of a conventional full-bridge DC-DC converter. In the circuit, the switches Q1 and Q4 are switched on and off at the same time. While the switches Q1 and Q4 are in transmission, positive input voltage is applied to the primary of the transformer and power is transferred to the output. Switches Q2 and Q3 are switched on after a certain period of time after the switches Q1 and Q4 are interrupted at the same time. In this case, negative voltage is applied to the primary of the transformer and power is transferred to the output again. As a result, a high frequency AC voltage is generated in the transformer primary.

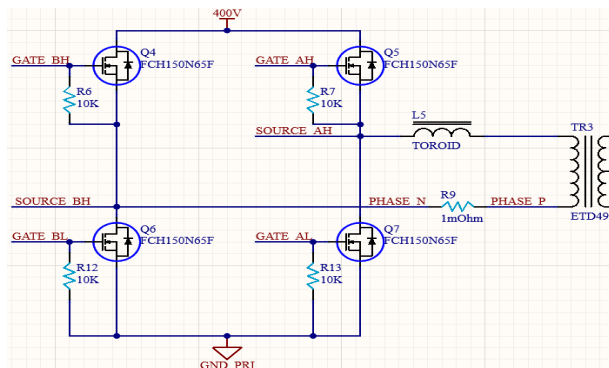


Figure 7.7. Full Bridge Converter

The basic operation involves switching one pair of transistors at a time for one half cycle of the control waveform and the other pair during the other part of the waveform. The two control strategies use the pulse width modulation signal to either switch the transistors on each leg simultaneously as a pair or switch them independently in series.

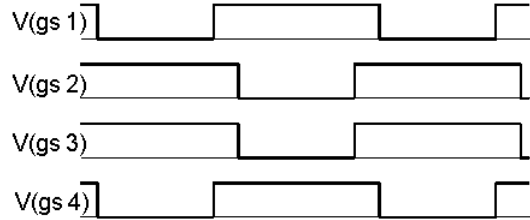


Figure 7.8. Hard Switch Control Waveform

FCH150N65F MOSFETs, which we used in the Full wave converter in Figure 7.7, have a voltage of 650V Vds, an internal resistance of 0.15 ohms, and a continuous current flow of 24A.

### 7.1.3.1. ZVS Control Topology

We used the ZVS control topology to dampen the leakage inductance caused by the structure of the transformers in the SMPS circuits. The inductance  $L_r$  in Figure 7.7 is used for the ZVS topology.

The required  $C_{oss} = 72pF$  in the calculations and the transformer input capacitance is  $66pF$ .

$$C_{eq} = 2 \times C_{oss} + C_{tr} = 2 \times 72pF + 66pF = 210pF \quad (7.15)$$

The capacity energy to be extracted in the transition can be explained as follows:

$$W_{cr} = \frac{1}{2} \times C_{eq} \times V_{bus}^2 \quad (7.16)$$

To soft-close the switch, the energy stored in  $L_2$  must be greater than the energy stored in  $C_{eq}$ :

$$W_{Lr} = \frac{1}{2} \times L_r \times I_1^2 \geq \frac{1}{2} \times C_{eq} \times V_{bus}^2 = W_{Cr} \quad (7.17)$$

The value of the resonant inductor depends on the desired minimum current. Usually,  $L_r$  is chosen to obtain ZVS for loads above a certain value.

Another method for choosing the  $L_r$  inductor is that the transition time should be greater than four times the resonant tank frequency.

$$T_{transition_{max}} = \frac{T_r}{4} \quad (7.18)$$

The resonance period is:

$$T_r = \frac{2\pi}{\omega_r} \quad (7.19)$$

$\omega_r$  resonant radian frequency is:

$$\omega_r = \frac{1}{\sqrt{C_{eq} \times L_r}} \quad (7.20)$$

When the above equations are combined,  $L_r$  :

$$L_r = \frac{1}{\omega_r^2 \times C_{eq}} = \left( \frac{2 \times T_{transitionmax}}{\pi} \right)^2 \times \frac{1}{C_r} \quad (7.21)$$

Current rise when we choose resonant inductor 47uH:

$$\frac{di}{dt} = \frac{V_{bus}}{L_r} = \frac{400}{47 \times 10^{-6}} = 8.51 \text{ A/us} \quad (7.22)$$

And then if the critical amount of current required to enter hard switch mode is:

$$I_{critical} = V_{bus} \times \sqrt{\frac{C_{eq}}{L_r}} = 400 \times \sqrt{\frac{210 \times 10^{-12}}{47 \times 10^{-6}}} = 0.84A \quad (7.23)$$

This means that when the primary current exceeds 0.84A and the dead time is set properly, the converter enters soft switching mode.

### 7.1.3.2. Dead Time

The resonant circuit consists of  $C_{eq}$  and  $L_r$ . The period of this oscillation:

$$T_r = 2 \times \pi \times \sqrt{C_{eq} \times L_r} = 2 \times \pi \times \sqrt{210 \times 10^{-12} \times 47 \times 10^{-6}} = 624ns \quad (7.24)$$

Dead time should be chosen more than a quarter of the oscillation period.

$$T_d = \frac{\pi}{2} \times \sqrt{C_{eq} \times L_r} = \frac{\pi}{2} \times \sqrt{210 \times 10^{-12} \times 47 \times 10^{-6}} = 156ns \quad (7.25)$$

We also gave 250ns dead time as a result of experimental studies.

### 7.1.3.3. Transformer Calculations

We chose ETD49 transformer core for power transfer. Core effective area  $2.11 \text{ cm}^2$ , Al value is 3900 nH. Number of primary windings of the transformer:

$$N_{pri} = \frac{V_{bus} \times 10^4}{4 \times A_e \times \Delta B \times F_{sw}} = \frac{400V \times 10^4}{4 \times 2.11 \text{ cm}^2 \times 0.2T \times 50 \text{ kHz}} = 47 \text{ turn} \quad (7.26)$$

Transformer magnetizing inductance:

$$L_m = A_L \times N_{pri}^2 = 3900 \text{ nH} \times 47^2 = 8.61 \text{ mH} \quad (7.27)$$

Primer and seconder and transfer ratio formula:

$$\frac{N_{pri}}{N_{sec}} = \frac{V_{inmin}}{V_{out}} \times D_{max} = \frac{390}{140} \times 0.8 = 2.22 \quad (7.28)$$

Seconder winding turn count is 21 turns.

### 7.1.3.4. Secondary Side Calculations

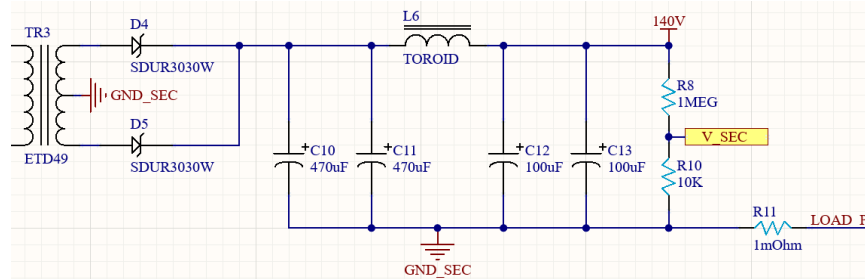


Figure 7.9. Secondary Side Rectification

We used bridge type rectification at the output. We used a  $\pi$ -circuit to minimize output current and output voltage fluctuation.

### 7.1.3.5. Output Choke Calculation

We have assumed a maximum of 20% output current fluctuation.

$$I_{ORIPPLE} = \frac{P_{OUTMAX} \times Ripple}{V_{OUTMIN}} = \frac{1500 \times 0.2}{138} = 2.17A \quad (7.29)$$

$V_{LMAX}$  is the maximum voltage drop on output inductance and  $t_{on}$  is the corresponding on – state time:

$$V_{LMAX} = \frac{N_s}{N_p} \times V_{INMAX} - V_{OUTMIN} = \frac{21}{47} \times 400V - 138V = 40.72V \quad (7.30)$$

$$t_{on} = \frac{1}{2} \times \frac{N_p}{N_s} \times \frac{V_{OUTMIN}}{V_{INMAX}} \times T_s = \frac{1}{2} \times \frac{47}{21} \times \frac{138V}{400V} \times 20 \times 10^{-6} = 7.72us \quad (7.31)$$

Output choke:

$$L_{OMIN} = \frac{V_{LMAX}}{I_{ORIPPLE}} \times t_{on} = \frac{40.72V}{2.17A} \times 7.72us = 144uH \quad (7.32)$$

Output Capacitor Calculation

The output capacitor has been designed to satisfy the maximum load transient:

$$t_{transient} = \frac{P_{out} \times L_{OMIN} \times 0.9}{V_{OUTMIN}^2} = \frac{1500 \times 144 \times 10^{-6} \times 0.9}{138^2} = 10.20us \quad (7.33)$$

$$C_{out} \geq \frac{\Delta I_c}{\%1 \times \frac{\Delta V_c}{\Delta t}} = \frac{\frac{P_{out} \times 0.9}{V_{OUTMIN}}}{\frac{0.01 \times V_{ripple}}{t_{transient}}} = \frac{\frac{1500 \times 0.9}{138}}{\frac{0.01 \times 6.9}{10.20 \times 10^{-6}}} = 1.4mF \quad (7.34)$$

We chose 470uF // 470uF // 100uF // 100uF capacitor bank.

### 7.1.3.6. Voltage and Current Measures

Current and voltage measurement circuits are shown in Figure 7.10.

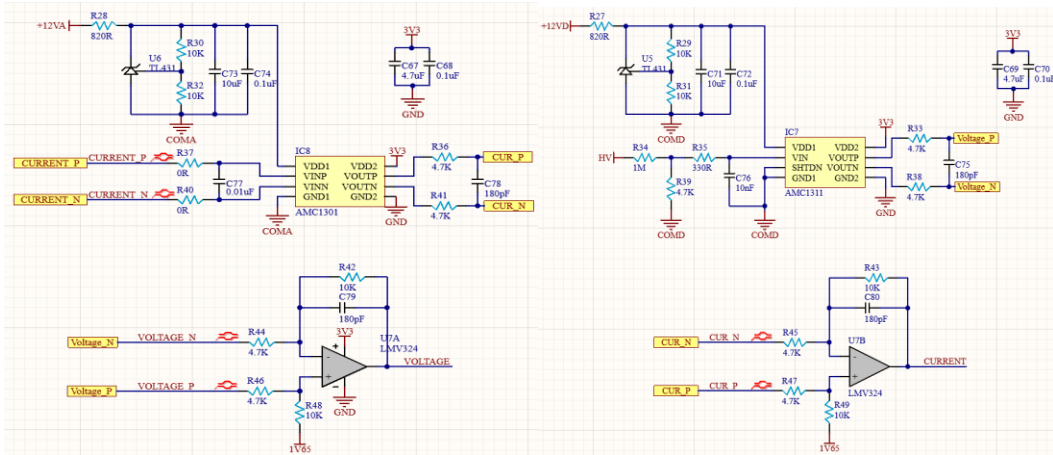


Figure 7.10. Primary Side Voltage and Current Measuring

Primary Side Current Measurement;

Current is read through a shunt resistor.  $R_{shunt} = 1m\Omega$ . The circuit of the Shunt resistor is shown in Figure 7.7. Current measurement with isolated OpAmp is shown in figure 7.10.

$$V_{shunt} = I_{primary} \times R_{shunt} \quad (7.35)$$

$$I_{primaryout} = \left(\frac{10K}{8.4K}\right) \times 8.2 \times V_{shunt} + 1.65 \quad (7.36)$$

Primary Side Voltage Measurement;

Voltage divider was used in voltage measurement. The circuit diagram is shown in figure 7.10.

$$V_{in} = V_{bus} \times \left(\frac{2.2K}{1M+2.2K}\right) + 1.65 \quad (7.37)$$

Secondary Side Current Measurement;

The schematic of the current measurement circuit is shown in figure 7.11.

$$V_{shunt} = I_{secondary} \times R_{shunt} \quad (7.38)$$

$$I_{primerout} = \left(\frac{10K}{4.7K}\right) \times V_{shunt} \quad (7.39)$$

Secondary Side Voltage Measurement;

Voltage divider was used in voltage measurement. The circuit diagram is shown in figure 7.11 and figure 7.9.

$$V_{in} = V_{bus} \times \left(\frac{10K}{1M+10K}\right) \quad (7.40)$$

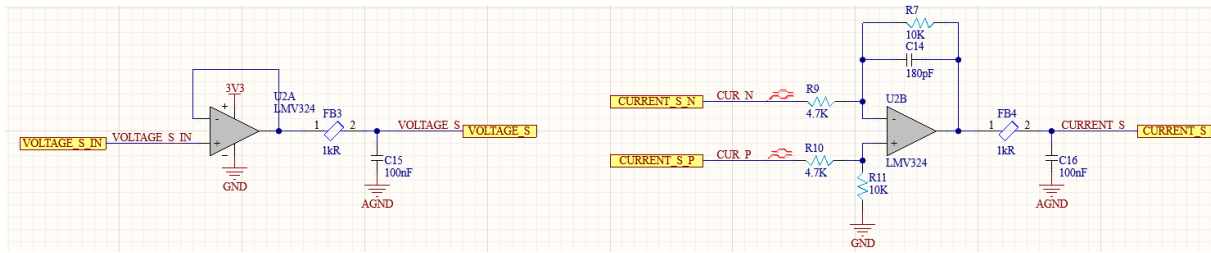


Figure 7.11. Secondary Side Voltage and Current Measuring

The current and voltage measurement of the primary part is read in isolation. In the primary part, an isolated gate driver structure is installed to drive the power MOSFETs. Isolated OpAmps get their power supply from this structure.

#### 7.1.4. Predrive Card

In this section, information about the predrive card of ERU is given.

An isolated structure is used to drive the power MOSFETs. High and Low side MOSFETs are driven by 4 power units isolated from each other. Würth 750316818 transformer is used with SN6505 transformer driver. TI UCC21542 is used as MOSFET driver. This driver can give 4A sink, 6A source current.

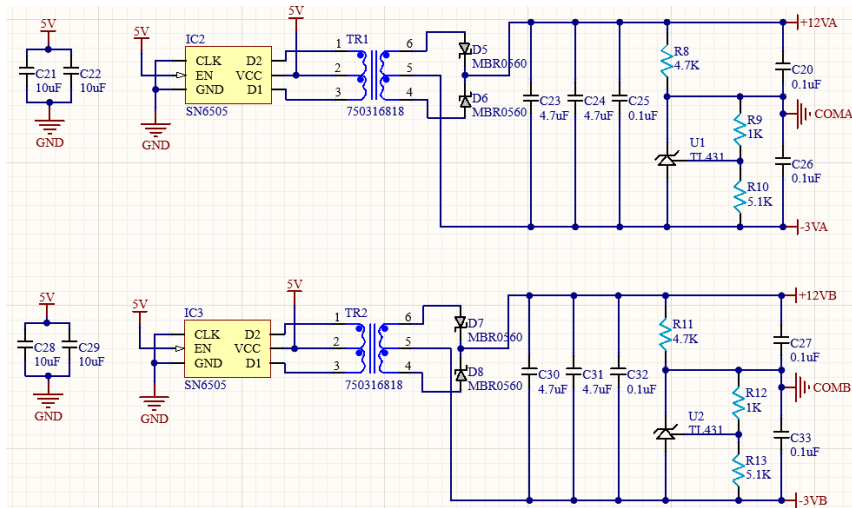


Figure 7.12. Half Bridge MOSFET Driver Power Supply

The gate is fed between +12V/-3V to ensure the full closure of the MOSFETs. The 15V output from the transformer is adjusted as +12V/-3V with the TL431 voltage reference IC.

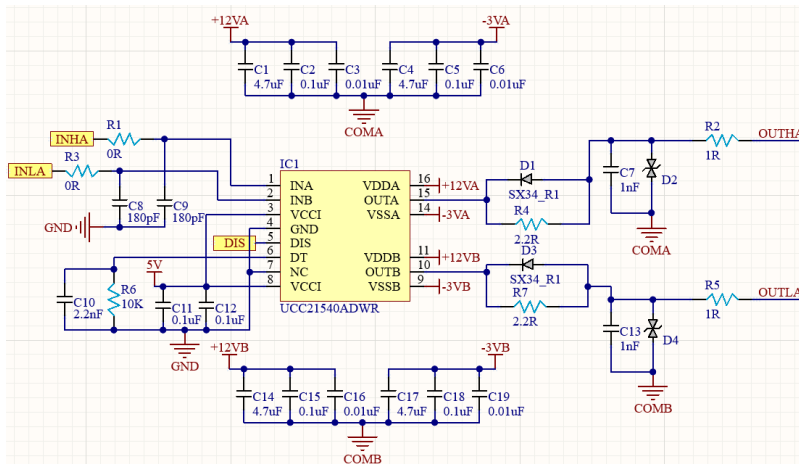


Figure 7.13. Half Bridge MOSFET Driver Circuit

### 7.1.5. Control Card

In this section, information about the control card of ERU is given.

#### 7.1.5.1. Microprocessor Selection

STM32F334C8 processor is used as microcontroller. The built-in HRTIM feature allows phase shifting while driving full bridge MOSFETs. This microcontroller was chosen because of its HRTIM feature. One analog input is reserved for temperature measurement. Two digital pins are used to operate the fan and relay.

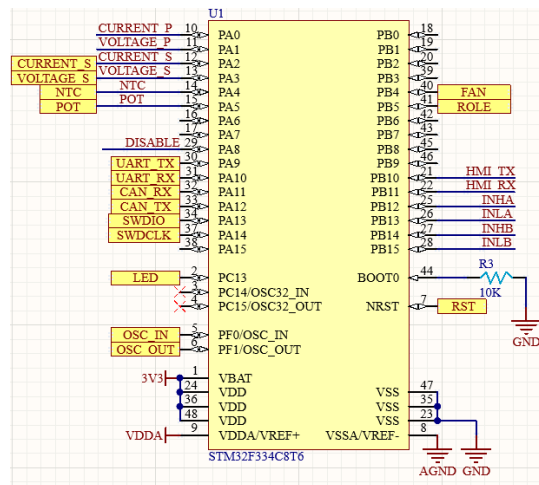


Figure 7.14. MCU Pin Schematic

#### 7.1.5.2. Isolated CAN Communication

Together with SN6505 transformer driver, isolated 760390012 SMPS transformer, TPS76350-Q1 voltage regulator, ISO1050 isolated CAN transfer IC, an isolated CAN communication system was created from other components of the card. The schematic of the mentioned CAN Communication circuit is shown in Figure 7.15.

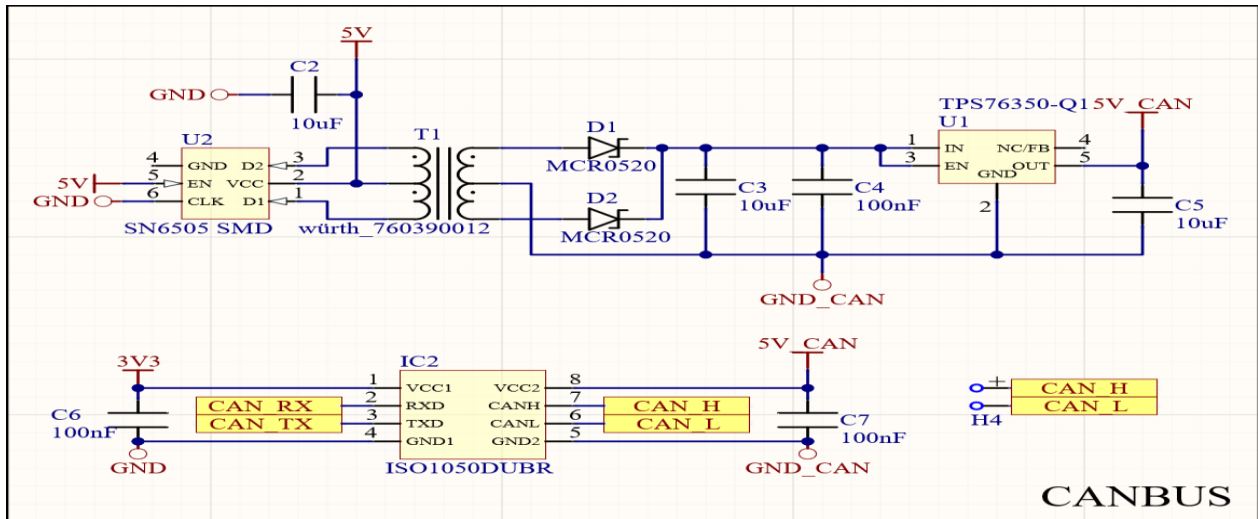


Figure 7.15. Isolated CAN Communication Schematic

### 7.1.5.3. Isolated UART Communication

ERU also communicates with the PC with the CH340 USB to UART converter on it. ADUM1201 UART isolator IC is used to provide isolation between ERU and the PC. Isolated UART communication circuit is shown in figure 7.16.

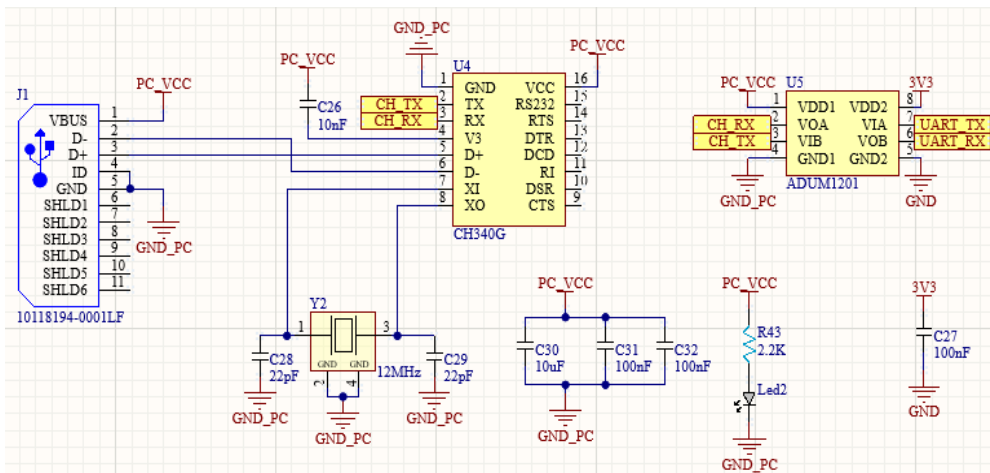


Figure 7.16. Isolated UART Communication

### 7.1.6. Control Algorithm

The STM32F334C8 processor on the control card has a high-resolution timer unit. This timer has hardware dead time support.  $PWM_{HS1}$  and  $PWM_{LS1}$  are connected to channel C of timer unit and channel D of timer  $PWM_{HS2}$  and  $PWM_{LS2}$ . 250ns dead time is given between high side and low side. PWMs work at 45% occupancy rate and their values are fixed.

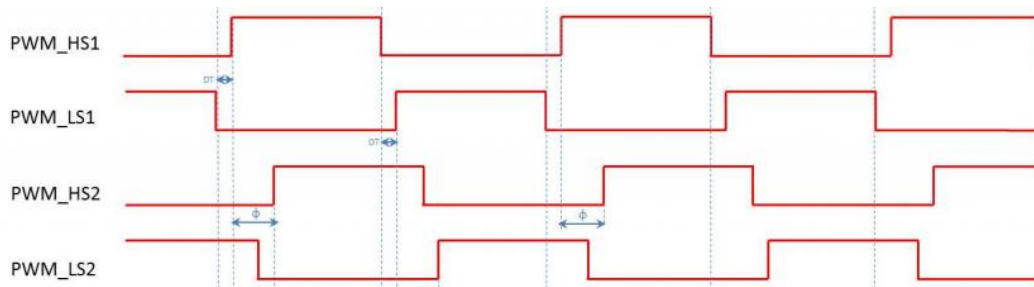


Figure 7.17. PWM Waveforms

The phase shift is created by the C and D channels of the microcontroller. Hardware asymmetrical PWM output can be obtained.

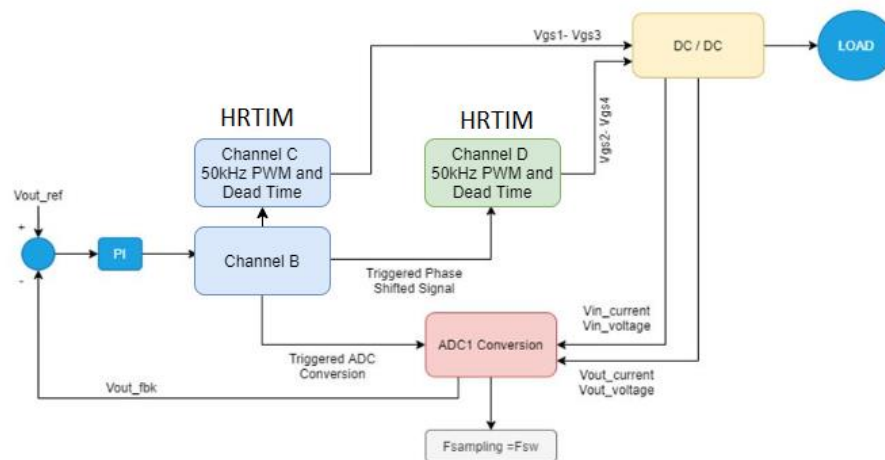


Figure 7.18. Block Diagram for DC/DC Converter Control

At the same time, current and voltage readings are performed when power is transferred.

The phase shift is adjusted based on the output voltage. The PI structure was needed to adjust the output voltage.

Error codes have been created in order for the device to protect itself and give information to the outside. When the system goes into error, it generates an error code and displays this error on the HMI screen and informs the VCU with CAN BUS.

Fault	Error Code
DCDC_NO_ERROR	0x0000
DCDC_OUT_OVER_VOLT	0x0002
DCDC_SHORT_CIRCUIT	0x0004
DCDC_OVER_CURRENT	0x0008
DCDC_OVER_TEMP	0x0009
DCDC_IN_UNDER_VOLT	0x0010
CANBUS_COMM_ERR	0x0012

Figure 7.19. Fault Code Table

DC/DC makes presets when first powered on. If the settings have been made successfully, it will start.  $V_{OUT\_REF}$  is checked. When the battery connection is made, the system starts to

work. If there are situations that will prevent the system from working, the system will crash and turn itself off.

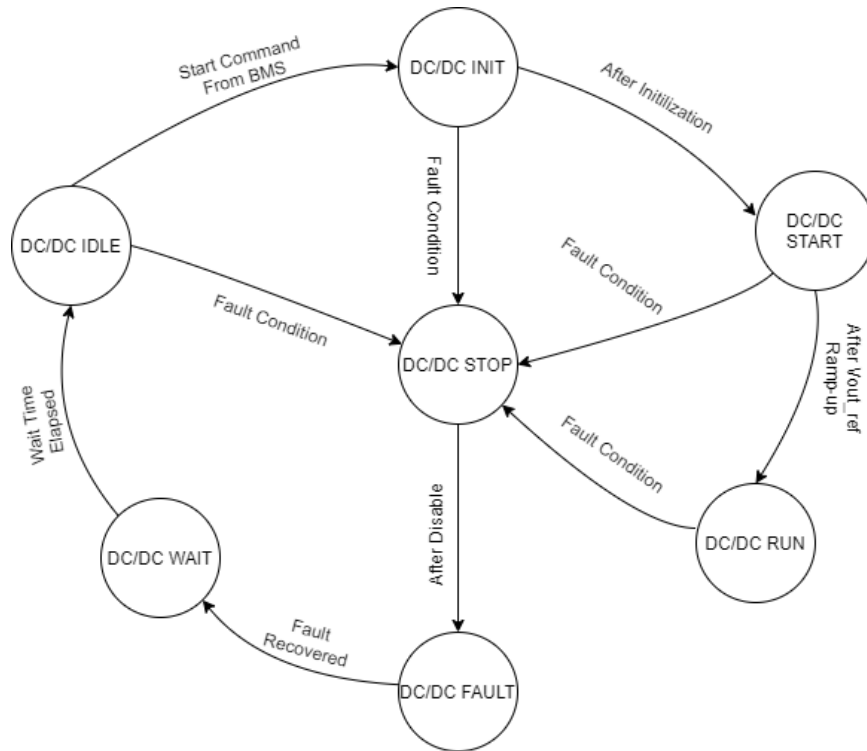


Figure 7.20. State Machine

ADC1 unit reads current and voltage while ADC2 unit reads temperature data. If the temperature is too high, the system will turn itself off again.

## 7.2. Simulation Studies

In this section, circuit analyses is shown. Analyses were made in TI Tina.

### 7.2.1. EMI Filter

EMI Filter is shown in Figure 7.21. The result of the analysis is shown in Figures 7.22 and 7.23. As seen in the graph, the gain of the filter decreases as the frequency increases.

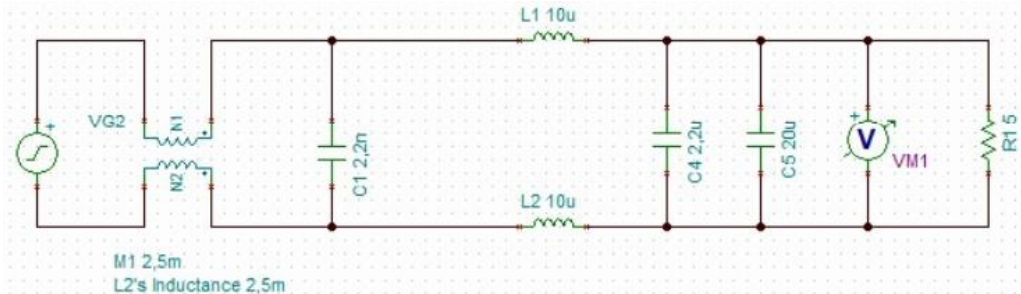


Figure 7.21. EMI Filter

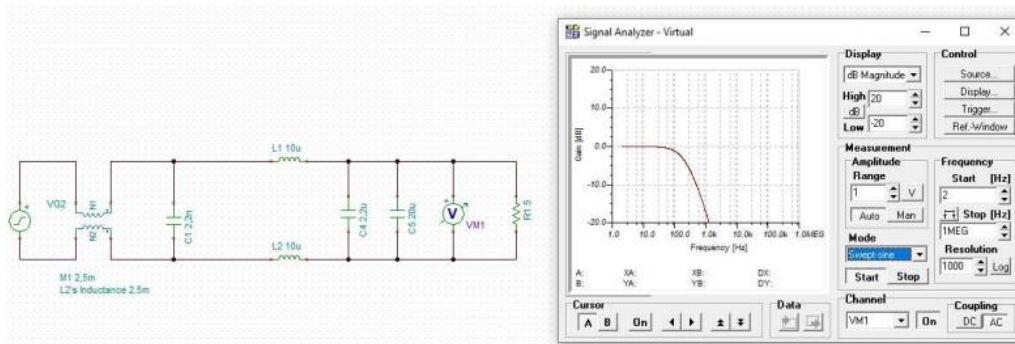


Figure 7.22. EMI Filter Analysis Result

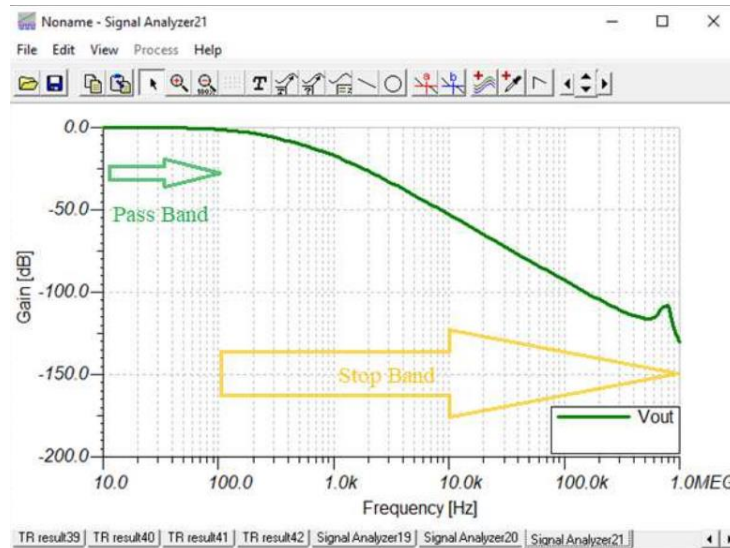


Figure 7.23. EMI Filter Analysis Result

### 7.2.2. Full Bridge Rectifier

In this section, analysis of full bridge rectifier and precharge circuit is made. Precharge has been deactivated after 15 seconds. Precharge circuit is shown in figure 7.24, precharge analysis is shown in figure 7.25.

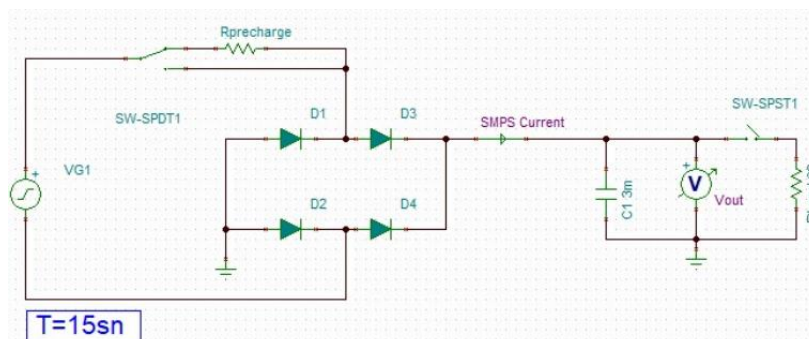


Figure 7.24. Full Bridge Rectifier with Precharge Resistor Circuit

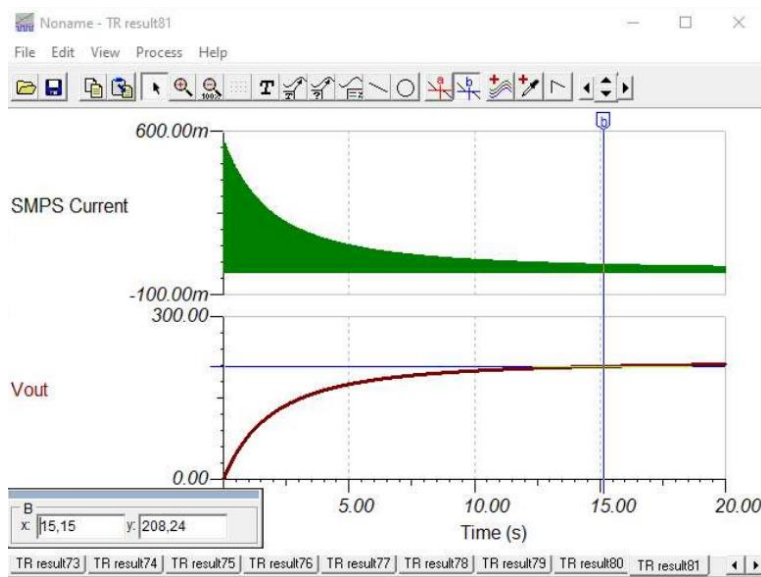


Figure 7.25. Full Bridge Rectifier with Precharge Resistor Circuit Analysis Result

### 7.2.3. DC-DC Converter Card

The circuit designed in the full bridge converter section has been analyzed. ZVS will be used as the switching method. The circuit diagram is shown in Figure 7.26.

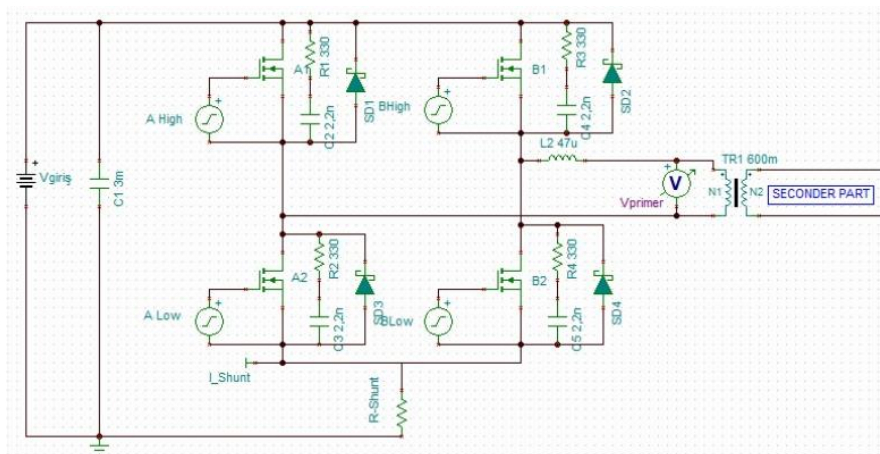


Figure 7.26. Full Bridge Conv. Circuit

In Figure 7.27, Figure 7.28. and Figure 7.29. PWMs and primary voltage of the transformer are shown according to different phase states.

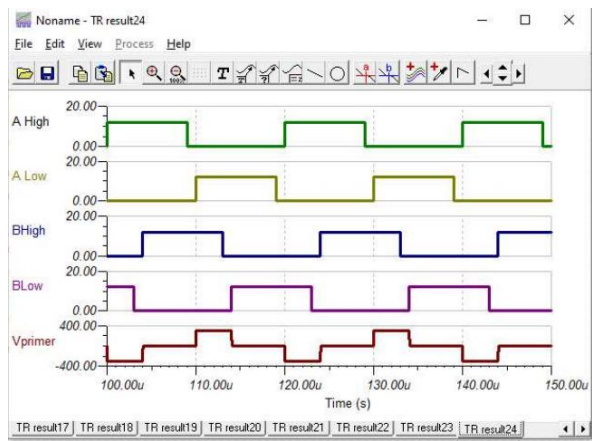
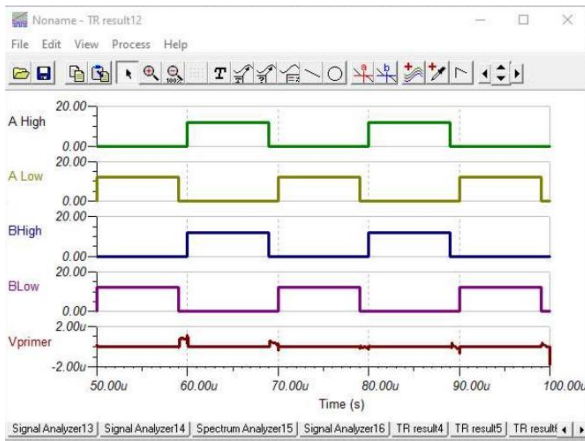


Figure 7.27. Phase shift  $t_d=0\mu s$  Figure 7.28. Phase shift  $t_d=4\mu s$

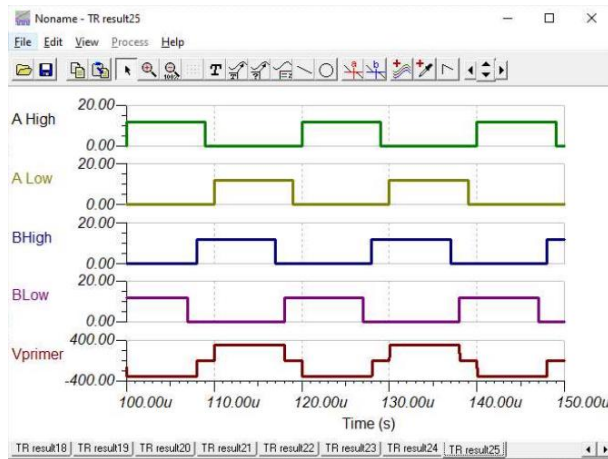


Figure 7.29. Phase shift  $t_d=8\mu s$

The full bridge rectifier at the transformer output is shown in Figure 7.30. Circuit analysis is shown in Figure 7.31.

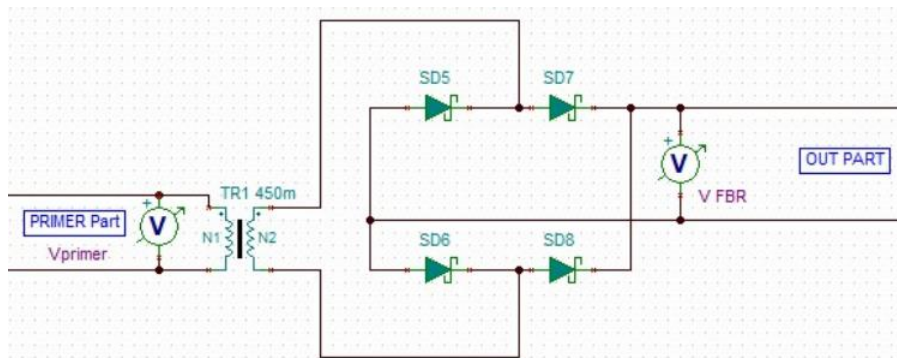


Figure 7.30. Full Bridge Rectifier Circuit of Second Part

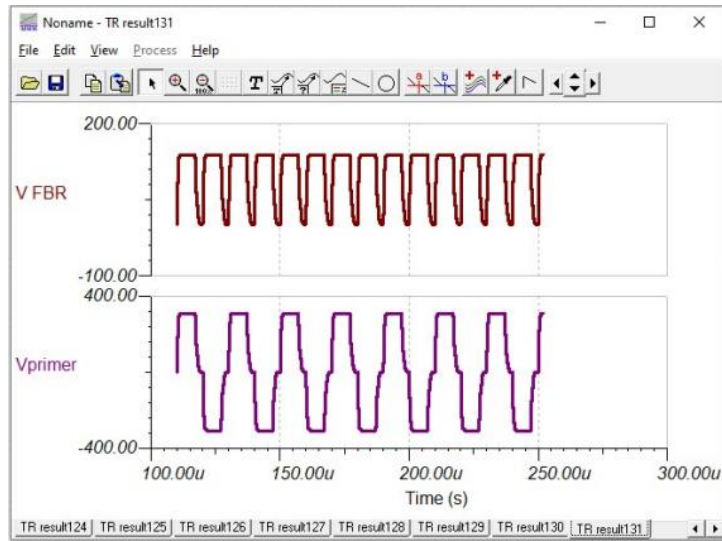


Figure 7.31. Result of Full bridge Rectifier Circuit Analysis of Second Part ( $f=50\text{ kHz}$   
 $t_d=8\mu\text{s}$ )

### 7.3. Production Studies

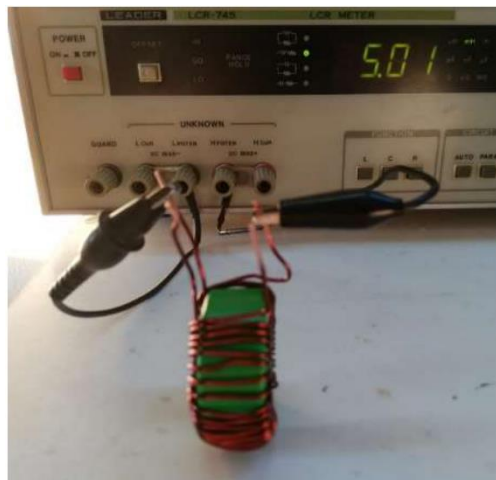


Figure 7.32. Common Mode Choke Inductor

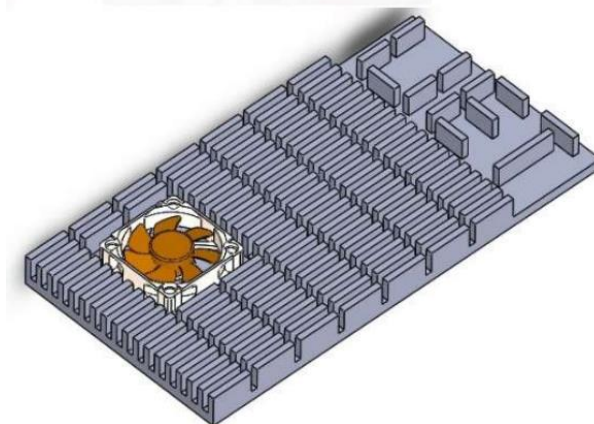


Figure 7.33. Charger Heatsink

## 7.4. Test Results

Test results are shown in this section.



Figure 7.34. PWM  $t_d = 0\mu s$



Figure 7.35. PWM  $t_d = 4\mu s$



Figure 7.36. Primer Voltage



Figure 7.37. Primer Voltage

## 7.5. PCB Designs

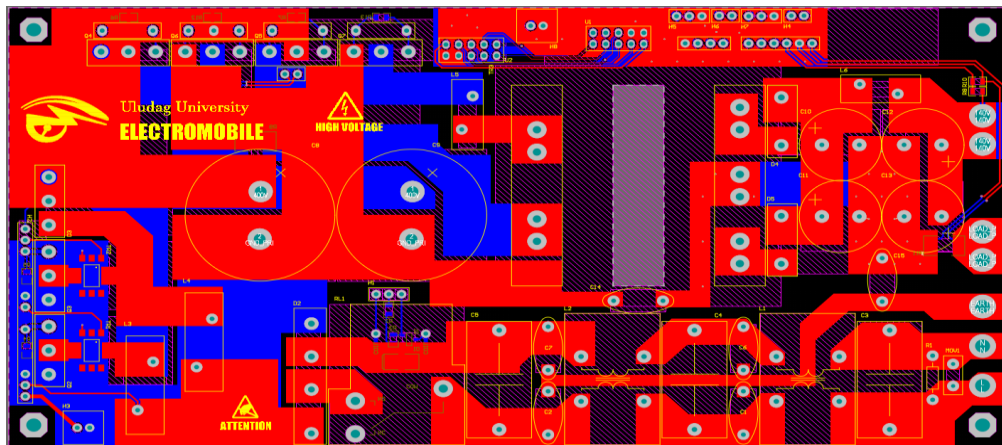


Figure 7.38. Power Card 2D

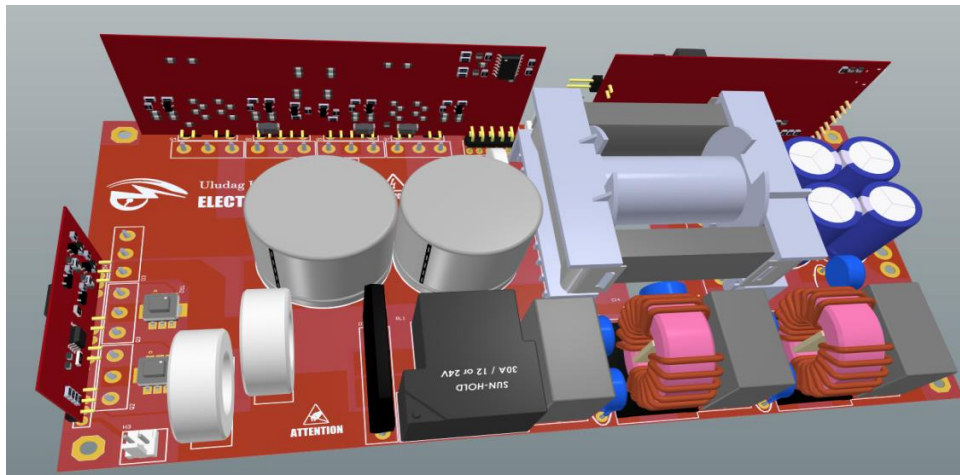


Figure 7.39. Power Card 3D

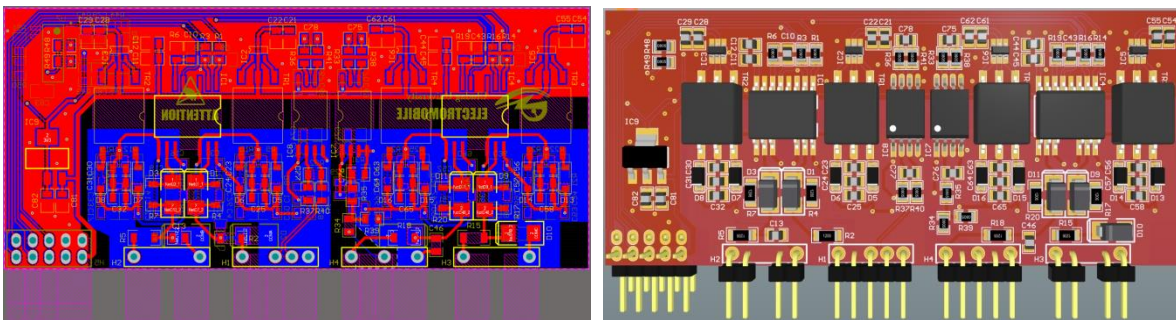


Figure 7.40. Predrive Card

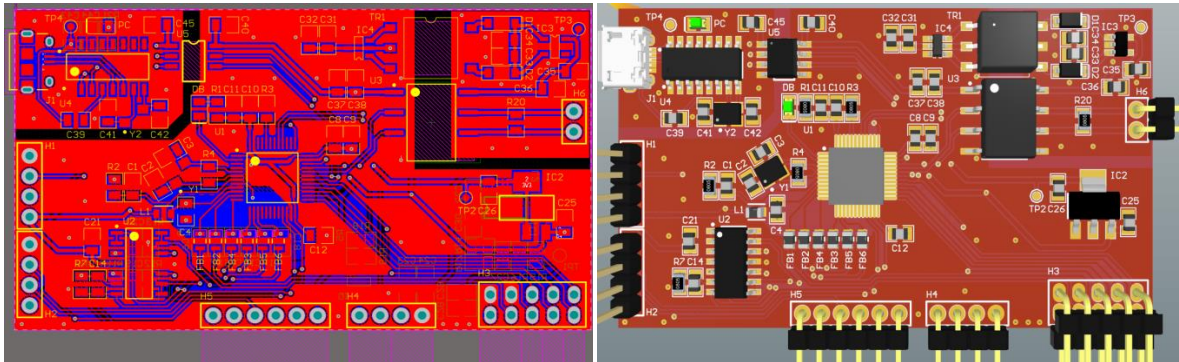


Figure 7.41. Control Card

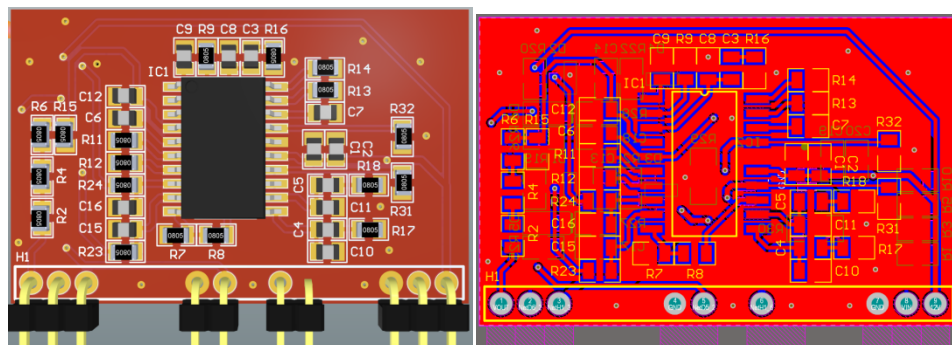


Figure 7.42. PFC Card

		<b>Previous Design</b>	<b>Current Design</b>
<b>Circuit Topology</b>	:	Phase Shifted Full Bridge Conv	Phase Shifted Full Bridge Conv
<b>Power</b>	:	1500W	1500W
<b>Output Voltage Range</b>	:	2X70V	140V
<b>Output Current Ripple</b>	:	%20	%20
<b>Input Power Factor</b>	:	NaN	0.99
<b>Power Conversion Efficiency</b>	:	NaN	NaN
<b>PWM Controller IC</b>	:	STM32F103RET6	STM32F334C8T6
<b>Protection Circuits / Components</b>	:	Current and Voltage control	Current and Voltage control
<b>PCB Size</b>	:	200mmx100mm, 150mmx100mm	200mmx100mm

<https://we.tl/t-nVaK2uU3I4>

## 8. Energy Management System

		Previous Design	Current Design
Circuit Topology	:		
Power	:		
Input Voltage Range	:		
Output Voltage Range	:		
Power Conversion Efficiency	:		
PWM Controller IC	:		
Semiconductor Power Switches	:		
Protection Circuits / Components	:		
PCB Size	:		

## 9. Battery Packaging

### 9.1. Properties of Cells

#### 9.1.1. Electrical Properties of Cells

On the TÜBİTAK Efficiency Challenge Electric Vehicle Races which is the 2021 Race Year, were used in the battery pack prepared 256 Panasonic NCR18650GA batteries, 32 series and 8 parallel. A cell has a nominal voltage of 3.6 V and a maximum voltage of 4.2 V. A maximum of 10 A current can be drawn from Panasonic NCR18650GA batteries during discharge. The maximum current for charging is determined as 1.475 A.

Figure 9.1 shows the technical characteristics of the cells used in the battery pack.

Specifications		
Rated capacity <sup>(1)</sup>		3300mAh
Capacity <sup>(2)</sup>	Minimum	3350mAh
	Typical	3450mAh
Nominal voltage		3.6V
Charging	Method	CC-CV
	Voltage	4.20V
	Current	Std. 1475mA
	Time	Std. 270 min.
Weight (max.)		48.0g
Temperature	Charge	10 to +45° C
	Discharge	-20 to +60° C
	Storage	-20 to +50° C
Energy density <sup>(3)</sup>	Volumetric	693 Wh/l
	Gravimetric	224 Wh/kg

Figure 9.1. Panasonic NCR18650GA Technical Data

#### 9.1.2. Thermal Properties of Cells

Keeping the battery at optimum operating temperatures is very important for its efficiency and long-term health. In Figure 9.2, the temperature values they reach according to different discharge currents from the cells and the discharge characteristics of their capacity are shown. Panasonic NCR18650GA batteries reach approximately 38°C when fully discharged in a 25°C environment with 4 A current sampling.

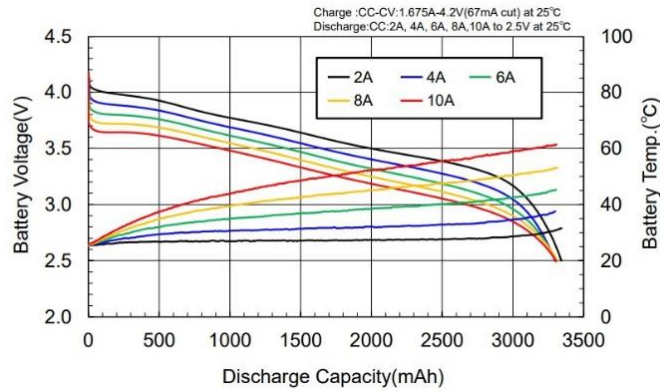


Figure 9.2. Temperature Characteristic of Panasonic NCR18650GA Batteries

### 9.1.3. Mechanical Properties of Cells

Panasonic NCR18650GA batteries are energy-dense and lightweight for their size and weight. Today, 18650 li-ion batteries are used in almost all electric vehicles in mass production. One of these batteries has a height of 65 mm, a width of 18 mm and a weight of 48 g.

Figure 9.3 shows the geometry of Panasonic NCR18650GA batteries.

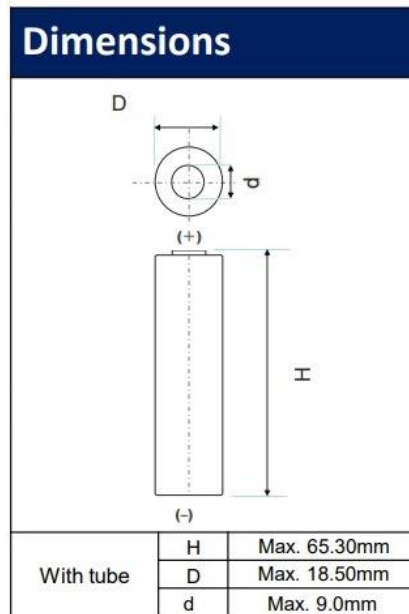


Figure 9.3. Geometry of Panasonic NCR18650GA Batteries

## 9.2. Battery Pack Features

The total nominal output voltage of the prepared package is 115.2 V, and the maximum output voltage is 134.4 V. A total of 3041 Wh energy was obtained with 32 serial and 8 parallel connections. The charging current is 1.475 A for a cell as standard. Since there are 8 parallel cells in the battery pack, the charging current is  $8 \times 1.475 = 11.8$  A. Since the discharge current is 10 A per cell in the batteries used, it is found as  $8 \times 10$  A = 80 A with 8

parallel cells. The battery pack weight is approximately 15 kg with 256 batteries and fasteners.

An 80 A fuse is installed against damage to other system components against high current drawn from the battery. Figure 9.4 shows the 80 A midi fuse used. In addition, this insurance meets automotive standards.

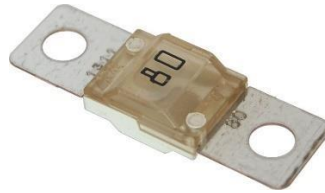


Figure 9.4. 80 A Midi Fuse

A contactor TYCO Electronics LEV100 was shown in figure 9.5.



Figure 9.5. 100A Contactor

### 9.3. Material Specifications of Battery Pack

The battery case is made of 1 mm thick sheets. It is covered with fiberglass material to gain strength and insulation properties. Fiberglass plates are placed so that the battery cells do not touch each other. A fire blanket is laid inside the fiberglass box. The fire blanket is both fireproof and electrically proof.

#### 9.3.1. Electrical Characteristics of Battery Pack Material

Fiberglass is a good electrical insulator even at low thickness. This property of fiberglass makes it suitable for electromagnetic windows.

#### 9.3.2. Thermal Properties of Battery Pack Material

fiberglass is still a very good insulator, though. But if the heat gets hot enough, it will melt. Fiberglass cloth has a melting point is 1121 C. Fiberglass has no true melting point, but it has a softening point. Since fiberglass is a mineral material, it is naturally incombustible. It does not propagate or support a flame. It does not emit smoke or toxic products when exposed to heat. Fiberglass has low thermal conductivity making it highly useful in the building industry.

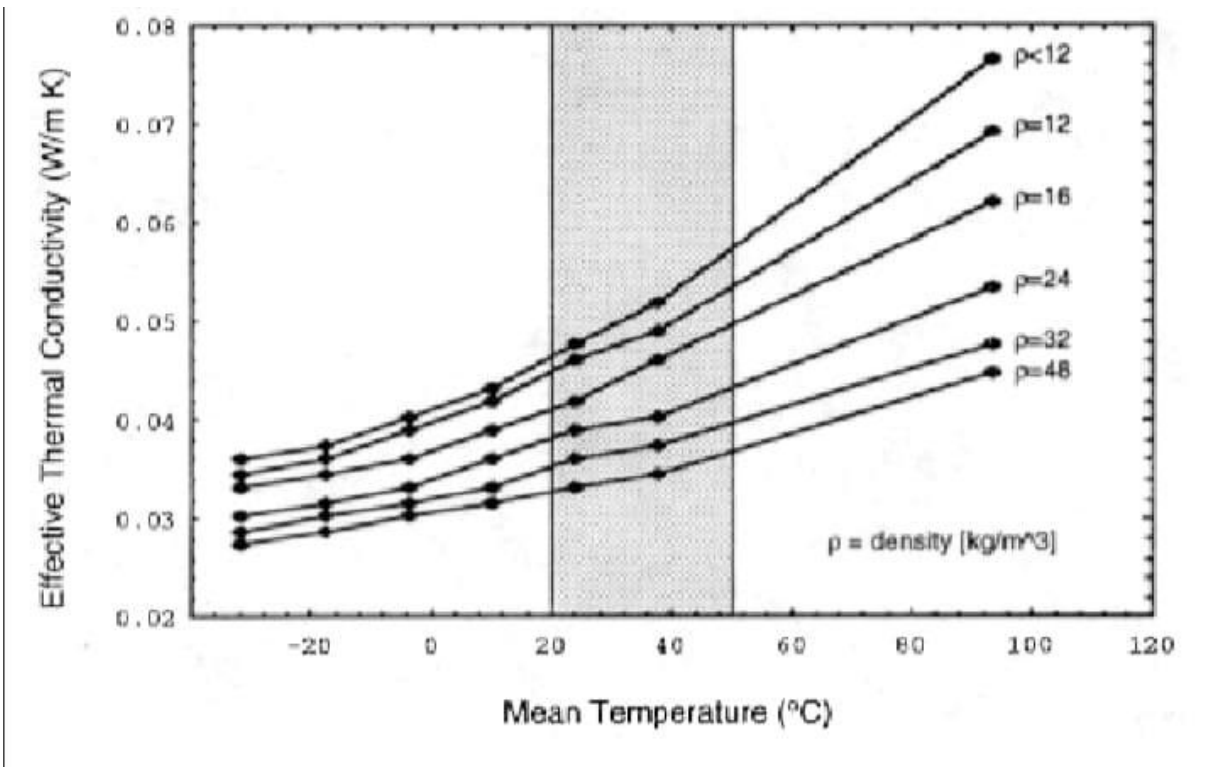


Figure 9.6. Thermal Conductivity - Mean Temperature

### 9.3.3. Mechanical Properties of Battery Pack Material

Fiberglass is not sensitive to variations in temperature and hygrometry. It has a low coefficient of linear expansion. Fiberglass has a specific resistance greater than steel. So, it is used to make high-performance. Figure 9.7 shows the properties of Fiberglass.

## Fiberglass (FRP) Properties

Typical Fiberglass Properties	
Flexural strength, psi	16,000 to 32,000
Flexural modulus, psi	0.8 to 1.4 x10 <sup>6</sup>
Tensile strength, psi	9,000 to 18,000
Tensile modulus, psi	0.8 to 1.4 x10 <sup>6</sup>
Elongation	1.0% to 2.5%
Compressive strength, psi	15,000 to 25,000
Impact strength izod, lb./in. of notch	4 to 12
Specific gravity	1.0 to 1.8
Density, lbs./ft. <sup>3</sup>	80 to 110
Continuous heat resistance	150 to 350
Thermal Coefficient of Expansion, in/in/Fx 10-	12 to 20
Barcol hardness	40 to 60

Properties of a typical 1/8" glass mat laminate using specific fire retardant resin	
Flexural strength, psi @ 77 degrees F	28,000
Flexural modulus, psi @ 77 degrees F	1.07 x 10 <sup>6</sup>
Tensile strength, psi @ 77 degrees F	16,800
Elongation	2.2%
Barcol hardness	45 to 50
Glass content	31%
Specific gravity	1.62
ASTM E-84 (tunnel test)	<25
UL Subject 94	V-0

Figure 9.7. Technical Specifications of Fiberglass

### 9.4. Layout and Isolation of Modules and Package

For the prepared battery pack, cells connected in 8 series and 8 parallel were turned into battery packs. Then, from this battery group, 4 series were connected and 32 series and 8 parallel battery packs were obtained.

The safest method for the connection between cells is the spotting method. In the prepared battery pack, the cells were assembled with the spotting method and turned into a battery group and then a battery pack. In the spotting method, nickel-plated metal with a size of 0.15mm x 8mm was used as the cell connector.

Figure 9.8 shows the CATIA drawing for the battery pack with 8 serial and 8 parallel connections.

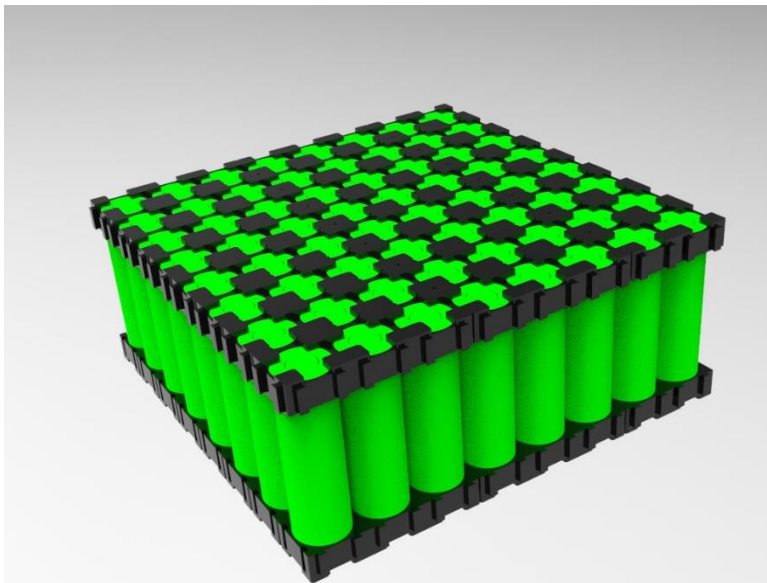


Figure 9.8. Battery Assembly CATIA Drawing

Figure 9.9 shows the drawing of the Whole Battery Pack, including the BMS and cooling fans, in the CATIA program.

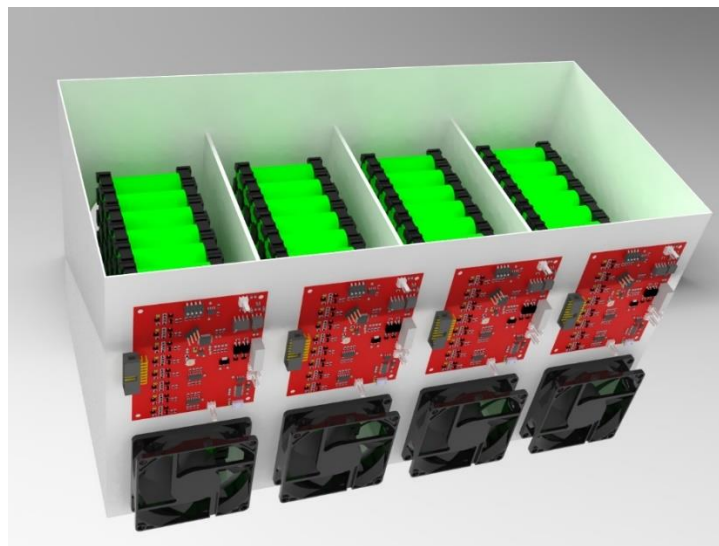


Figure 9.9. Battery Pack CATIA Drawing

### 9.5. Battery Cooling System Design

There are 4 80x80 fans inside the battery box. The Cooling Fan is shown in Figure 9.10. This way each battery cell is cooled evenly. There are 4 grill fans inside the battery box to expel the incoming air.

Figure 9.11 shows the fan grills to expel the incoming air.

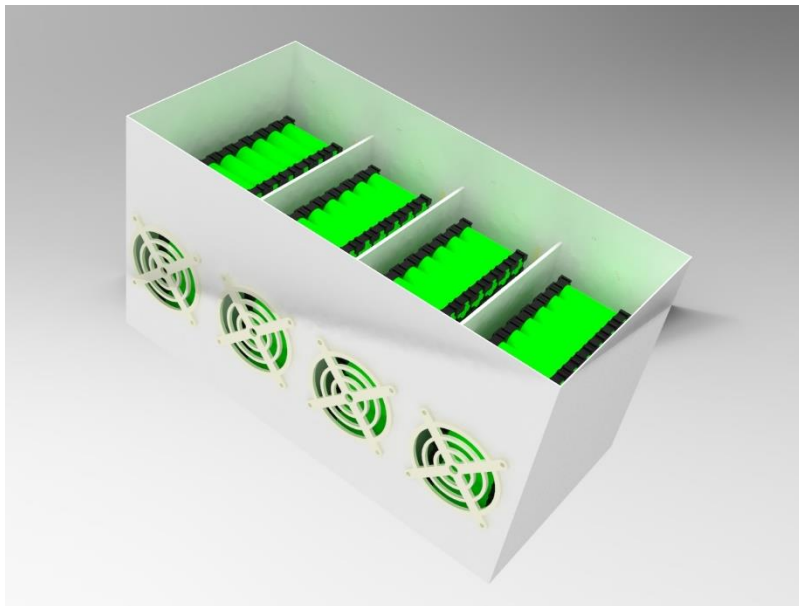


Figure 9.10. Fan Grills of Battery Pack CATIA Drawing

### 9.6. Precharge Circuit Design

The Vehicle Control System (VCU) card activates the precharger first. After the precharge remains active for 3 seconds, it closes the precharger and activates the main contact.

Figure 9.12 shows the drawing of the Precharge circuit in the TINA TI program.

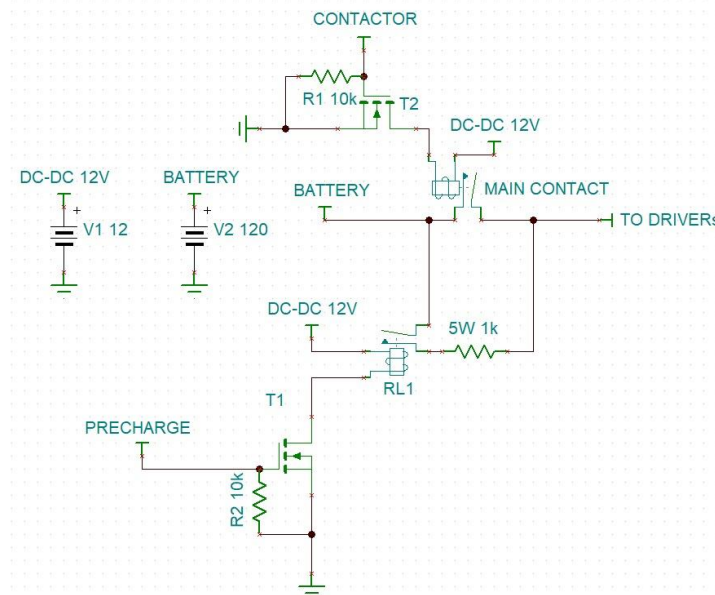


Figure 9.11. Precharge Circuit TINA TI Drawing

## 10. Electronic Differential Application

In this section, the Electronic Differential card designed for the Efficiency Challenge Electric Vehicle Racing 2021 will be discussed. The electronic differential card reads the angle information from the steering wheel and the throttle information from the accelerator pedal analogously. After reading the speed information from the right and left engines, it puts this information into a mathematical process. As a result of this process, it produces two analog signals. These signals go to the drivers controlling the right and left motors. The drivers adjust the throttle of the engine according to this command they receive. This process, which takes place without additional intervention on the drivers, works independently of the driver. The vehicle calculates the average speed information with the speed information it receives from the engines and sends it to the vehicle control system. The schematic and PCB files are attached as PDF files.

Features of the card:

- Isolated CAN Communication,
- Mode select switch,
- Brake pedal detection,
- Independent analog signal generation for motor drivers,
- Independent revolution speed reading,
- Hard acceleration protection,
- External isolated UART Communication with PC

### 10.1. Reading steering wheel angle information

With a potentiometer to be placed on the steering shaft, analog information is read according to the steering angle. The potentiometer is operated with voltage divider logic. The analog signal is passed through the buffer with the help of an operational amplifier before it enters the microcontroller. Steering angle reading circuit is as in figure 10.1.

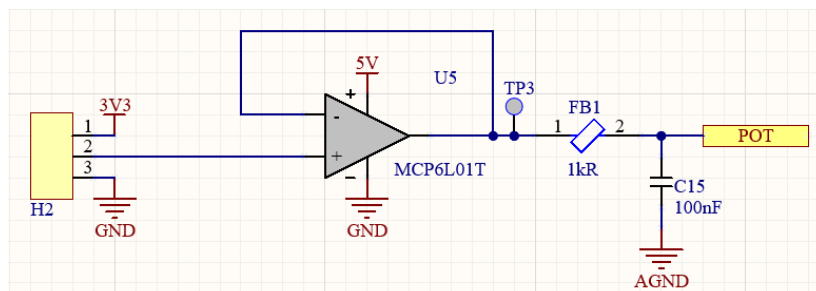


Figure 10.1. Reading Steering Wheel Angle Information

### 10.2. Reading accelerator pedal information

The gas pedal is powered by 5V. The output signal is brought to the reading range of the microcontroller with a voltage divider resistor. The analog signal is passed through the buffer with the help of an operational amplifier before it enters the microcontroller. The accelerator pedal reading circuit is as in figure 10.2.

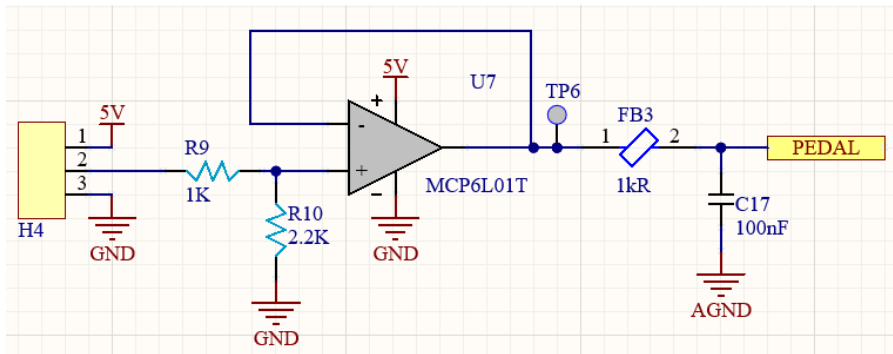


Figure 10.2. Reading Accelerator Pedal Information

### 10.3. Analog Signal Generation for Motor Drivers

The microcontroller generates two different analog signals from the DAC unit after mathematically processing the read information. These signals enter operational amplifiers after passing through the filter. Since the system is designed with 5V-3.3V option, the signals are amplified about 1.45 times. Analog output circuit for motor drivers is as in figure 10.3.

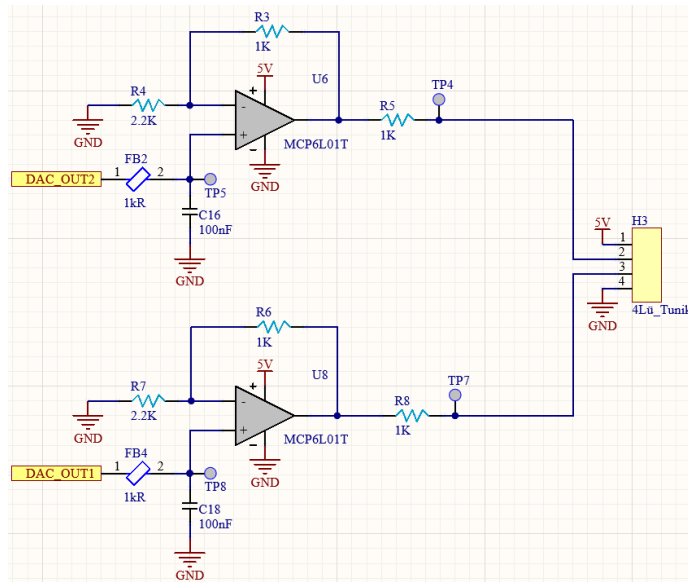


Figure 10.3. Analog Output Circuit For Motor Drivers

## 10.4. Control Algorithm

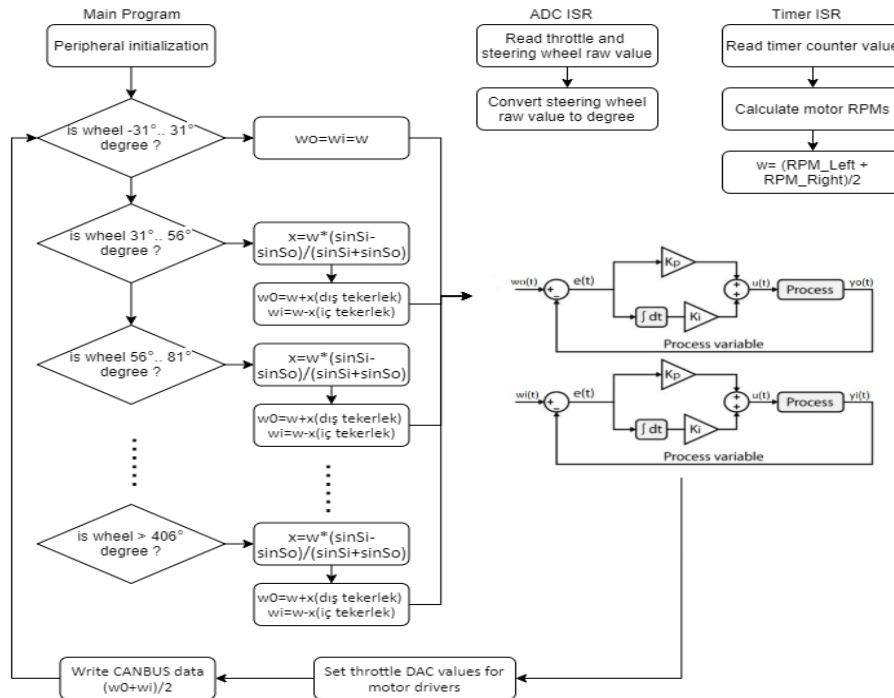


Figure 10.4. Electronic Differential Control Algorithm

## 10.5. PCB Design

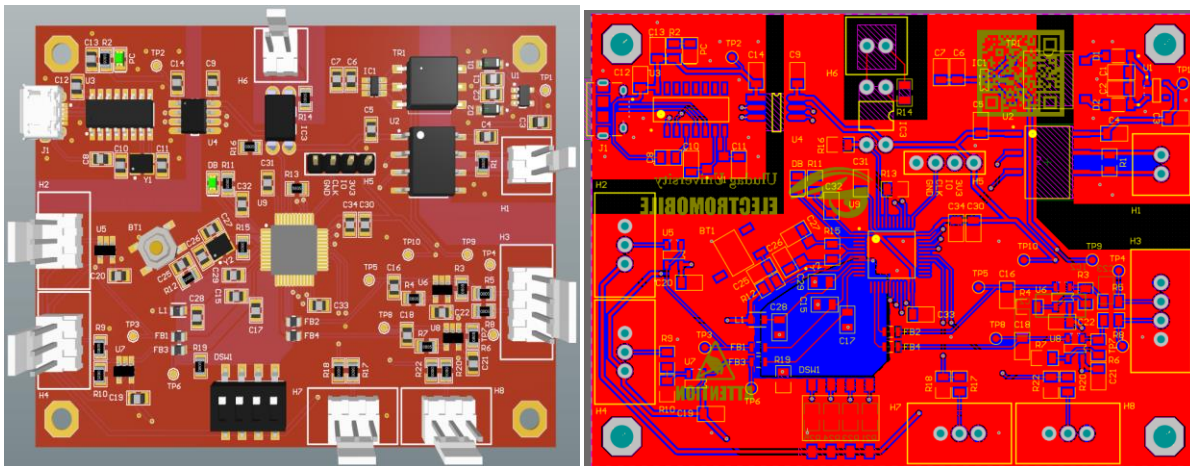


Figure 10.5. Electronic Differential PCB Design

### 10.5.1. Electronic Differential Mechanical Details

We have determined the information we need for the electronic differential application. These are from the steering system designed according to the Ackerman principle, the angles of the inner and outer wheels of the vehicle during turning, the gap of the rack-pinion mechanism in the steering box, which is our domestic design for more accurate operation of the system, and the effect of other gaps in the system on the steering angle, and calculations were made using this information.

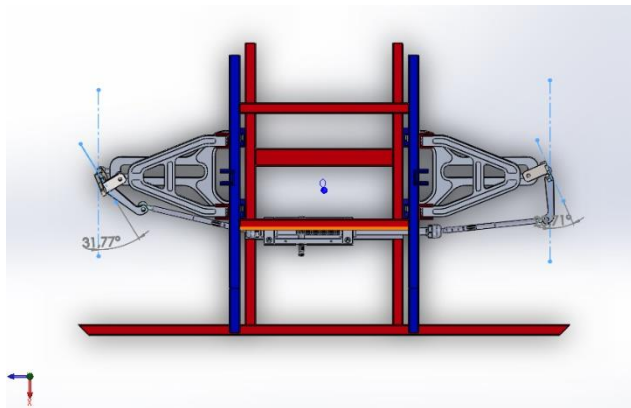


Figure 10.6. Bicycle Model

The gaps in the steering system are measured as  $\pm 12$  degrees on the steering wheel, and the operating mechanism of the system is designed to work with 25 degrees of steering movement sensitivity for more accurate use. According to this design, the speed difference between the rear wheels between 0 degrees and  $\pm 31$  degrees of the steering wheel was neglected. For the subsequent steering angles, the inner and outer angles of the steering wheels were determined separately in each 25-degree range of motion, and the rotation calculations of the rear wheels were made.

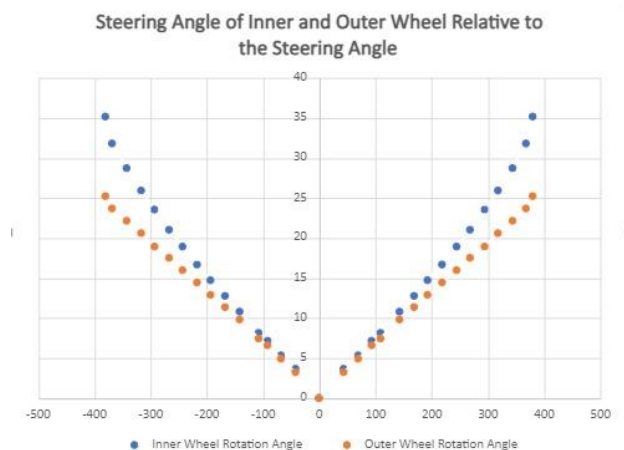


Figure 10.7. Steering Angle of Inner and Outer Wheel Relative to The Steering Angle

During the design of the steering system, the inner and outer wheel rotation angles calculated in the direction of Ackerman were used to calculate the rotational difference that will occur during the rotation of the rear wheels. ( $x$ =rev difference  $w$ =instantaneous angular velocity of the wheels)

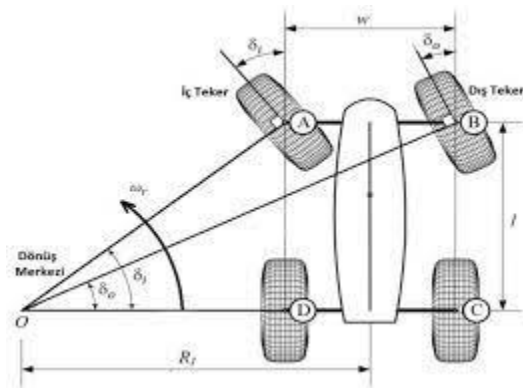


Figure 10.8. Turning Angle Analysis of Inner and Outer Wheels

$$x = \omega \times (\sin \delta_i - \sin \delta_o) / (\sin \delta_i + \sin \delta_o)$$

$$\text{And } \omega_o = \omega + x \text{ and } \omega_i = \omega - x$$

Finally, in order to calculate these calculations correctly by the processor, the steering movement was transmitted to the potentiometer by using a spur gear mounted on the steering shaft for accurate and reliable reading of the steering angle. It was aimed to provide better perception of the potentiometer by choosing a 1:2 ratio straight gear mechanism.

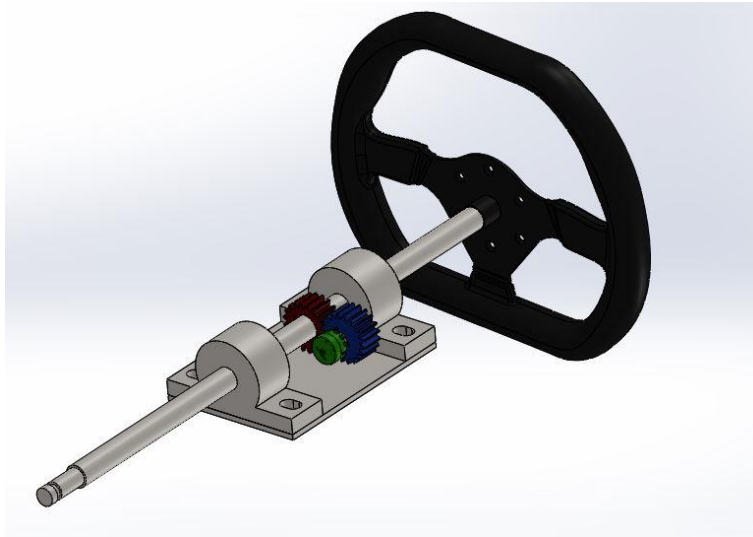


Figure 10.9.

		Previous Design	Current Design
<b>System Topology (Used Sensors, Control Units, Actuators etc.)</b>	:		
<b>Vehicle Model (Kinematic Model, Simple Dynamic Model, Full Vehicle Model etc.)</b>	:		
<b>Control Algorithm</b>	:		
<b>Considered Exceptional Cases and Proposed Design Solutions (Low Adhesion, Split Friction (Mu), Weight Transfer, Acceleration /Deceleration on Curves etc.)</b>	:		
<b>Applied Simulation Scenarios</b>	:		
<b>Performance Results for Simulation Scenarios</b>	:		
<b>Applied Test Scenarios</b>	:		
<b>Performance Results for Test Scenarios</b>	:		

<https://we.tl/t-CPnLIP0LPR>

## 11. Vehicle Control Unit (VCU)

In this section, the Vehicle Control Unit card designed for the Efficiency Challenge Electric Vehicle Racing 2021 will be discussed. The vehicle control system of 2021 consists of 3 different cards. It consists of main control card, I/O card and energy meter. Vehicle Control Unit cards were designed by Altium Designer and circuit analysis was done by Tina Ti. The placement of the cards is shown in Figure 11.1.

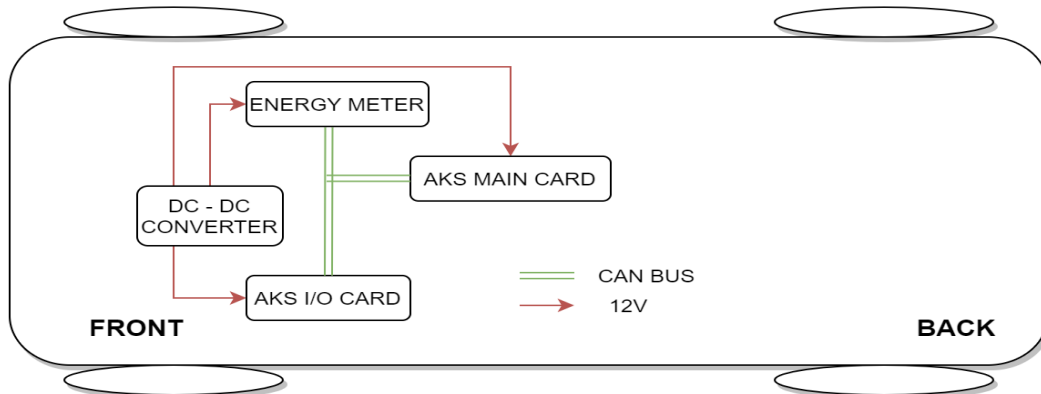


Figure 11.1. In-Vehicle Placement of Cards

### 11.1. Main Control Card

The main control card is the card where the basic in-car algorithm will work. Basic controls will be done by this card and will communicate with the CAN BUS with the other cards. The schematic and PCB files are attached as pdf files.

Features of the card:

- Isolated CAN-BUS protocol for in car communication,
- GSM Communication (Telemetry) with SIM808 Module,
- RF Communication (Telemetry) with XBEE (optional),
- RF Communication (Telemetry) with LORA (optional),
- In-car monitor,
- External isolated UART Communication with PC

#### 11.1.1. Microcontroller Selection

STM32F302C8T6 produced by STMicroelectronics is used. VCU main card, VCU I/O card and Telemetry card use the same microcontroller.

Its main features are:

- 64 KB Flash,
- 16 KB SRAM,
- GPIO capable of 32 external cutting,
- 2 x 12 Bit ADC,
- Internal RTC,



schematic, which assumes the transmitter position in the vehicle, is in Figure 11.4; LoRa schematic is in Figure 11.5; The SIM808 schematic is shown in Figure 11.6. VCU main card and telemetry card use the same wireless communication circuit.

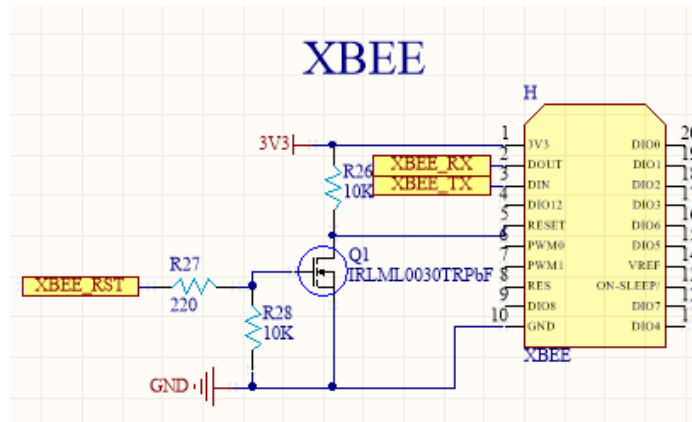


Figure 11.4. XBEE Schematic

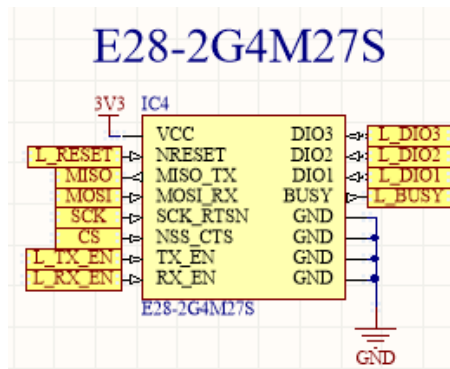


Figure 11.5. LoRa Schematic

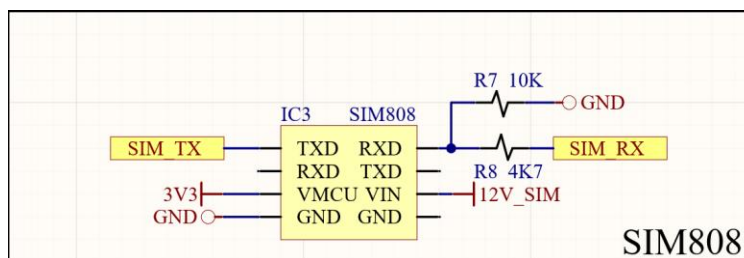


Figure 11.6. SIM808 Schematic

#### 11.1.4. Isolated UART Communication

All cards in the vehicle control system also communicate with the PC with the CH340 USB to UART converter on them. ADUM1201 UART isolator IC is used to provide isolation between vehicle and PC. Isolated UART communication circuit is shown in figure 11.7. VCU main board, VCU I/O board and energy meter use the same UART communication circuit.

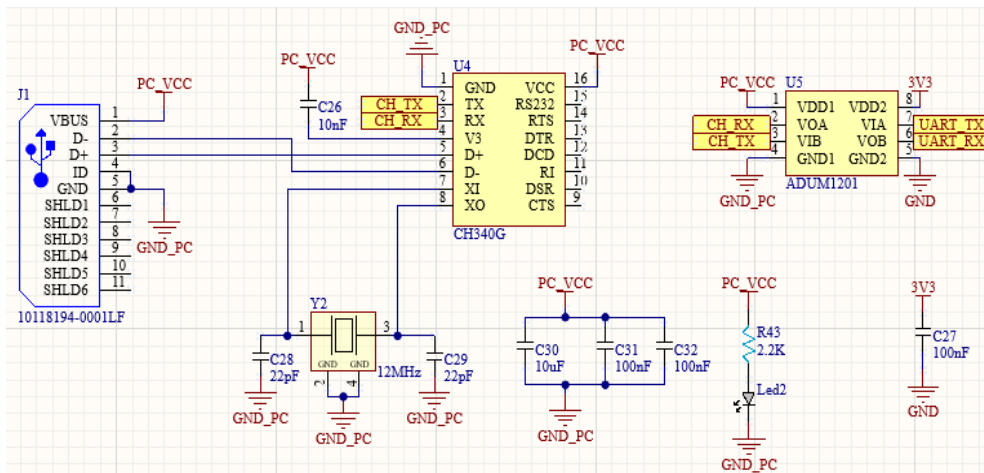


Figure 11.7. Isolated UART Communication

### 11.1.5. Regulators

3.3 Volt and 5 Volt output were obtained with MP1482 buck converters from 12 Volt input to be used in VCU card. Mentioned regulator circuit schematic is shown in Figure 11.8.

Since the SIM808 GSM module board contains a regulator, it is fed from a 12V input. CAN communication system and Dashboard are powered by 5V. Microcontroller and other components are fed with 3.3V.

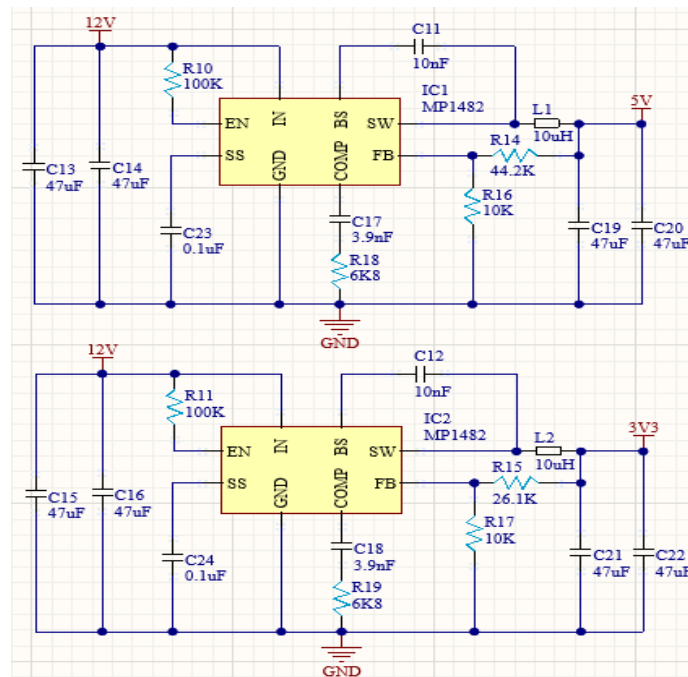


Figure 11.8. MP1482 Buck Converters

### 11.1.6. In Car Monitor (Dashboard)

It acts as the control panel of the vehicle. Analog values such as current, voltage, speed, battery status and temperature; It contains digital values such as horn, wiper and signal. On the left of the screen, there is information from the battery. These are battery voltage, battery charge rate, current drawn, power consumed, battery temperature and energy consumed. In

the lower left part of the screen are the headlight, wiper, main ignition and horn. There are warning signs in the upper middle part of the screen. These are signs indicating high current, high temperature and low voltage conditions. In the middle part, there are time and date data, left signal, right signal, quads, motor temperatures and remaining range. On the right part of the screen, there are motor drivers' temperatures, numerical speed information and a button that opens the battery cells page. cell voltages and temperatures are displayed on the screen. Dashboard screen communicates with VCU via UART protocol. Nextion NX1060P101 smart screen is used as the display panel. Said internal screen design is shown in Figure 11.9.

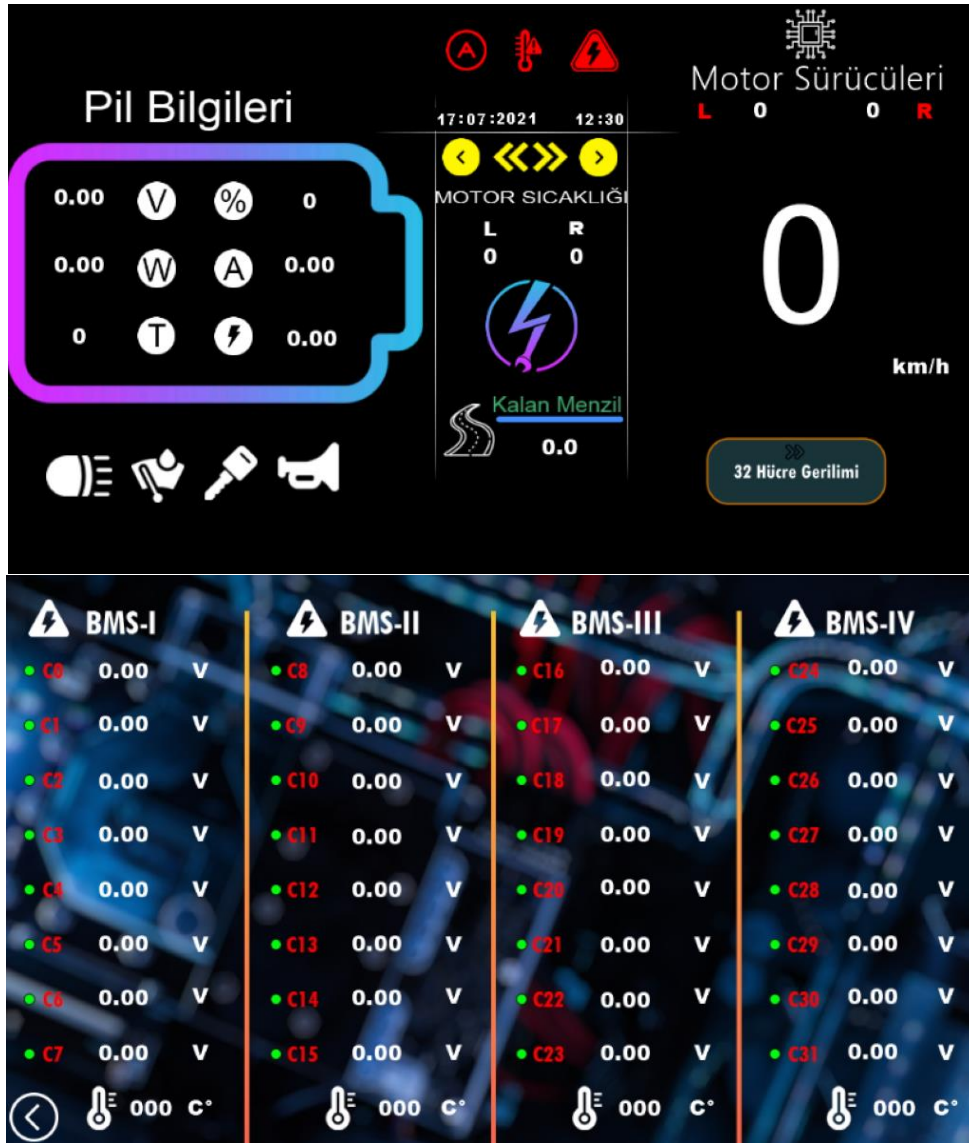


Figure 11.9. In Car Monitor Design

### 11.1.7. Control Algorithm

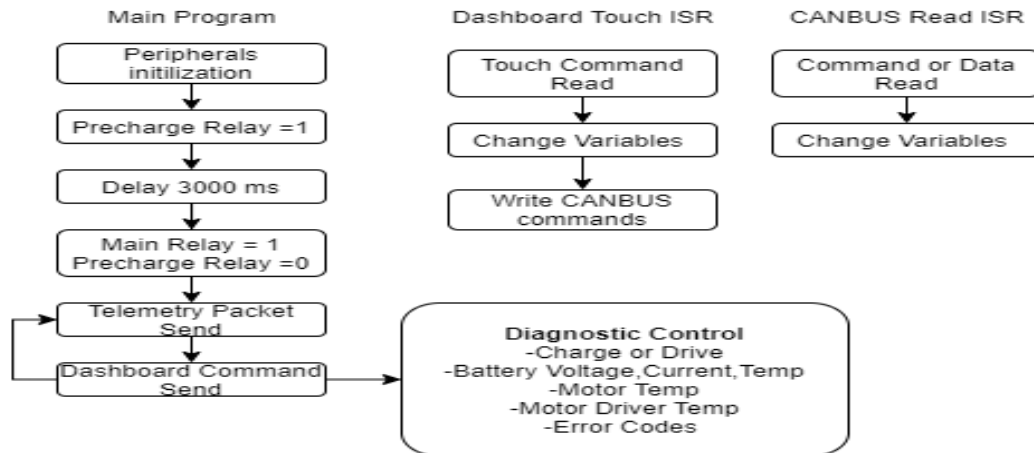


Figure 11.10. VCU Control Algorithm

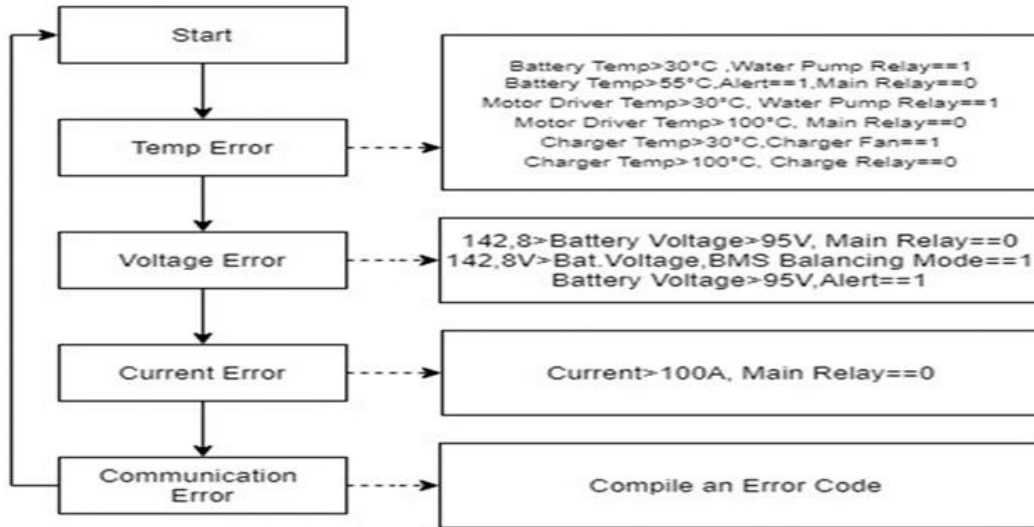


Figure 11.11. Vehicle Error Codes

### 11.1.8. PCB Designs

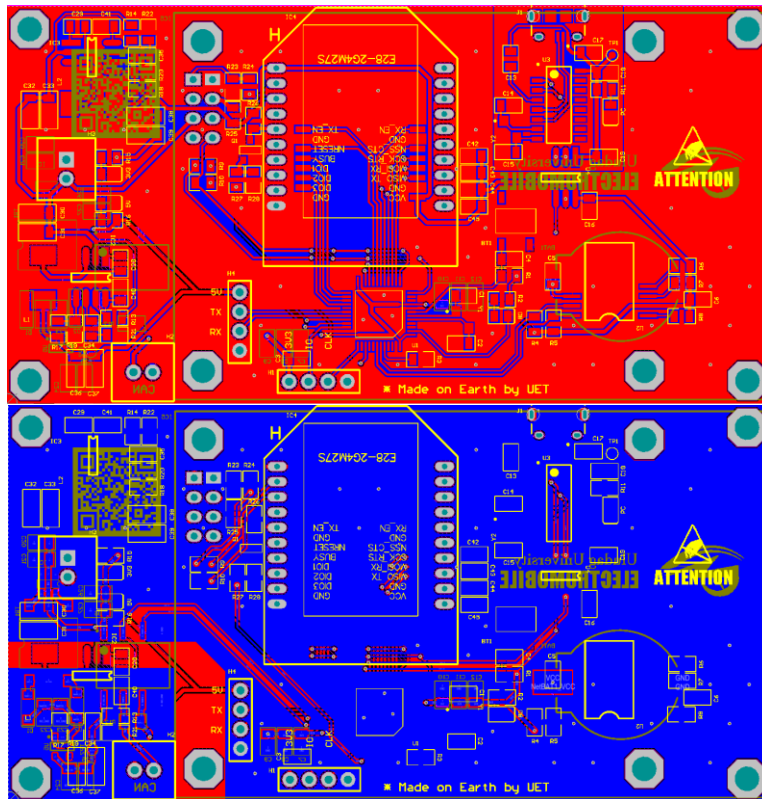


Figure 11.12. VCU Communication Card 2D

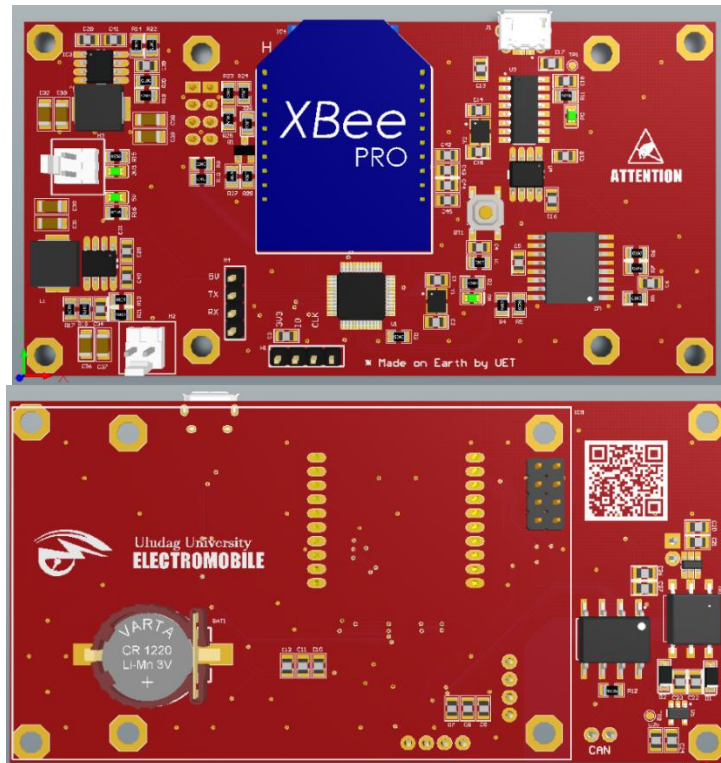


Figure 11.13. VCU Communication Card 3D

## 11.2. VCU I/O Card

In-car accessories will be operated with this card. The I/O card and the main control card communicate with CAN BUS. The main purpose in the design of this card is to reduce the amount of in-car cables and detect errors. The card content is summarized below. The schematic and PCB files are attached as pdf files.

Isolated CAN Communication,

8 pcs digital isolated output,

8 pcs digital isolated input,

4 pcs analog input,

External isolated UART Communication with PC

### 11.2.1. Input and Output

#### 11.2.2. Analog Inputs

Data such as temperature, current, voltage and current battery status in the vehicle; obtained from analog inputs. One analog input circuit diagram is mentioned in Figure 11.14.

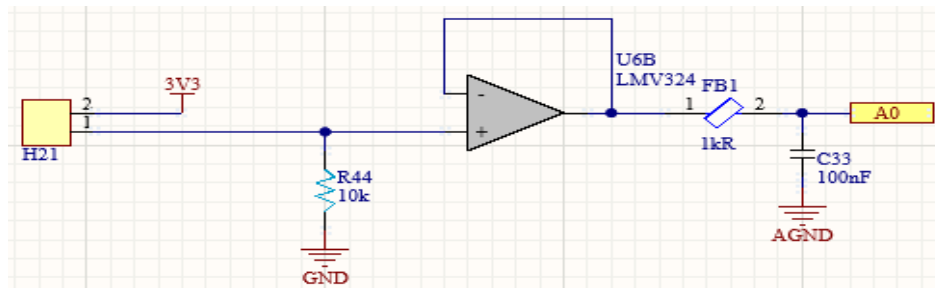


Figure 11.14. Analog Input Schematic

#### 11.2.3. Digital Inputs

Data to be sent digitally such as horn, wiper and signal in the vehicle; is obtained from digital inputs. Each digital input is isolated from the other. One digital input circuit schematic mentioned is given in Figure 11.15.

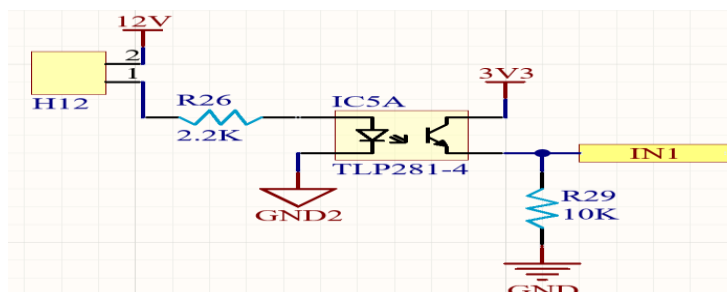


Figure 11.15. Digital Input Schematic

### 11.2.4. Digital Outputs

Data of the parts of the vehicle that will work digitally, such as horn, wiper and signal are obtained from digital outputs. Each digital output is isolated from the other. One digital output circuit schematic is given in Figure 11.16.

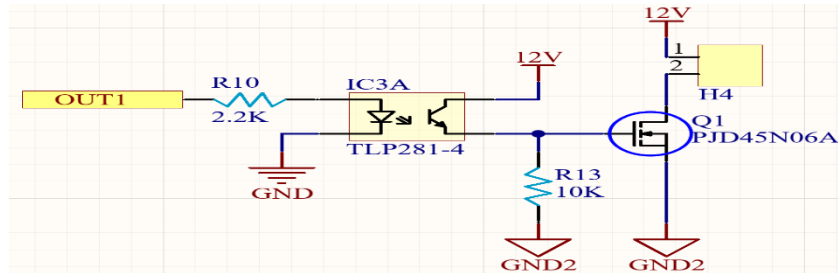


Figure 11.16. Digital Output Schematic

### 11.2.5. Regulators

A 5 Volt output was obtained with MP1482 buck converter from 12 Volt input to be used in VCU card. The 5 Volt output from the MP1482 buck converter has been reduced to 3.3 volts with the AMS1117-3.3 for the supply of the processor and other components. Mentioned regulator circuit schematic is shown in Figure 11.17.

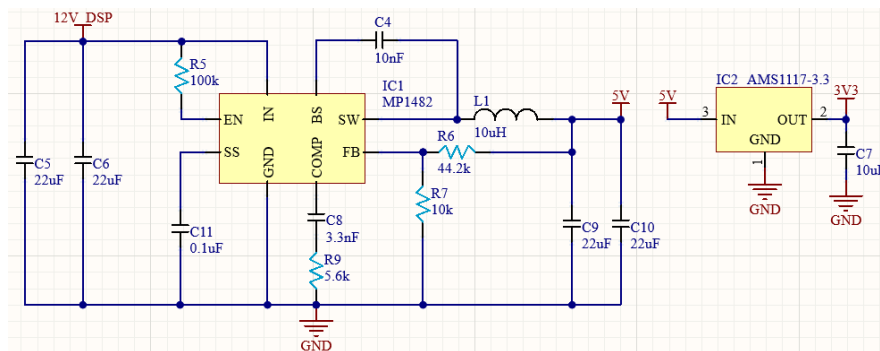


Figure 11.17. Regulator Circuit

### 11.2.6. PCB Designs

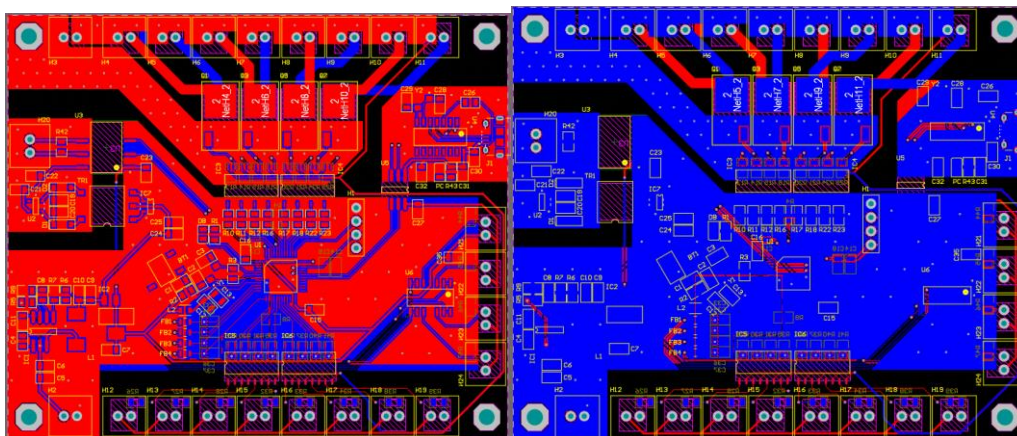


Figure 11.18. VCU I/O Card 2D





### 11.3.3. PCB Design

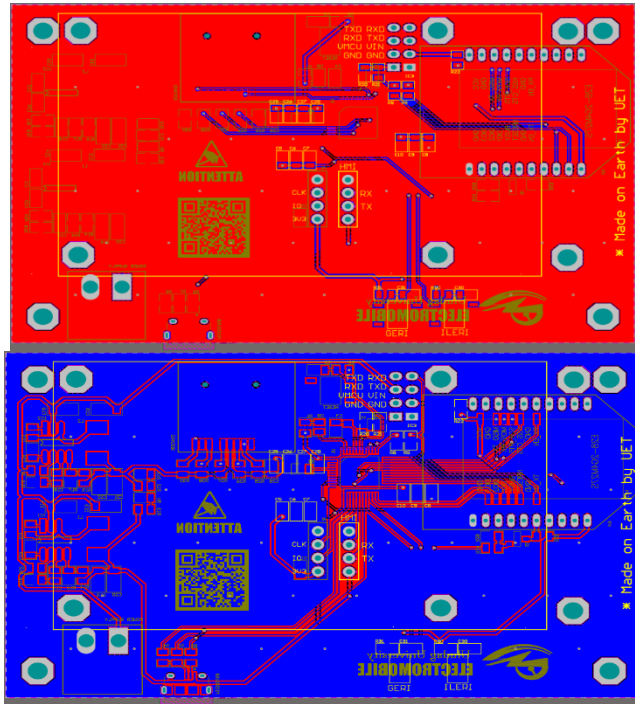


Figure 11.22. Telemetry Card 2D

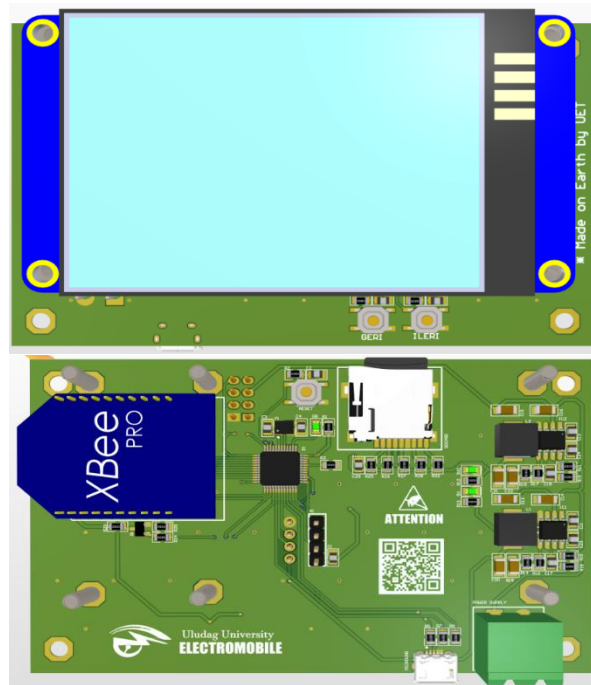


Figure 11.23. Telemetry Card 3D

### 11.4. Energy meter

The energy meter reads the battery voltage and current drawn in isolation from the battery. With these read data, it calculates the power drawn and the energy consumed by the vehicle. It logs the energy consumed via RTC to the SD card. It communicates with the vehicle via CAN communication. It displays the instantaneous current drawn, the total voltage of the battery, the instantaneous power and the energy consumed on the screen. It gives a warning to the driver when excessive current is drawn. It has 0.2% voltage and current accuracy. It was used as the original design in this vehicle. The schematic and PCB files are attached as pdf files.

Features of the card:

- Isolated CAN Communication,
- Isolated Voltage and Current Measurement,
- Internal RTC,
- SD card for logging,
- 1.3inc I2C OLED Display,
- External isolated UART Communication with PC

#### 11.4.1. Microcontroller Selection

STM32F373C8T6 produced by STMicroelectronics is used. STM32F373C8T6 is especially preferred because it contains 16-bit sigma-delta ADC.

Its main features are:

- 3 x 16 Bit sigma-delta ADCs,
- 12 Bit ADCs with 1 MSPS,
- Up to 2 x comparators,
- Up to 3 x 12 Bit DACs,
- 1 x CAN 2.0B,
- 1 x USB 2.0,

### 11.4.2. Isolated Voltage and Current Measurement

In the designed circuit, the current was calculated from the voltage falling on the shunt resistor. The battery voltage was measured with voltage divider resistors. AMC1301 is used for current measurement and AMC1311 is used for voltage measurement. The gain of the AMC1301 operational amplifier is  $A_v = 8.2$  and gain of the AMC1301 operational amplifier is  $A_v = 1$ . The AMC1301 and AMC1311 output an offset 1.44V output signal. It reads differential input from two channels with the sigma-delta ADC inside the microcontroller. It takes the difference of the two channels it reads and converts it to a 16-bit number. In voltage and current measurement, positive and negative polarity signals can be read. Thus, it can be determined which of the production and consumption modes of the vehicle.

Transfer function of the current sense circuit;

$$V_{out} = (I \times R_{shunt}) \times 8.2 \quad (15.1)$$

$$V_{out} = (I \times 500\mu\Omega) \times 8.2 \quad (15.2)$$

The circuit diagram of the current sense circuit was shown in Figure 11.24.

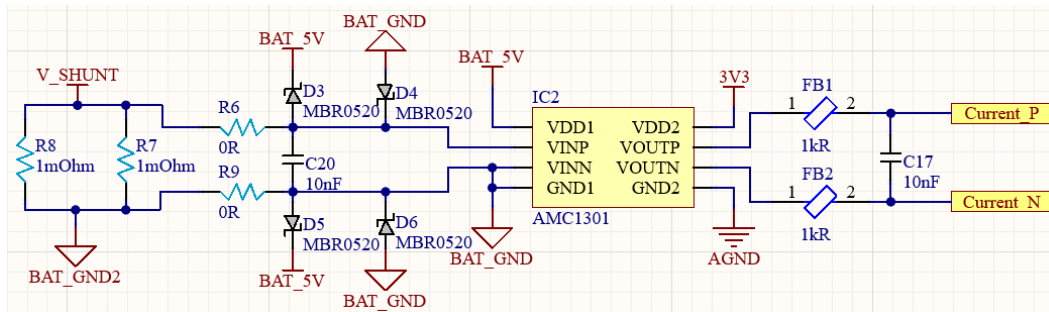


Figure 11.24. Circuit Schema of The Isolated Current Sense

Transfer function of the voltage sense circuit;

$$V_{bat} = V_{out} \times \frac{(10k\Omega + 1M\Omega)}{10k\Omega} \quad (15.3)$$

The circuit diagram of the voltage sense circuit was shown in Figure 11.25.

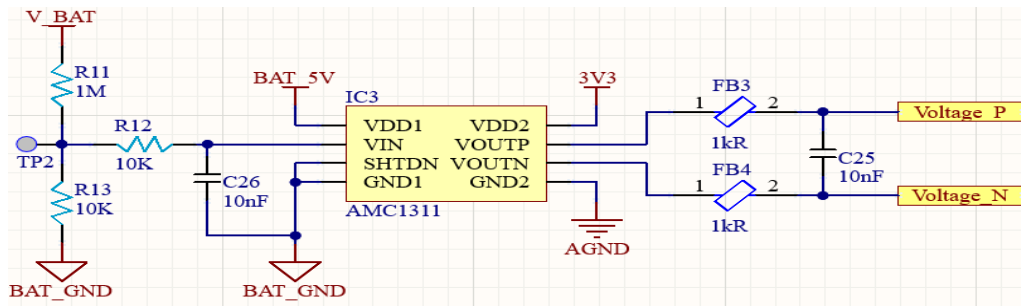


Figure 11.25 Circuit Schema of The Isolated Voltage Sense

In order for the measured signal to be affected by electrical noise as little as possible, filter coils are used as LC low-pass filters. Analog and digital GNDs are connected to each other as a star connection with the help of a 0R resistor.

### 11.4.3. Isolated Power Supply for OPAMPs

SN6505 transformer driver, isolated 760390012 SMPS transformer and TPS76350-Q1 voltage regulator are used for isolated supply for AMC1301 and AMC1311. The power supply circuit diagram set up to read the battery voltage and current in isolation from the battery is shown in Figure 11.26.

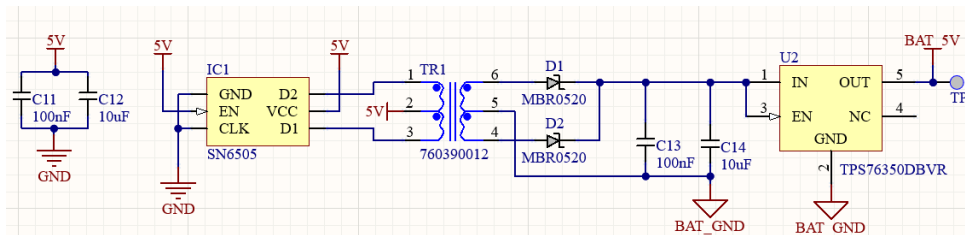


Figure 11.26. Isolated Power Supply for OPAMPs

### 11.4.4. DS3231 RTC and SD Card

RTC and SD card are used to calculate energy and keep logs. The power draw is calculated by multiplying the measured battery voltage and current. The energy consumed is calculated by integrating the power absorbed. The 4 calculated data are saved in the SD card by adding the time and date. If the system does not see the SD card at boot, it does not log. In the program, data is written to the SD card every 250ms by adding time and date information. The circuit diagram for logging is in Figure 11.27.

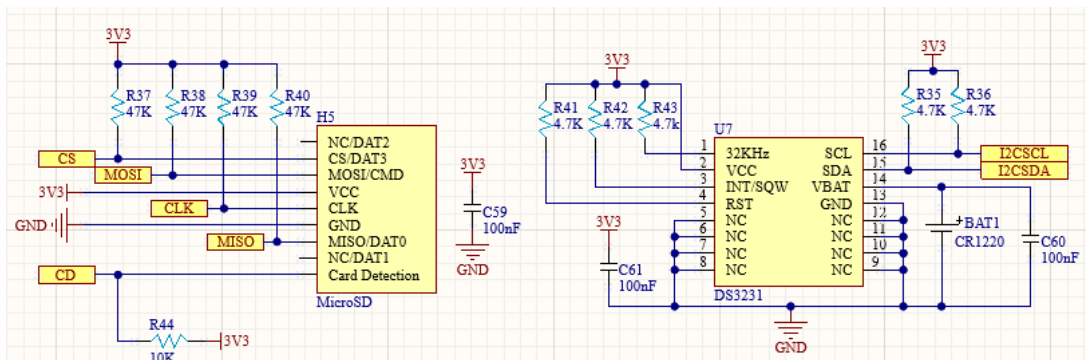


Figure 11.27. DS3231 RTC and SD Card Schema

When the logging process is finished, the .txt file created with the help of the excel program is opened. The “\*” sign is used as a separator. Excel divides the typed data into columns. If desired, these data can be graphed. Below is an example Energy-Time graph created in Figure 11.28.

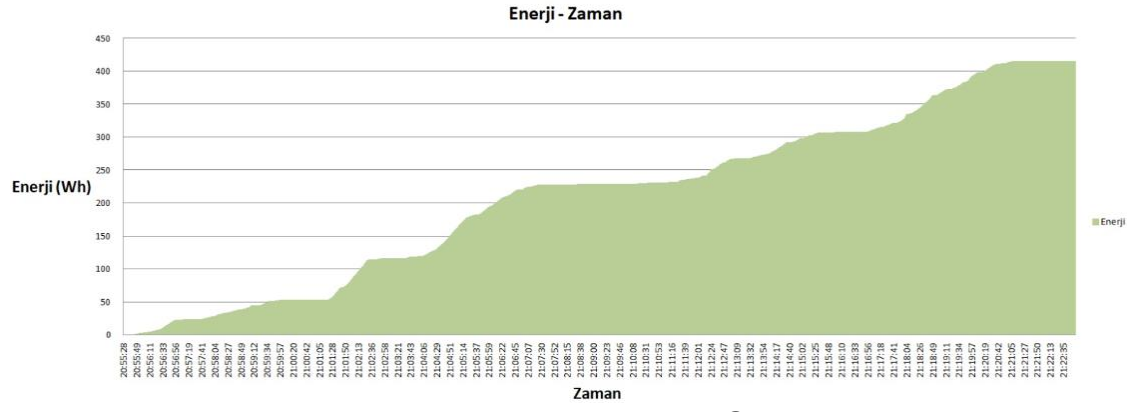


Figure 11.28. Energy-Time Graph

```

20:55:28
20:55:49
20:56:11
20:56:38
20:56:56
20:57:10
20:57:24
20:58:04
20:58:49
20:59:12
20:59:32
20:59:57
21:00:20
21:00:42
21:01:05
21:01:28
21:01:50
21:02:13
21:02:36
21:02:58
21:03:21
21:03:44
21:04:06
21:04:29
21:04:51
21:05:14
21:05:37
21:05:59
21:06:22
21:06:45
21:07:07
21:07:29
21:07:52
21:08:15
21:08:38
21:09:00
21:09:23
21:09:45
21:10:08
21:10:31
21:10:53
21:11:16
21:11:39
21:11:59
21:12:20
21:12:41
21:12:54
21:13:09
21:13:32
21:13:52
21:14:17
21:14:40
21:15:02
21:15:25
21:15:48
21:16:10
21:16:33
21:16:56
21:17:18
21:17:41
21:18:04
21:18:26
21:18:49
21:19:11
21:19:34
21:19:57
21:20:19
21:20:42
21:21:05
21:21:27
21:21:50
21:22:13
21:22:35

```

**Zaman**

Figure 11.29. Created .txt File

### 11.4.5. Isolated UART Communication

All cards in the vehicle control system also communicate with the PC with the CH340 USB to UART converter on them. ADUM1201 UART isolator IC is used to provide isolation between vehicle and PC. Isolated UART communication circuit is shown in figure 11.30. VCU main board, VCU I/O board and energy meter use the same UART communication circuit.

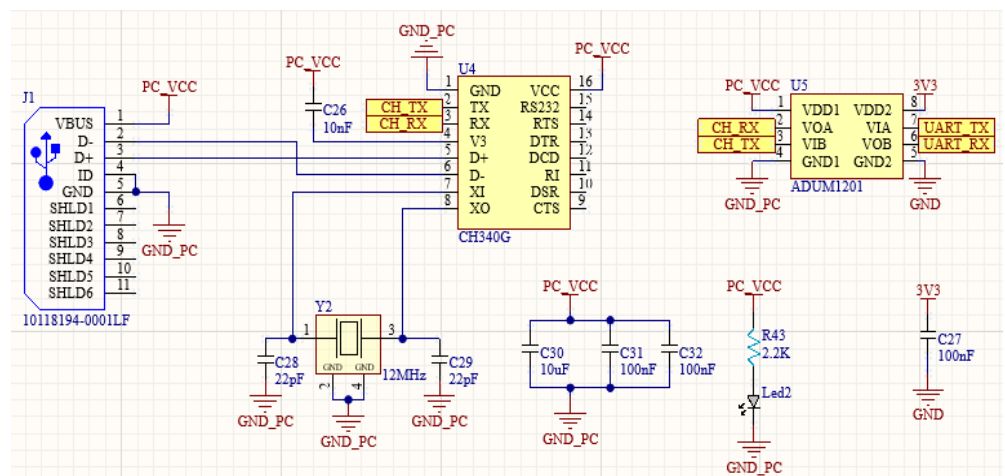


Figure 11.30. Isolated UART Communication

### 11.4.6. Regulators

To be used in the energy meter card, a 5 Volt output was obtained with the MP1482 buck converter from the 12 Volt input. The 5 Volt output from the MP1482 buck converter has been reduced to 3.3 volts with AMS1117-3.3 for the supply of the processor and other components. The mentioned regulator circuit schematic is shown in Figure 11.31.

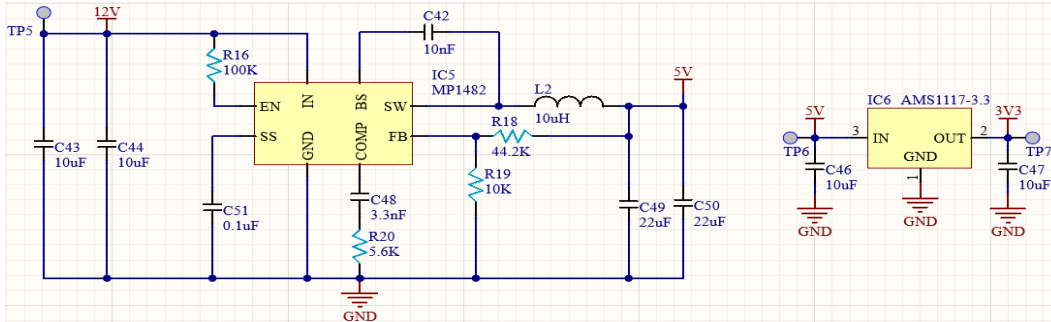


Figure 11.31. Regulator Circuit

### 11.4.7. Control Algorithm

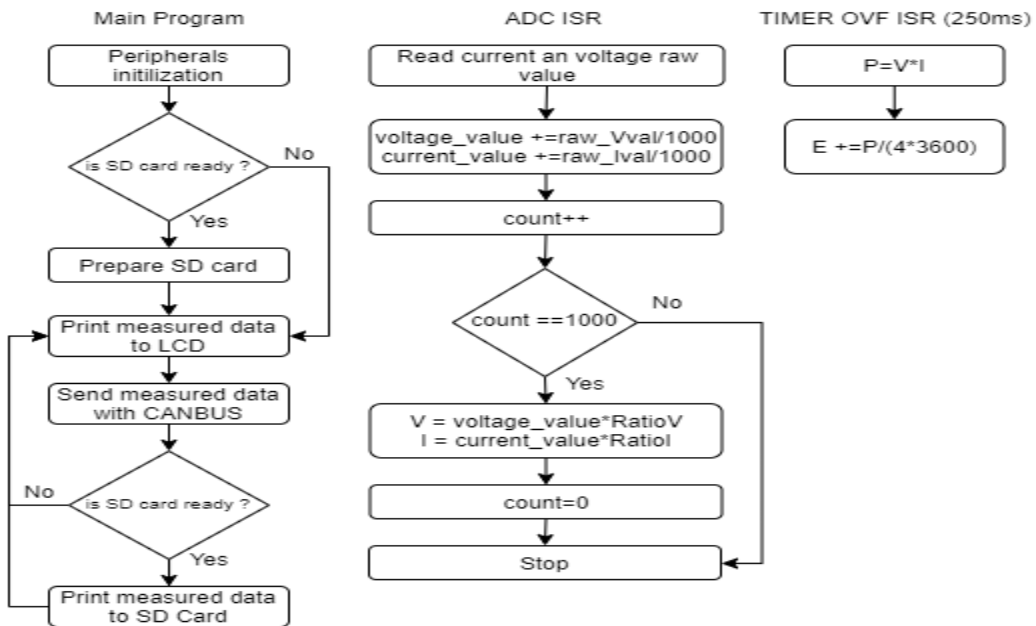


Figure 11.32. Energy Meter Control Algorithm

### 11.4.8. Production Studies

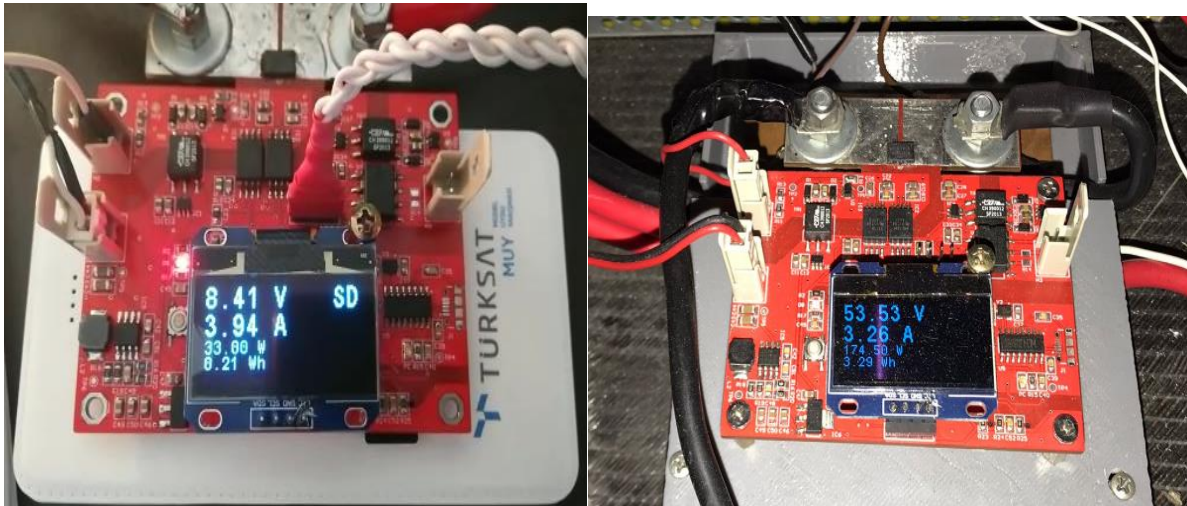


Figure 11.33. Energy Meter

<https://we.tl/t-94Zwbbs1mb>

	Previous Design	Current Design
<b>VCU Functions</b>	Telemetry ,I/O	Telemetry, I/O, Energy meter
<b>Controller IC</b>	Isolated I/O Card	Isolated I/O Card
<b>Number of VCU I/O</b>	15	16
<b>Electronic Circuit Design</b>	Altium Designer	Altium Designer
<b>Printed Circuit Design</b>	Altium Designer	Altium Designer
<b>Printed Circuit Manufacturing</b>	JLPCB	JLPCB
<b>Software Algorithm</b>	STM32CUBEIDE , C Language	STM32CUBEIDE , C Language
<b>Experimental Study</b>	-	-
<b>Size (PCB / Box)</b>	100 mm/85 mm	100 mm/90 mm

### 12. Insulation Monitoring Device

	Previous Design	Current Design
Micro Controller IC		
Measuring Method		
Sampling Period		
Measuring Accuracy at 100kΩ		
Measuring Accuracy at 1MΩ		
Size (PCB / Box)		

## 13. Steering System

The steering system is important for the vehicles to advance and turn smoothly. The angle created by the driver with the steering wheel is transmitted to the wheels through the system. This system basically consists of steering wheel, steering box, steering gear, tie rod and steering arm. It should be ensured that the steering system elements work in harmony with other elements in the front layout. Therefore, dimensions of the front parts of the vehicle (wishbone, axle carrier and chassis connection points) must be made. Later, the routing system can be designed.

One of the most important parts in the front geometry is angles. These angles are; caster, camber and king-pin angles. The camber and king-pin angles visible in the front view are shown in Figure 13.1. Generally, it can be seen differently at certain intervals in vehicles. The range values of the angles are taken from Prof. Dr. Nusret Sefa KURALAY's "Motorlu Taşıtlar" book.

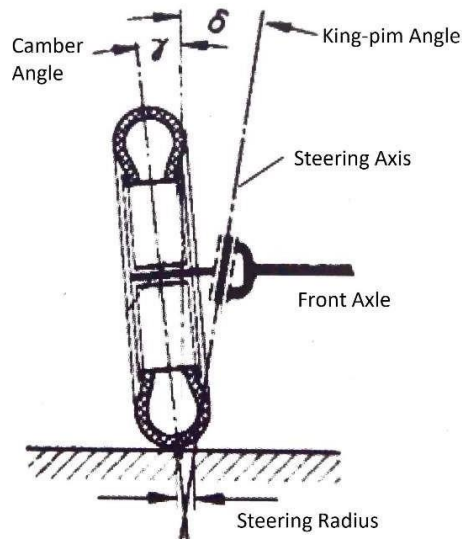


Figure 13.1. Camber, King-Pin Angles and Steering Radius.

### 13.1. Caster angle

It ensures the stability of the wheels. Creates torque of reversal on oriented wheels. It can be taken between  $0^{\circ}$ - $4^{\circ}$  in front-wheel drive vehicles and  $6^{\circ}$ - $12^{\circ}$  degrees in rear-wheel drive vehicles. In our vehicle, this angle is accepted as  $5^{\circ}$  in order not to reach the limit values.

### 13.2. Camber angle

Refers to the inclination of the wheels to the road. When viewed from above, the wheels are called positive if they are inclined outward and negative if they are inclined inwards. The slightly positive camber angle allows the wheels to roll better on roads with a tread slope. It usually ranges from  $3^{\circ}$  to  $1^{\circ}$  on the front wheels that are directed. This angle changes with the suspension movement. In our vehicle, it is accepted as  $0^{\circ}$  in normal conditions. With the suspension movement, this value ranges from about  $-1^{\circ}$  to  $+1^{\circ}$ .

### 13.3. King-pim angle

It is the angle that the steering axis makes on the ground in front view. This angle brings the wheel's ground contact point closer to the ground contact point of the steering axis. For this reason, the steering radius of the wheel becomes smaller. So it is easier to steer the wheel. This angle is usually between  $5^{\circ}$  and  $10^{\circ}$ . The existing wheels used in our vehicle have negative offset. The negative offset value in the rims increases the radius of steering on the wheels. In order to reduce this negative effect, the king-pin angle was determined to be approximately  $17^{\circ}$  in our vehicle.

2D drawing of the front layout was made by determining the angles. Figure 13.2 shows the drawing made in the SolidWorks program. In this way, it is aimed to determine the dimensions of the axle carrier and wishbone.

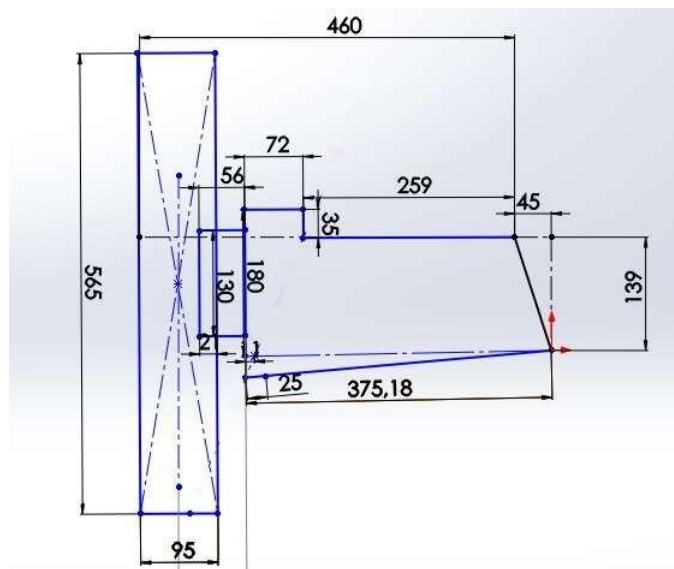


Figure 13.2. 2D Drawing of The Front Layout.

Wishbone and axle carrier prototype have been designed with the dimensions determined in 2D drawing. Front layout assembly was done in SolidWorks program. Changes were made to the wishbone and axle carrier dimensions to provide the previously determined camber angle. As seen in Figure 13.3, the camber angle remains between  $-1.15^{\circ}$  and  $+1.10^{\circ}$  with the suspension movement. If the vehicle floor is 150 mm above ground level, the camber angle is  $0.1^{\circ} \approx 0^{\circ}$ . Wishbone and axle carrier dimensions were determined in this way according to the targeted angles.



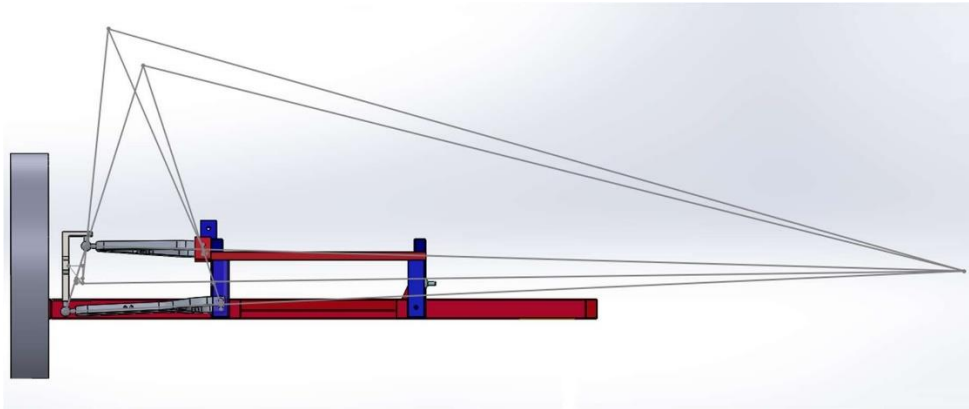


Figure 13.5. Determination of The T Point with The Graphical Method in Our Vehicle.

The model was created by adding steering arm, steering box and tie rod as a representative. The model is seen in Figure 13.6. In this model, the rotating angles on each wheel can be measured individually by moving the representative rack on the axis indicated by yellow.

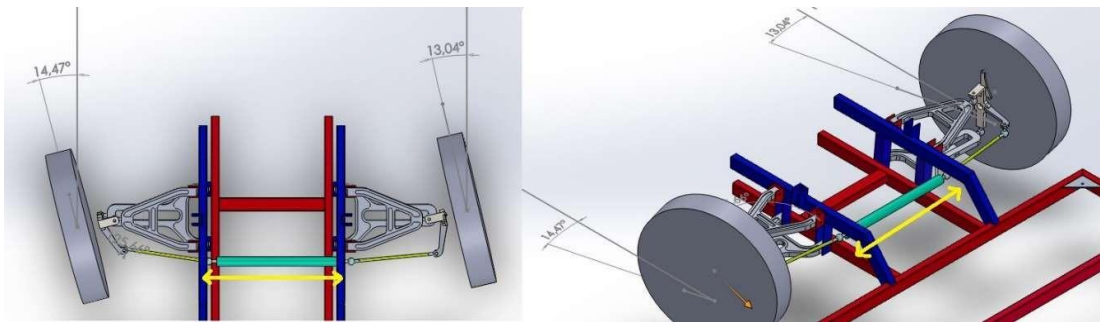


Figure 13.6. Modeling of Steering System

According to the Ackerman principle, internal and external wheels should make relative motion relative to each other. However, since we find the U point with pre-accepts, the Ackerman principle cannot be fully confirmed in these dimensions of the steering arm. Steering arm parameters are shown in Figure 13.7

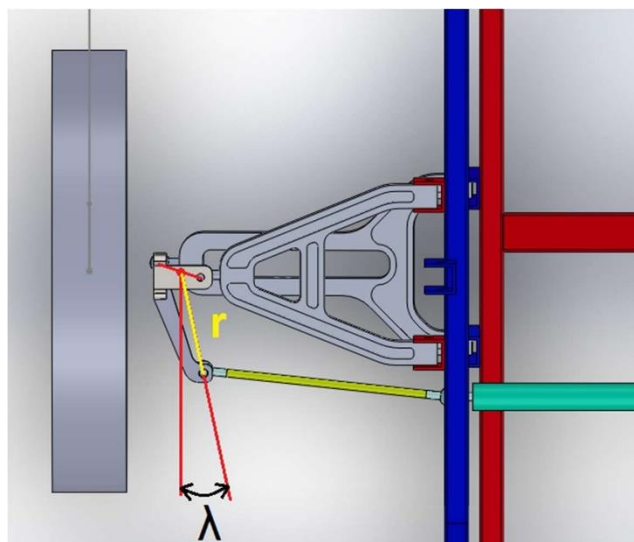


Figure 13.7. Steering arm parameters.

It is aimed to provide the Ackerman principle with different  $r$  and  $\lambda$  values. These values are shown in Table 13.1. The current turning angles of the wheels were obtained using the model in Figure 13.6 and theoretical values were obtained using the Ackerman formula. Ackerman formula;

$$\tan Bi = \frac{\frac{L}{j} \tan Ba}{\frac{L}{j} - \tan Ba} \quad (13.1)$$

$L$ : Distance between front and rear axles. ( $L=2003,4$  mm)

$J$ : Distance between left and right steering center. ( $j=1217,5$  mm)  $Bi$ : Internal wheel turning angles.

$Ba$ : External wheel turning angles.

$Ba_0$ : External wheel theoretic turning angle. (According to the Ackerman Principle)

Table 13.1. Turning angles for different steering arm parameters.

		$\lambda_1=8^\circ$		$\lambda_2=10^\circ$		$\lambda_3=12^\circ$		$\lambda_4=14^\circ$		
		$Bi$	$Ba_0$	$Ba$	$Ba-Ba_0$	$Ba$	$Ba-Ba_0$	$Ba$	$Ba-Ba_0$	
$r/j=0,10$	5	4,75	4,86	0,11	4,75	0,00	4,8	0,05	4,79	0,04
	10	9,05	9,6	0,55	9,36	0,31	9,36	0,31	9,29	0,24
	15	12,98	14,15	1,17	13,7	0,72	13,62	0,64	13,46	0,48
	20	16,60	18,48	1,88	17,74	1,14	17,54	0,94	17,27	0,67
	25	19,97	22,54	2,57	21,44	1,47	21,08	1,11	20,68	0,71
	30	23,14	26,27	3,13	24,74	1,60	24,21	1,07	23,63	0,49
	35	26,16	29,61	3,45	27,57	1,41	26,85	0,69	26,07	-0,09
$r/j=0,12$	5	4,75	5,29	0,54	5,3	0,55	4,52	-0,23		
	10	9,05	10,05	1,00	9,98	0,93	9,16	0,11		
	15	12,98	14,58	1,60	14,5	1,52	13,58	0,60		
	20	16,60	18,9	2,30	18,68	2,08	17,66	1,06		
	25	19,97	23,02	3,05	22,61	2,64	21,42	1,45		
	30	23,14	26,73	3,59	26,14	3,00	24,75	1,61		
	35	26,16	30	3,84	29,27	3,11	27,63	1,47		

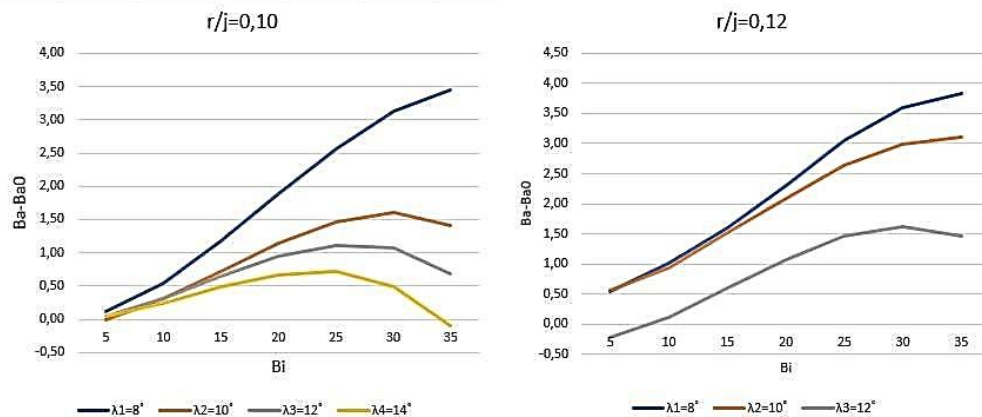


Figure 13.8.  $Ba-Ba_0$  graph.

According to the deviation of the internal wheel ( $Bi$ ), the theoretical angle ( $Ba_0$ ) and the current angle ( $Ba$ ) show the least deviation values for  $r/j = 10$  and  $\lambda=14^\circ$  (yellow curve).

Deviation from the theoretical angle value is maximum  $\approx 0.7^\circ$ . In this way, steering arm  $\lambda$  and  $r$  parameters are determined with minimum deviation. For  $\lambda = 15^\circ$ , it can be obtained that the maximum deviation is less, but  $B_a = 35^\circ$  deviation seems to increase.  $\lambda = 14^\circ$  is the ideal value for us, since it is

necessary to adhere more to theoretical values at low speeds. In Figure 13.9, Ackerman values and actual values of the vehicle are compared.

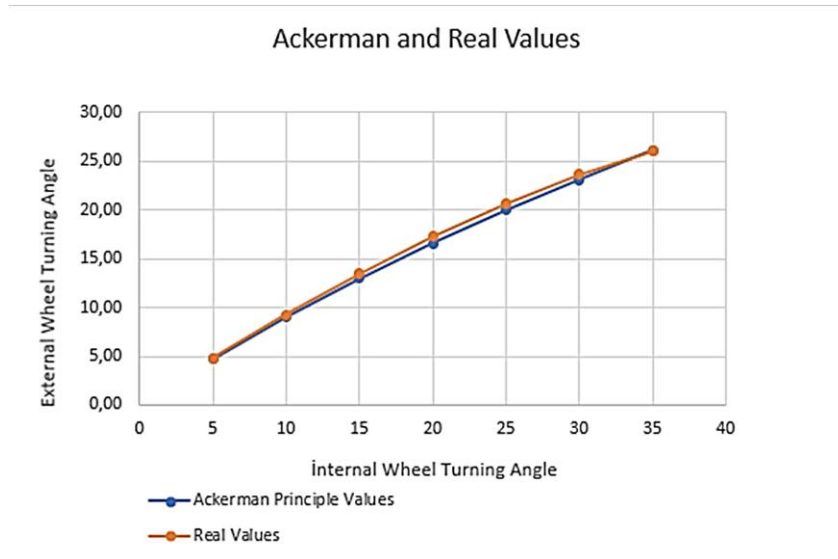


Figure 13.9. Ackerman and real values.

Thus, the dimensions of the parts in the steering system were determined. The turning radius of the vehicle was determined by adding new parts to the previously created model according to the determined dimensions. The turning radius is determined as 4.53 meter according to SAE standards (Figure 13.10). According to the bicycle model, the turning radius of the vehicle is shown in Figure 13.11.

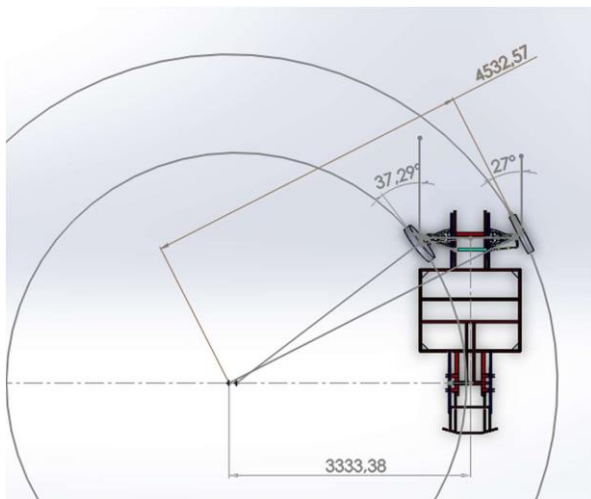


Figure 13.10. Turnin Radius of external and Wheel and rear axle.

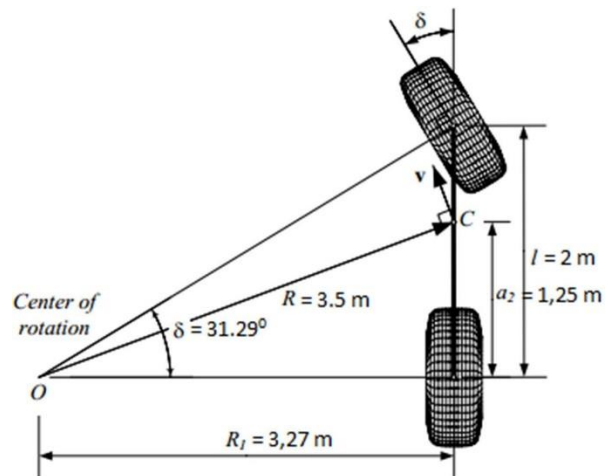


Figure 13.11. Turning radius according to the bicycle model.

The angle  $\alpha$  shown in Figure 13.12 should be between  $165^\circ < \alpha < 15^\circ$ . If the angle exceeds  $165^\circ$  when the inner wheel is at the maximum turning angle, the wheel may not be able to recover the old position. At these angles, the system starts to behave erratically. This angle in our vehicle reaches a maximum of  $156^\circ$  with the 63 mm movement of the rack.

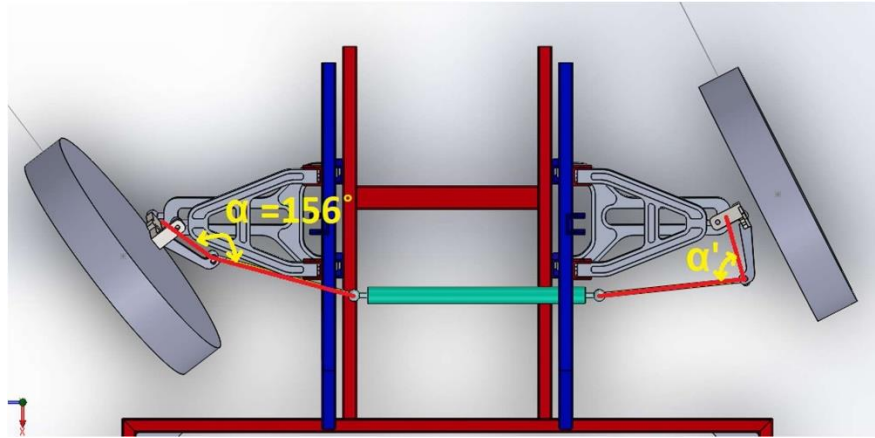


Figure 13.12. Maximum  $\alpha$  Angle.

A rack-type steering box was used in our vehicle. The pinion gear division diameter was determined according to the rack stroke value ( $\pm 63$  mm) determined above. Pinion gear diameter is 16.5 mm and module value is 1.5. The maximum dedendum tension calculated with the maximum torque value (12 Nm) that a person can apply to the steering wheel was found to be 290 MPa. 1040 steel was used in the rack and pinion, and surface hardening was applied to the pinion. The yield strength value of 1040 Steel is approximately 360 MPa. Steering box assembly drawing is shown in Figure 13.13.



Figure 13.13. Steering box assembly.

The body of the steering box was made of 6061 Aluminum. In order to make bedding of the rack easier, rack shaft was preferred. LME 20 UU Linear bearings were used while bearing the rack and 6903 Bearings were used while bearing the pinion. The section view of the steering box is shown in Figure 13.14.

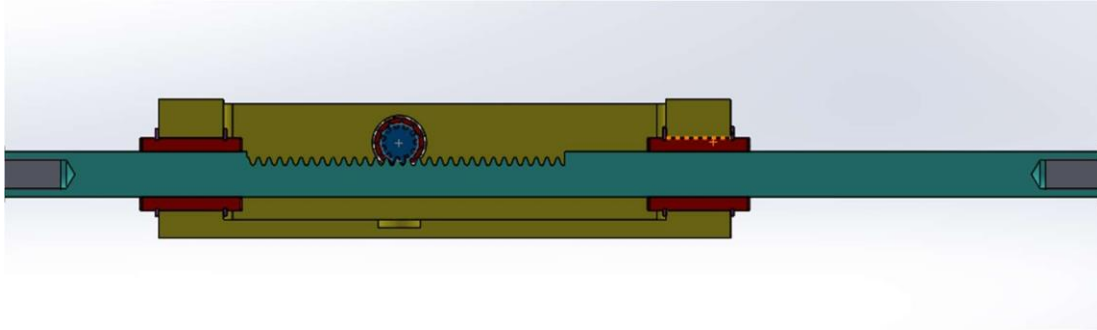


Figure 13.14. Steering box section.

According to the dimensions of the predetermined axle carriers and wishbone, their final designs for production were made and their static analysis were made. These designs are shown in Figure 13.15.

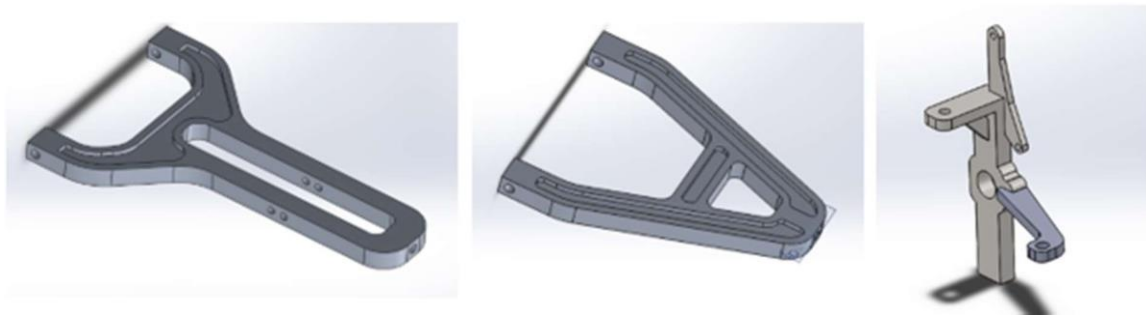


Figure 13.15. Lower- Upper wishbone and axle carrier.

The wishbones are made of aluminum casting. The parts were more than a process for improving the surface quality and opening the canals in the design. During static analysis of the wishbones, 5000 Newton forces were applied according to the critical condition calculated earlier. This critical situation is the fact that the vehicle passes fast through a bowl. Some analysis results are shown in Figure 13.16, Figure 13.17, Figure 13.18 and 13.19.

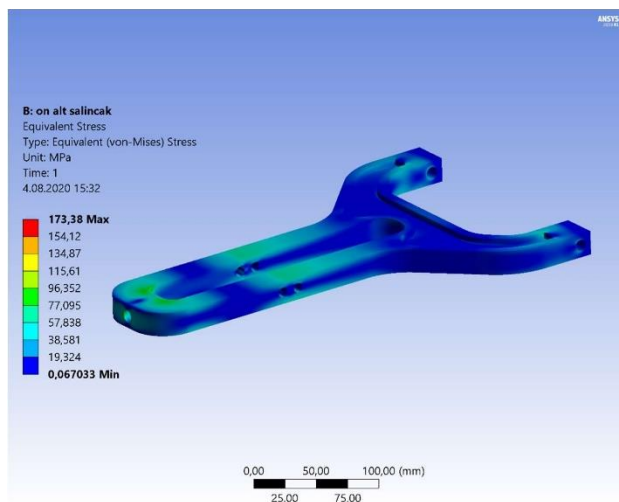


Figure 13.16. Equivalent (Von Mises) stress on lower wishbone

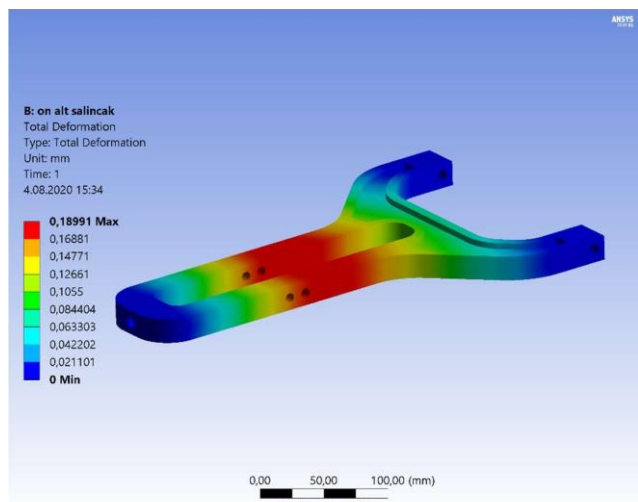


Figure 13.17. Total deformation on lower wishbone.

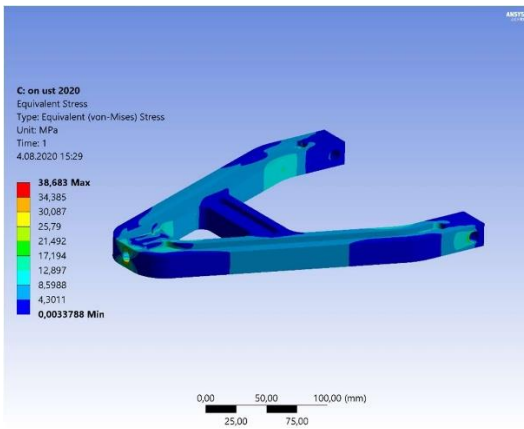


Figure 13.18. Equivalent (Von Mises) stress on upper wishbone.

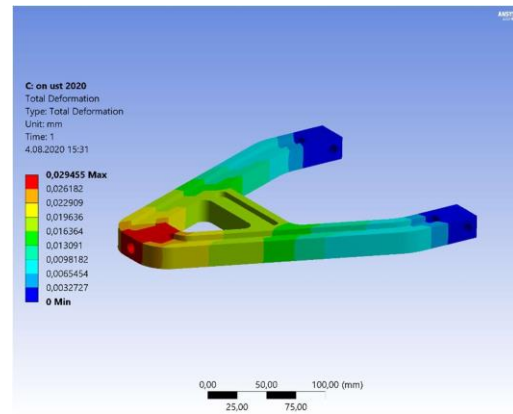


Figure 13.19. Total deformation on upper wishbone.

The axle carrier is made of steel material by laser cutting method. Here, the parts are combined with the latest welding for ease of production. Static analysis results of the axle carrier; maximum deformation is 0.18 mm and maximum von mises stress is 127 Mpa. In the middle part was supported, the upper connection point was pulled with 1500 N. Analysis results are shown in Figure 13.20.

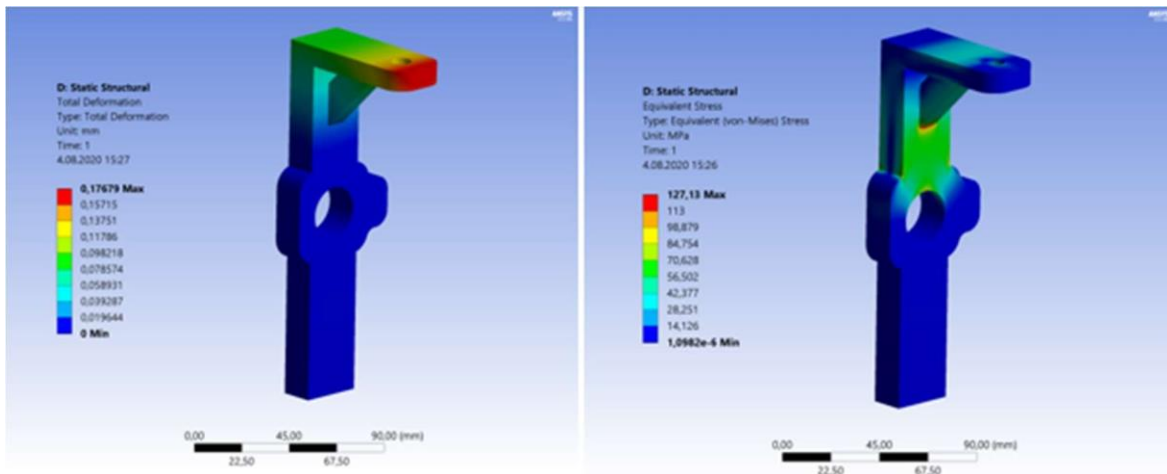


Figure 13.20. Equivalent stress and total deformation on axle carrier.

Thus, the design of all parts in the front layout and steering system has been completed. The final version of all parts is assembled in the SolidWorks program. Steering ratio and actual turning angles were measured with the values measured on this assembly. Figure 13.21 shows the assembly of the final parts.

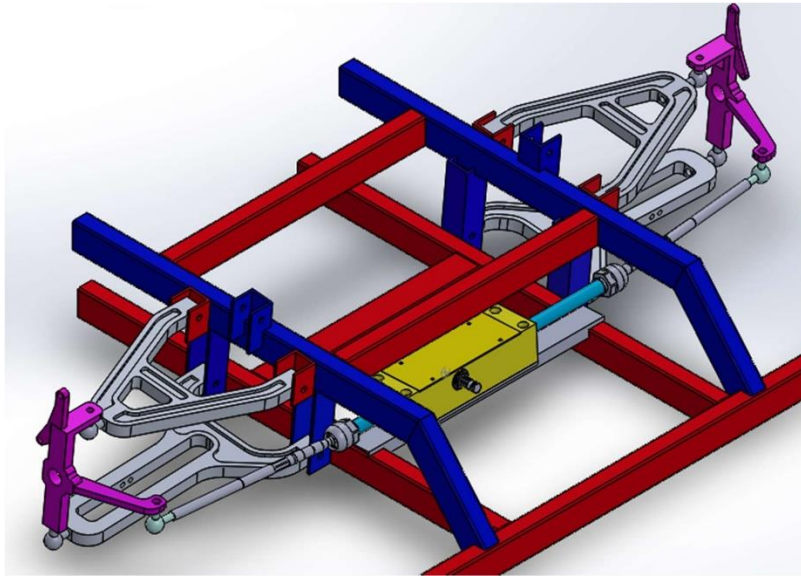


Figure 13.21. Front layout and steering system assembly.

Steering ratio in our vehicle was measured as 14.43. The total number of spins in the steering wheel is 2.43. In Figure 13.22, the turning angles of the right and left wheels are given according to the steering wheel turning angle.

The Turning Angle of the Wheels According to the Steering Angle

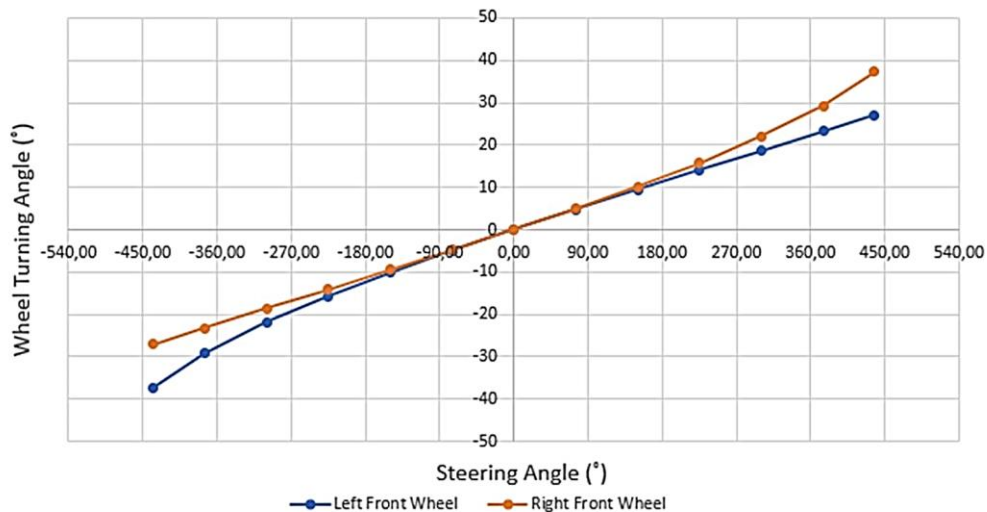


Figure 13.22. The turning angle of the wheels according to the steering angle.

Steering system data link: <https://we.tl/t-ZZXWFouzYI>

## 14. Door Mechanism

Firstly prioritizing design in the door mechanism, vertical wing door hinge to be done. But according to the competition rules, when the car overturned door could not open. At the same time analysis and our experience in the previous years shows that required hinge both heavy and it has connection problems. For this reason we turned another new design. When

determining hinge connection points the steepest surface deemed appropriate for the horizontal opening. When the determining hinge dimensions, FEA taken into account.

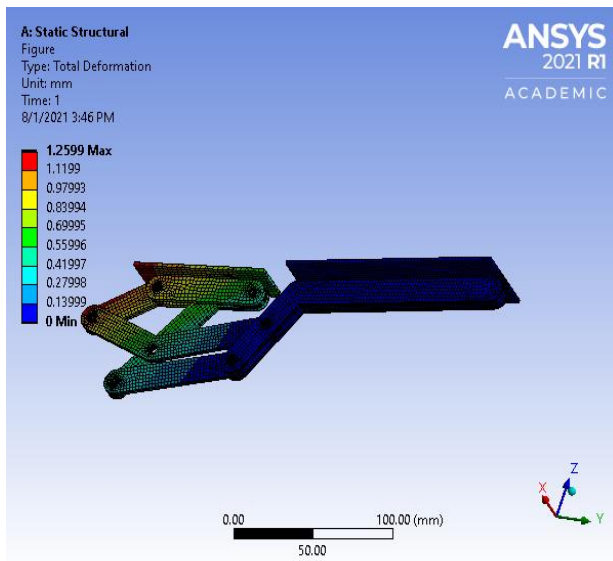


Figure 14.1. Total Deformation Analysis



Figure 14.2. Designed Hinge When Door Open

In the design process, when the door was opening seen door touching shell therefore designed additional connection points. Losening nuts problems solved at the connection point with lock nut and greasing the moving parts.

The car has two horizontal opening doors and their surface area more than 0.4 m<sup>2</sup> .For the sealing at the door used door weatherstrip. For locking mechanism used wardrobe lock and lock slot and used the circulation lock for the door to be pushed closed. 0.2 mm thick object can not enter into door because the door fits perfectly in the frame.

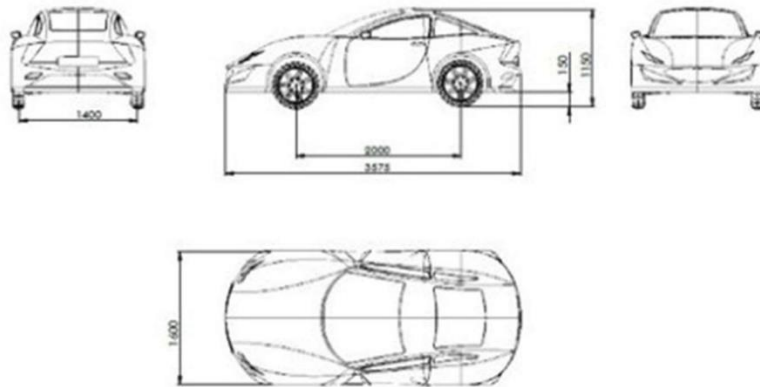


Figure 14.3. Door hinges and weaterstrips

<https://we.tl/t-3drccAPUd3>

## 15. Mechanical Details

### 15.1. Technical drawings



	Minimum (cm)	Value (cm)	Maximum (cm)
A	120	160	180
B	130	200	-
C	10	20	-
H	100	115	-
L	200	3575	425
W_front	100	140	-
W_rear	80	140	-

Figure 15.1. Technical drawing of the vehicle

### Strength analysis

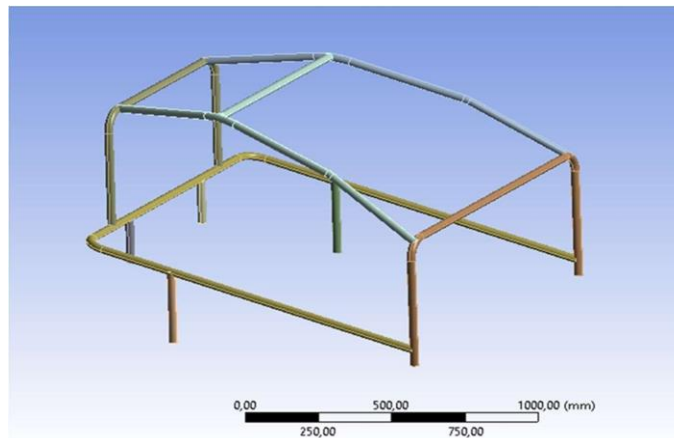


Figure 15.2. Designed rollbar with support

1000 N force was separately applied to front and rear rollbars to observe if the limit values of  $H/200$  for horizontal displacement were exceeded.

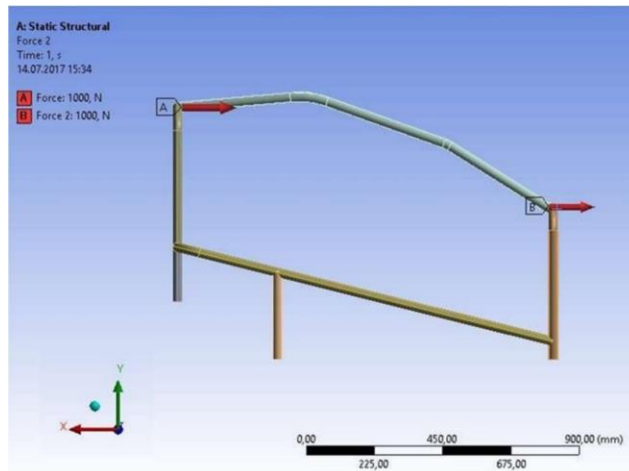


Figure 15.3. Directions of forces

The height of the rear rollbar was designed to be 650mm and the limit of the horizontal displacement is required to be  $H_{rear}/200 = 3,25\text{mm}$ . The height of the front rollbar is 500 mm and the limit of the horizontal displacement is required to be  $H_{front}/200 = 2,5\text{mm}$ .

Limit value of the front rollbar: 2,5mm Limit value of the rear rollbar: 3,25mm

As a result of the analysis made, the horizontal displacements were

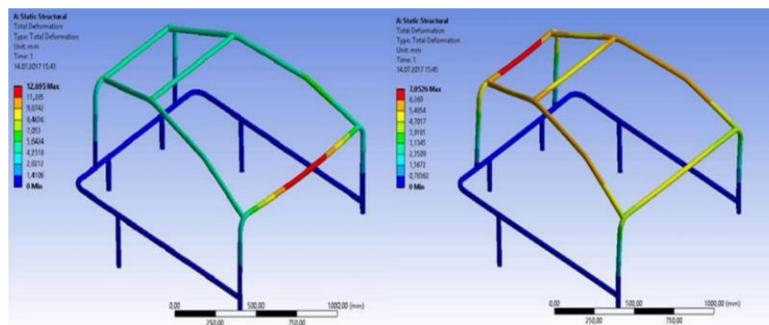


Figure 15.4. Analysis results

Front rollbar: 12,7 mm Rear rollbar: 7,05 mm

Over these results, the number of reinforcements were decided to be increased.

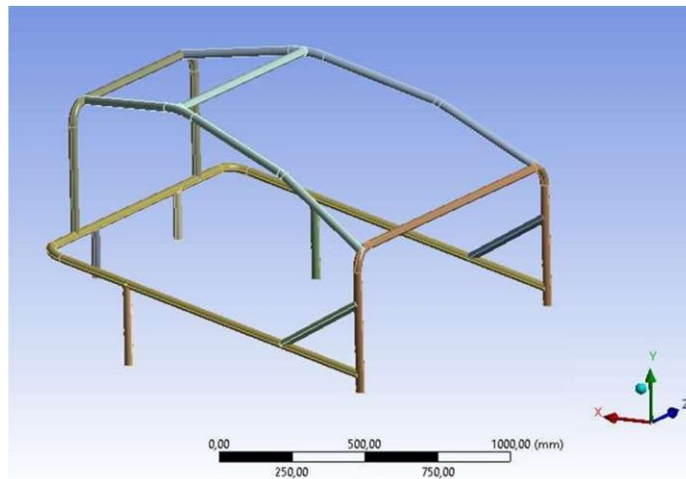


Figure 15.5. Adding new supports to rollbar

In the new reinforced state, as seen in the figure above, the horizontal displacements were found as following:

For front rollbar: 9,5mm For rear rollbar: 5,36mm

Since the intended values could not be found, a size increase to 40mm for diameter was carried out, with thickness remaining the same. The new analyses performed bore the following results:

Front rollbar: 3,85mm Rear rollbar: 2,27mm

Cross-sectional area: 1394,87 mm<sup>2</sup>

In another trial, sizes were changed to be 30 mm diameter and 5mm thickness and analysed this way with the following results:

Front rollbar: 6,85mm Rear rollbar: 3,80mm

Cross-sectional area: 1570,8 mm<sup>2</sup>

It is observed that the profile with a smaller diameter has a larger cross-sectional area. From this point, it is also determined that increasing diameter instead of thickness would provide more resistant structures. Since weight is an important criterion for the contest, profile sizes were returned to their initial values of 30 mm diameter and 3 mm thickness, and the number of reinforcements were decided to be increased instead.

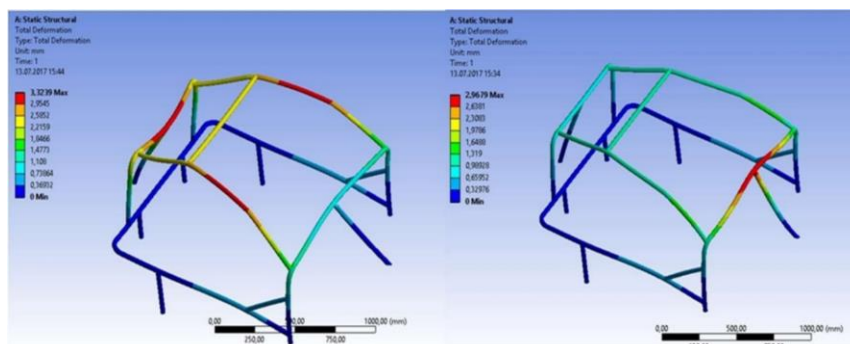


Figure 15.6. Analysis results of new supports added

With the reinforcents placed in the middle, the new values of Front Rollbar: 2,96mm

Rear Rollbar: 3,32mm were found; however, they weren't sufficient for the required limit values as well.

For this reason, the reinforcements removed from the middle were reorganized to be dual, as seen in the figure below.

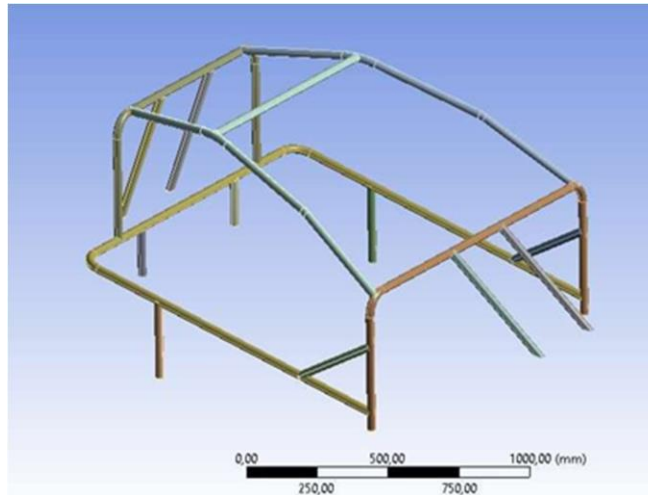


Figure 15.7. Rollbar design with extra support

As a result of the analyses made, the values of

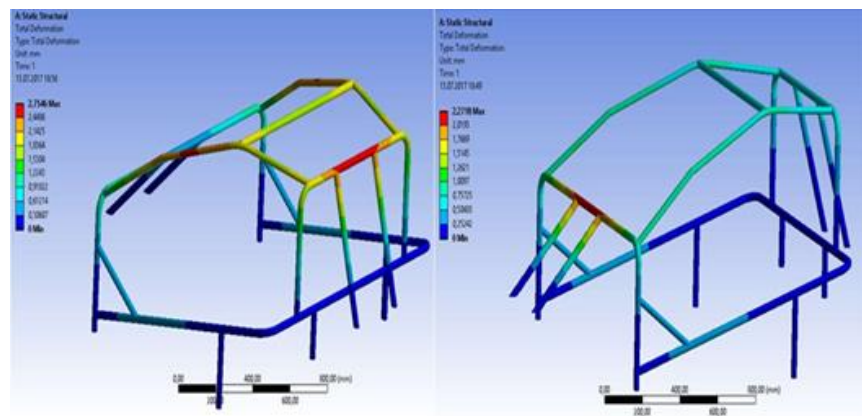


Figure 15.8. Results of rollbar analysis with added support

Front Rollbar: 2,27mm

Rear Rollbar: 2,75mm were found, which were below the limit values of  $H/200$ .

Although currently the analyses indicate that a reliable rollbar rollcage was formed, the structure is not stable when it is thought individually. For this, one final tweak was decided to be performed in order to prevent the new reinforcements from being damaged while they were separated from the chasis and causing any repairs by breaking during transportation.

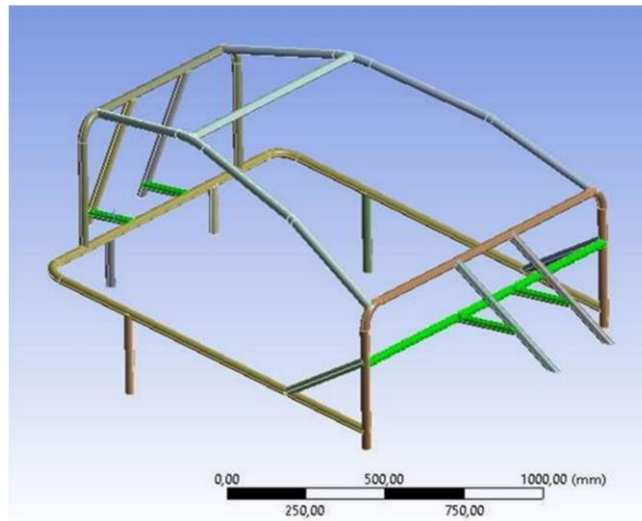


Figure 15.9. Final rollbar design

The new reinforcements were indicated in the figure above with green color. One final test was applied upon the final design in order to observe the durability of the finalized rollbar rollage.

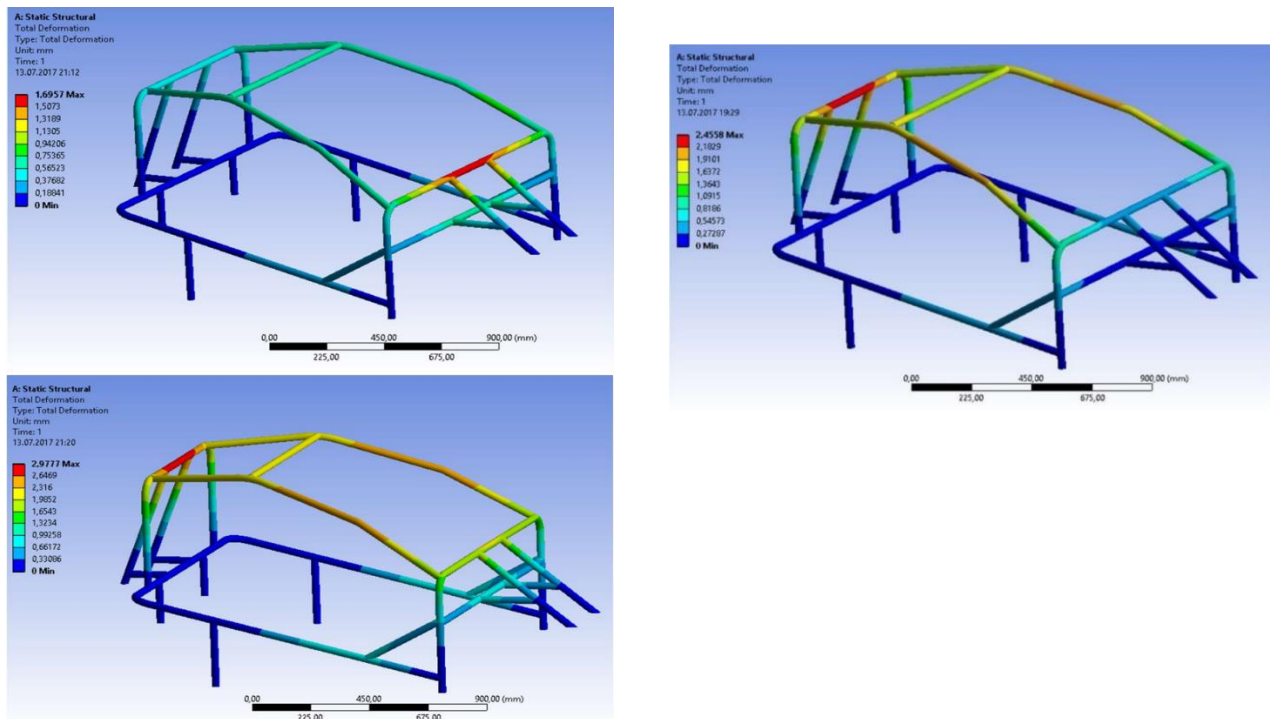


Figure 15.10. Analysis results of final rollbar design

Horizontal displacement of the front rollbar under 1000 N force: 1,69mm Horizontal displacement of the rear rollbar under 1000 N force: 2,45mm

Maximum horizontal displacements of both rollbars when they are under 1000 N force at the same time was found as 2,97mm for the rear rollbar and 2,45 for the front rollbar.

Postscript: Front Rollbar:  $500\text{mm}/200 = 2,5\text{mm}$  Rear Rollbar:  $650\text{mm}/200 = 3,25\text{mm}$

## 15.2. Outer shell production

Materials;

- Foam model
- BR 400 Polyester instead D2 Wood Glue
- Polyester Putty
- Poliya Polyester
- Mold release liquid
- Jel code
- Glass fiber
- Polyester

Car body material will be glass fiber. If financial support is provided, carbon fiber will be used.

For the body production, first the mold is produced with the help of model and then the actual body is produced with this mold.

The sequence of operations is as follows;

According to the body design, the minimum number of molds was determined so that the body can be removed from the mold as a single piece.

(The model to be produced is the male model, in which case the female mold will be removed)

After the number of molds is determined, the molds are ready to be machined in CNC (7 molds intotal including right and left door).



Figure 15.11. Styrofoam model of the vehicle

The mold was modeled by a firm that was a distributor, and the CNC was processed from the foam material.

The above-mentioned materials were supplied for body production.

The above steps have been performed and the next steps are as follows.

Steel paste will be used to provide the surface smoothness of the molds. Since the steel putty melts the foam a layer on the foam model with the aid of the BR400 polyester material, which does not melt the foam before the steel block, it will be created.

Since BR400 is not available in the hands of the supplier companies, the polyester alternative was tested with a few materials according to literature review.

These are D2 wood glue, white glue, Martin and ceiling paint as seen in the picture below. The cheapness and the desired due to the qualification of D2 wood was selected as a glutton.



Figure 15.12. Chemicals that will make the surface of the Styrofoam model suitable



Figure 15.13. Application of chemicals to Styrofoam surface and testing of reactions with polyester

After the dried D2 adhesive is completely dry, the steel paste is applied onto the polyester layer and dried, then emeryed to smoothness.

After all models are sanded and prepared, the mold removal process will start.



Figure 15.14. Corrections of mold surfaces

For surface polish, poly is applied with a sponge on a steel putty made of sandpaper.

The liquid separator material is applied to the surface with the help of a sponge so that the mold can easily be separated from the mold after polishing.

Jel code called material called plastic surface material is applied to the surface with the help of a brush.

(This material forms a layer between the mold and the mold. It allows the mold to be easily separated from the mold. It can be in different colors. The mold that will come out will be in this gel code color.)

After drying the gel code, the glass fiber is laid manually on the model surface and the polyester is applied with a brush. The process can be 2-3 times.

**11.** After this process, there is no oven, so it is kept in a hot environment for 24-48 hours. After drying, the molds are separated from the model.

After the molds have been removed, the molds are connected to each other at the junctions (female mold is formed)



Figure 15.15. Female mold formed by combining the molds

The same process as the removal process continues in the body.

After the polish lacquer cream and liquid separator liquid is dried and dried, the gel code is applied.

Fiberglass is applied into the mold by manual folding method 2-3 times with polyester.



Figure 15.16. Separation of the diffuser and the lower body from the mold

After the edge, the molds are separated one by one and the body is removed.

After the excess is cut off, it is sanded and painted.



Figure 15.17. Sanding the body and priming

### Experiments

A series of experiments have been carried out to determine factors such as freezing times and surface quality of the polyester types and the solids present at hand. The materials used during these experiments can be listed as follows.

2 different polyester 2 different freezers Catalyst substance Cobalt Octoate Butanol PVA fluid mold separator

The positive results of the butanol and PVA liquid mold release have been discovered in order to prevent the freezing of the brush used in future operations.



Figure 15.18. Testing polyester with different chemicals



Figure 15.19. Polyester reactions with different chemicals and determination of the duration of reactions

In order to preserve the appearance-wise aesthetics of the vehicle, the rollbars were decided to be in a way that they would contain the driver and the passengers. For their light-weight and easy accesibility, rollbars and rollcages were decided to be used from the profile that could show resistance above 200 MPa and is tempered aluminium pipe. The following design is the result of these decided criteria and the rules. The minimum values of 30 mm diameter and 3 mm thickness indicated in the rules were used as the profile size.

### Streamlined Designs

-Concept criteria for the vehicle:

-Vehicle will be a sport car

-It will not be far from reality as design

-A body for the vehicle was imagined which wasn't completely irrelevant from today's vehicle designs and was attractive for the customers.

According to the determined criteria, the outline of the vehicle was formed as the following figure and the appearance-wise aesthetics of the vehicle and it's theoretical yield was compared. In order to improve the results of this comparison, a pursuit for the maximum yield that could be obtained from vehicle had begun with revisions and alterations in the design.

The Star CCM + program will be used when CFD analysis of the vehicle is done and the k-epsilon turbulence model and segregated fluid temperature convergence will be made with Reynold-Averaged Navier-Stokes (RANS) viscous equations. Because the module uses the Boussinesq approach, it is likely to diverge from the correct result depending on the intensity variation at high speeds and in jamming environments. The equations used in the CFD analysis will be appropriate as the speed criterion of the vehicle is 60 km / h and the air temperature is 35 °C.

Rans equation:

$$\rho \left[ \frac{\partial}{\partial x} (\overline{u^2}) + \frac{\partial}{\partial y} (\overline{uv}) + \frac{\partial}{\partial z} (\overline{uw}) \right] = \frac{\partial \overline{p}}{\partial x} + \left[ \frac{\partial}{\partial x} \left( \mu \frac{\partial \overline{u}}{\partial x} - \rho \overline{u^2} \right) + \frac{\partial}{\partial y} \left( \mu \frac{\partial \overline{u}}{\partial y} - \rho \overline{u^r v^r} \right) + \frac{\partial}{\partial z} \left( \mu \frac{\partial \overline{u}}{\partial z} - \rho \overline{u^r w^r} \right) \right] \quad (15.1)$$

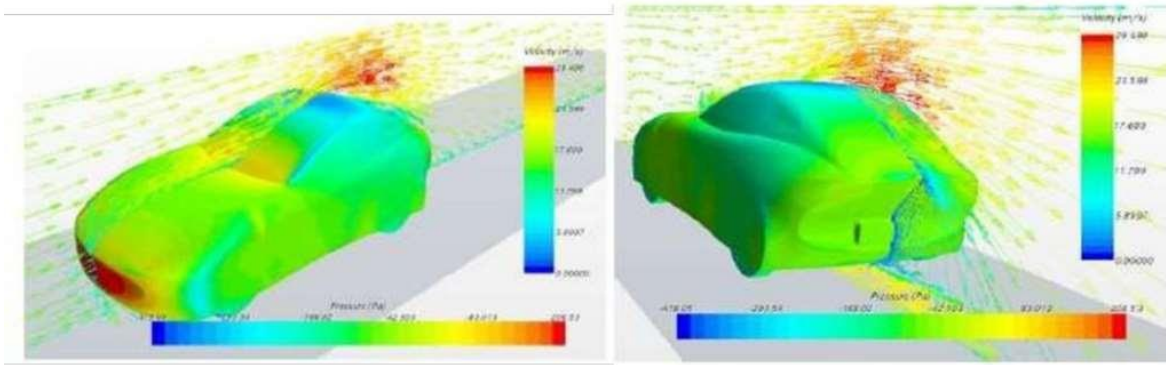


Figure 15.20. Pressure distribution on vehicle surface.



Figure 15.21. Iteration graph.

### First Revision

In the first design, a flow break was occurring at the rear of the vehicle. With this factor increasing with vehicle's speed, it had been causing too much power consumption combined with increasing drag force. With this tweak that is executed on the rear of the vehicle, which also preserved the fastback effect, it is observed that the drag force had been reduced by half. However, this move had an effect that enhanced the road grip and increased the weight of the vehicle. Since this was a modification to gain the maximum yield from the vehicle, and since the weight of the vehicle is an important aspect of yield from the vehicle, a second revision had been started.

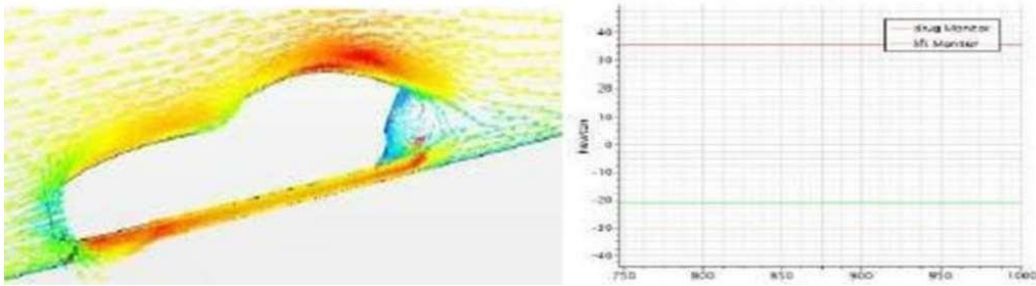


Figure 15.22. First revision results.

### Second Revision

After the rear of the vehicle was softened again, although better results were yielded compared to first analyses and the problem about the lifting force had been solved, it was observed that the drag force was higher than what it was in the first revision; which caused the third revision of the vehicle.

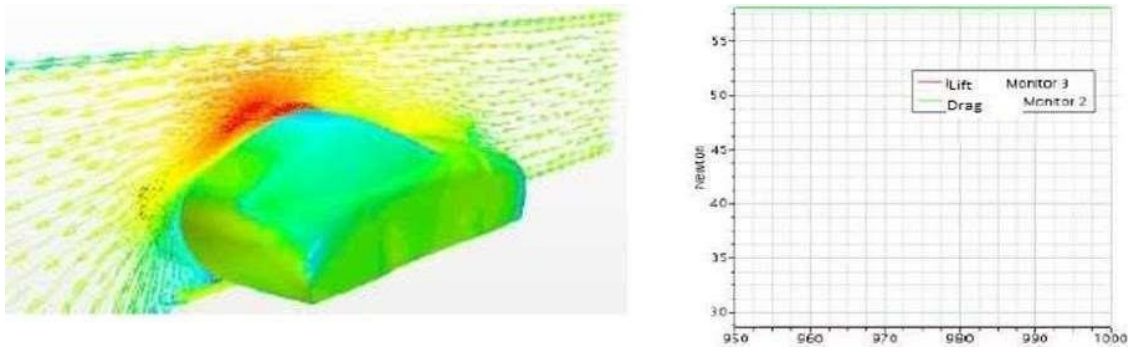


Figure 15.23. Second revision results.

### Third Revision

In the last revision, wind grooves were integrated to the front hood so that the wind coming from the front could be directed proportionally to the turbulence area behind the car; and thus it was planned that this method would clean the air there. Also, in order to decrease the Cd coefficient, the altitude of the body was decreased by 10 cm.

As a result, increase in drag force proportional to speed of the vehicle was decreased, and the vehicle was given a more stable geometry. With these changes providing both visual aesthetics and a stable vehicle geometry, it was decided to start production with this design.

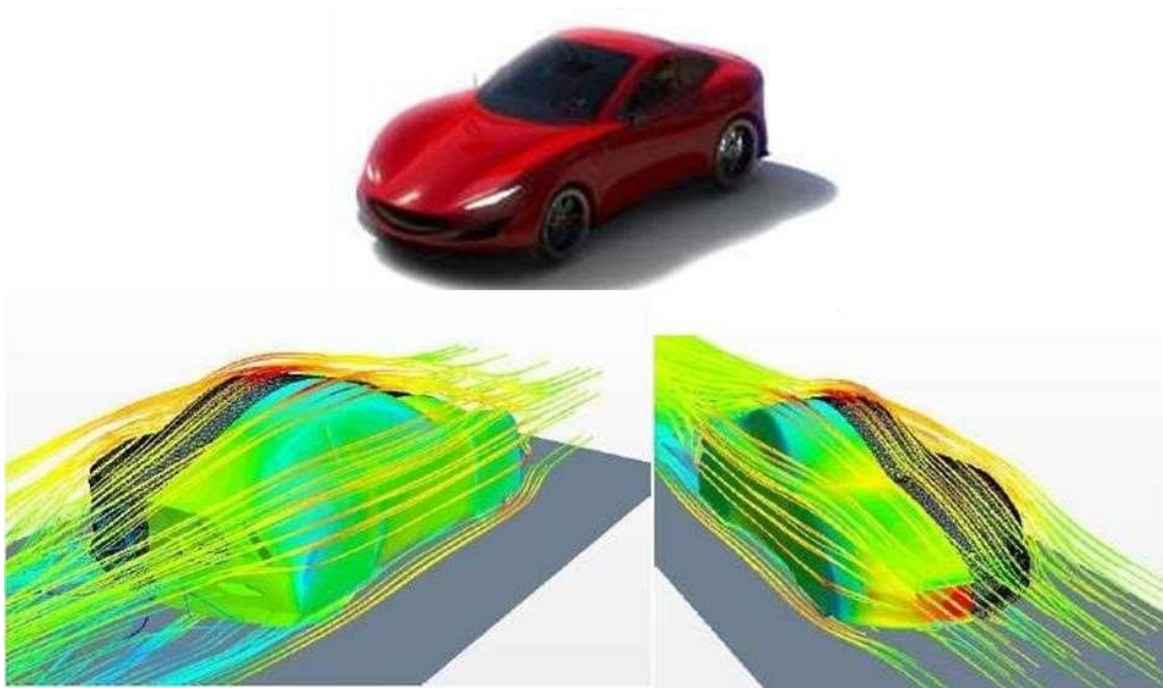


Figure 15.24. Final design and aerodynamic.

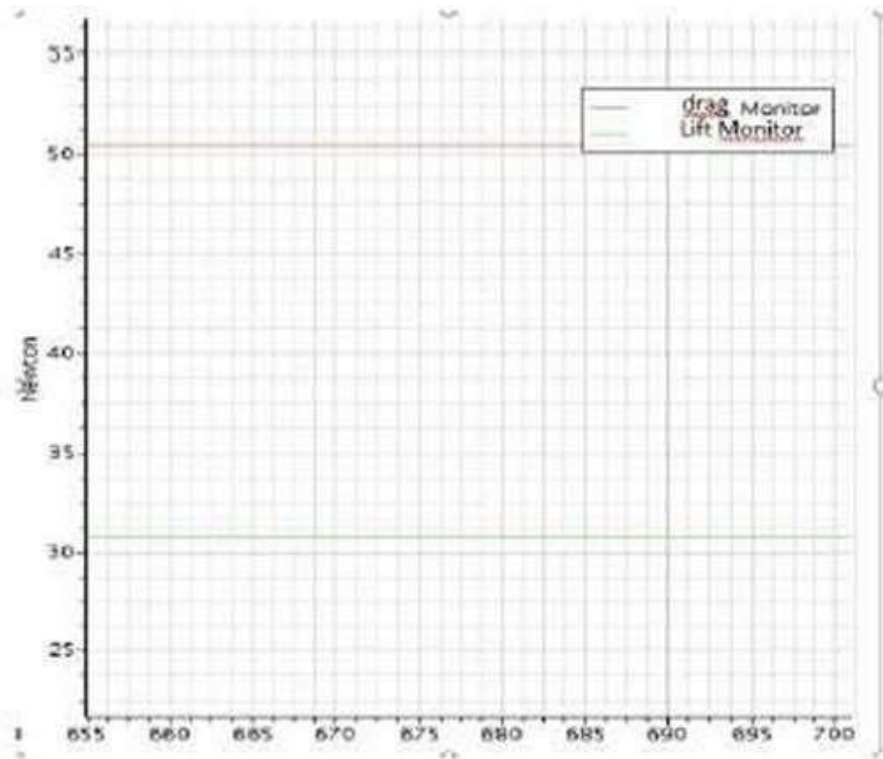


Figure 15.25. Iteration graph of last revision.

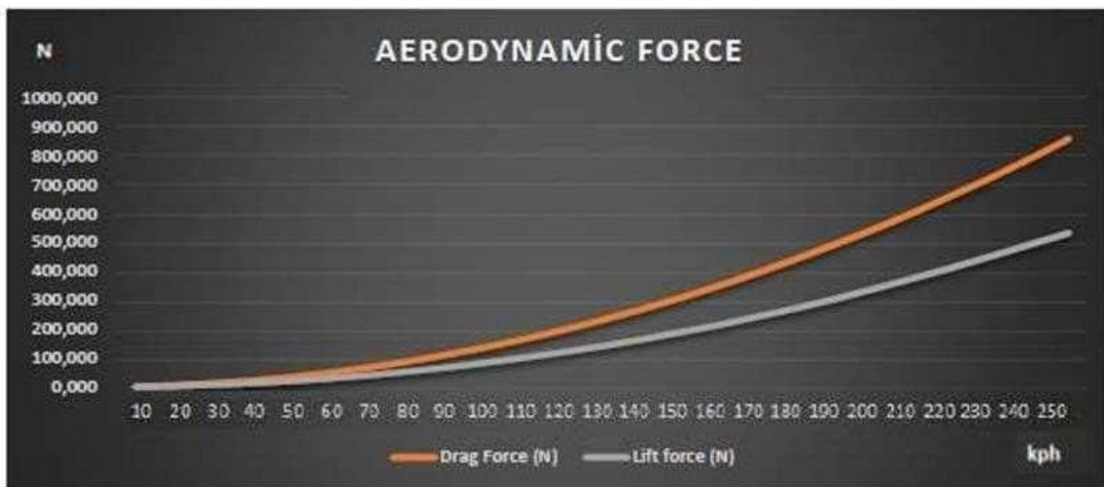


Figure 15.26. Change of forces with respect to speed.

While designing the surface of the vehicle, C3 surface continuity is tried to be used in b-spline curves and active curvature radius is tried to reach to the final result by making a contest with the radius of curvature.

$$\text{Curvature Radius: } R = \frac{\left[1 + \left(\frac{dy}{dx}\right)^2\right]^{\frac{3}{2}}}{\frac{d^2y}{dx^2}} \quad (15.2)$$

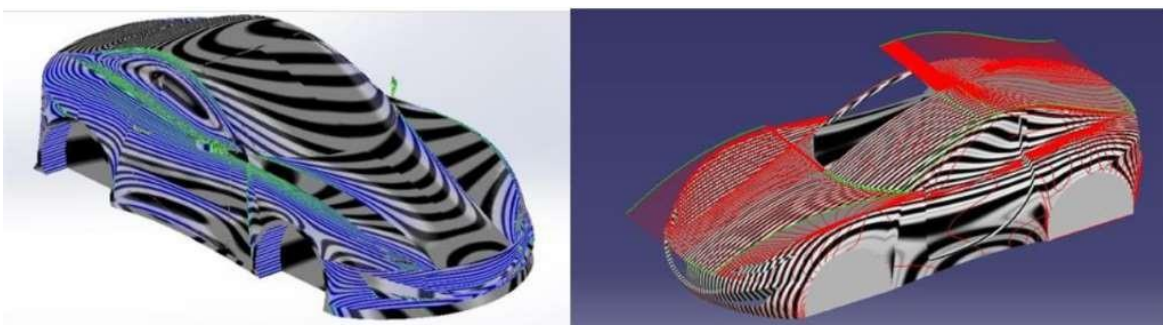


Figure 15.27. Zebra analysis of car body.

## Diffuser Design

Many factors influence the efficiency of automobiles. Some of those; engine, tire and rim construction, vehicle weight and aerodynamic structure. Of course, the most important place in the aerodynamic structure is the body geometry and the parts that are in contact with the air flowing outside the vehicle. Some work can be done to reduce these contacts. Today, almost all of the sports equipment manufactures the soles in flat or nearly flat form to reduce the air friction of the parts under the vehicle. Closure of these parts with planar parts provides a reduction in Cd of between 1% and 7%. [1] Based on these examples, the base design for the undercarriage was made.



Figure 15.28. Before and after the base design. Figures show the state of the vehicle before and after the base design.

By means of the base, the aerodynamic structure is improved and the basin diffuser insertion work is carried out. In this respect, various diffuser geometries are tried to be obtained by making use of

relevant and academic sources. Some of them are standard diffuser (without vertical guide) and advanced diffuser (with vertical guide). It is aimed to reach the result by evaluating the obtained bases with flow analysis.

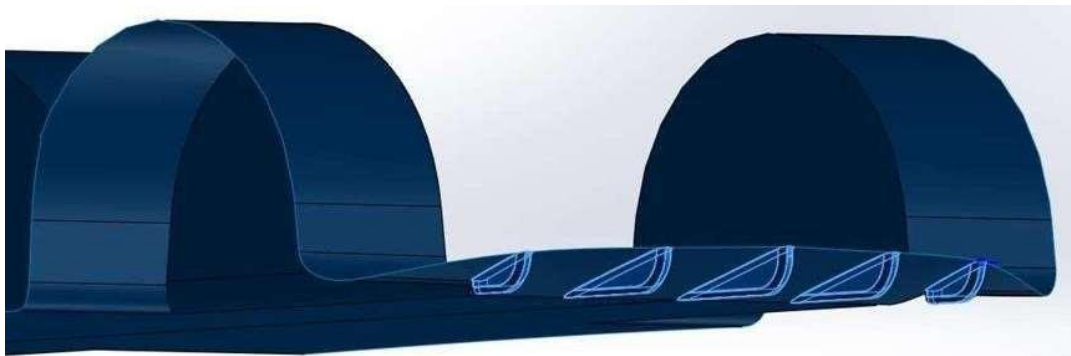


Figure 15.29. Advanced difusser (Vertical Guidance) model.

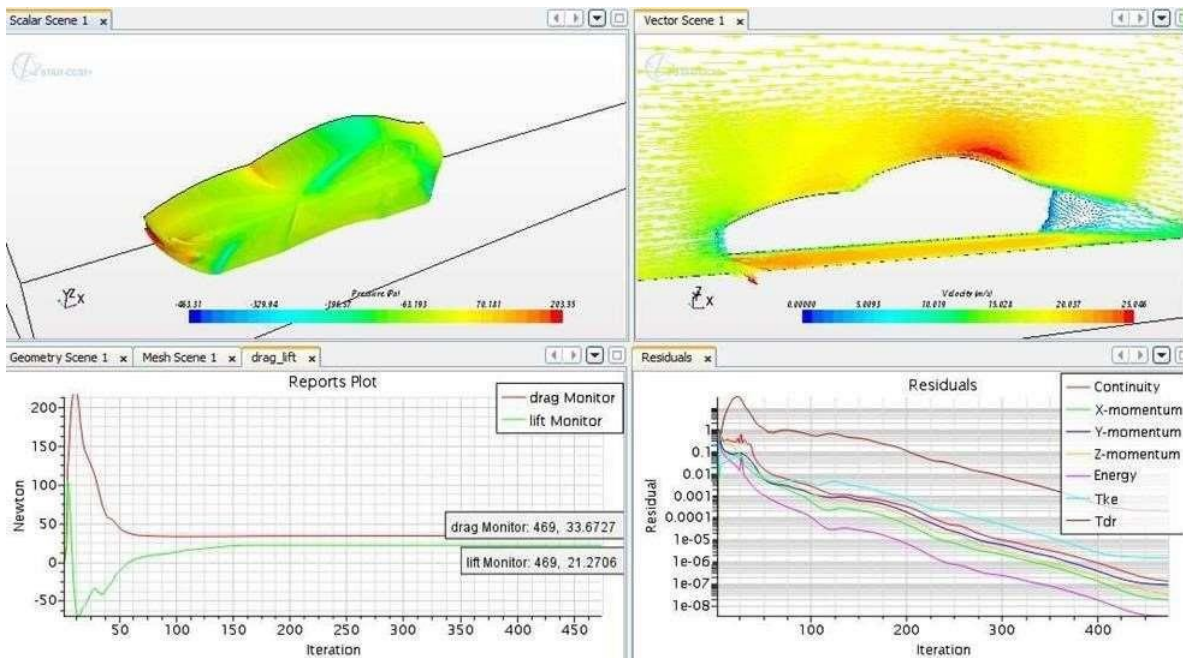


Figure 15.30. Analysis result of flat base.

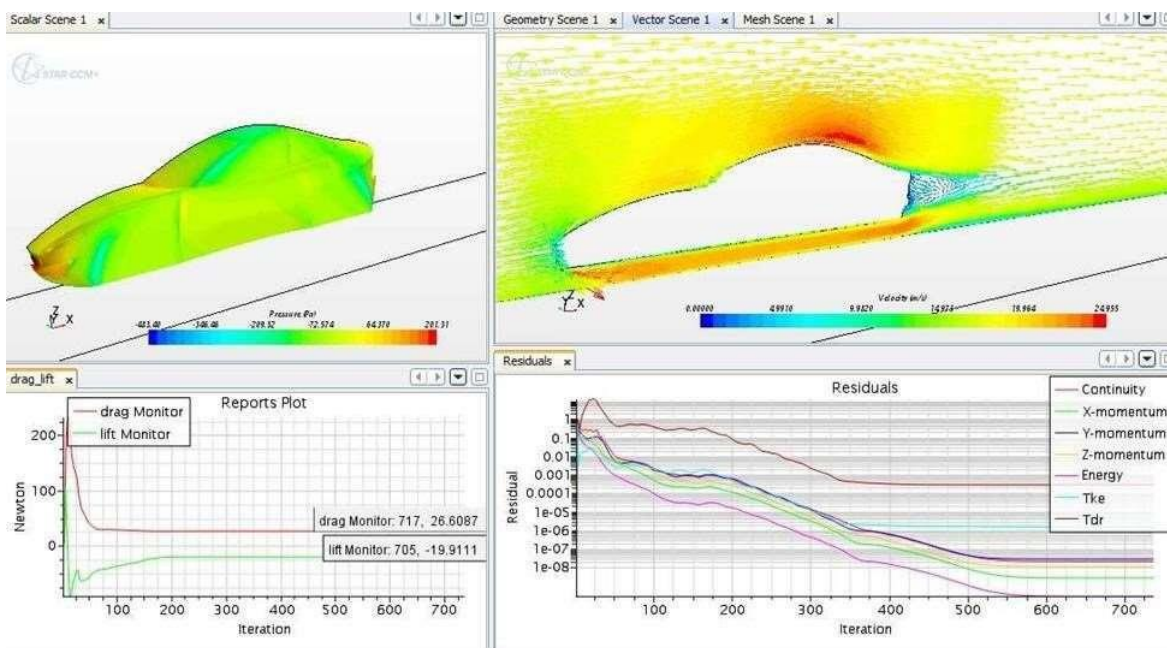


Figure 15.31. Analysis result of car body with difusser.

Table 15.1. Comparison of difusser design.

	Flat Base	Base With 15 Degree Difusser	15 Degree Advanced Difusser
<b>Drag Force</b>	33,6727N	26,4940N	26,6087N
<b>Lift Force</b>	21,2706N	-24,5986N	-19,9111N

Analyses made showed that the rear diffuser lower plate had a drop of 20% drag force compared to the posterior flat plate. In addition to this, the buoyancy force is positive and the negative is decreasing. A diffuser system was developed and a router was added. As a result of this change, the expected drift force could not be observed but the lifting force approached

to 0 and a positive result was encountered. The studies for reducing the drag force of the Rear Diffuser system are given below.

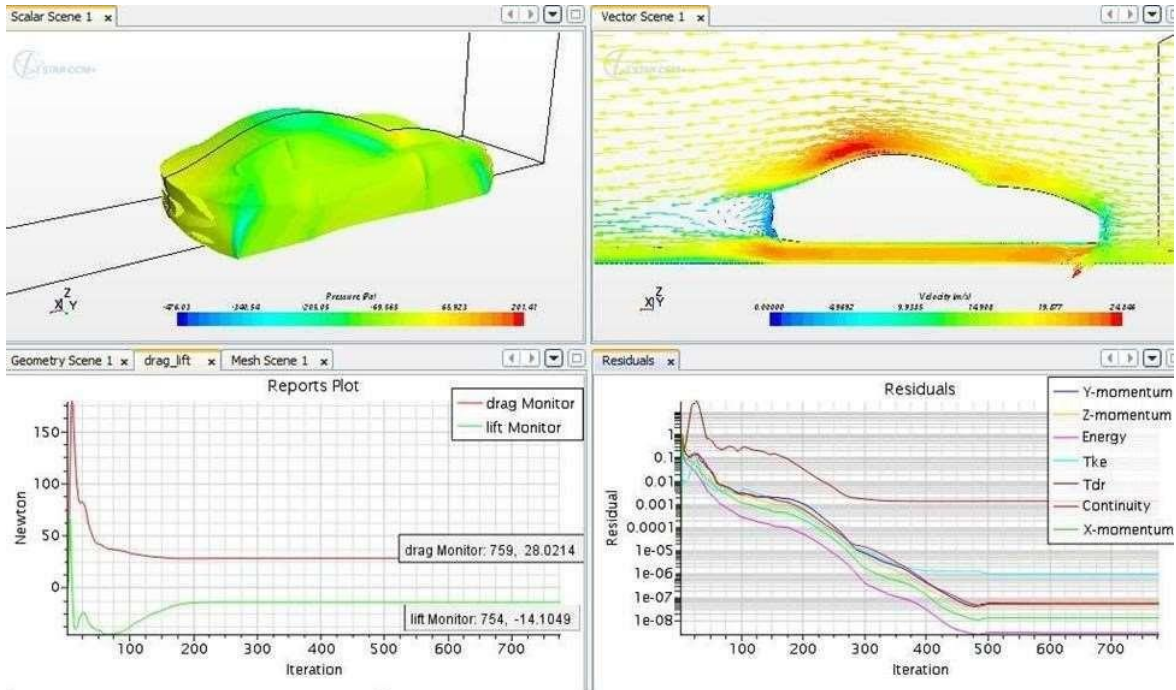


Figure 15.32. 10 Degree slope diffuser analysis results.

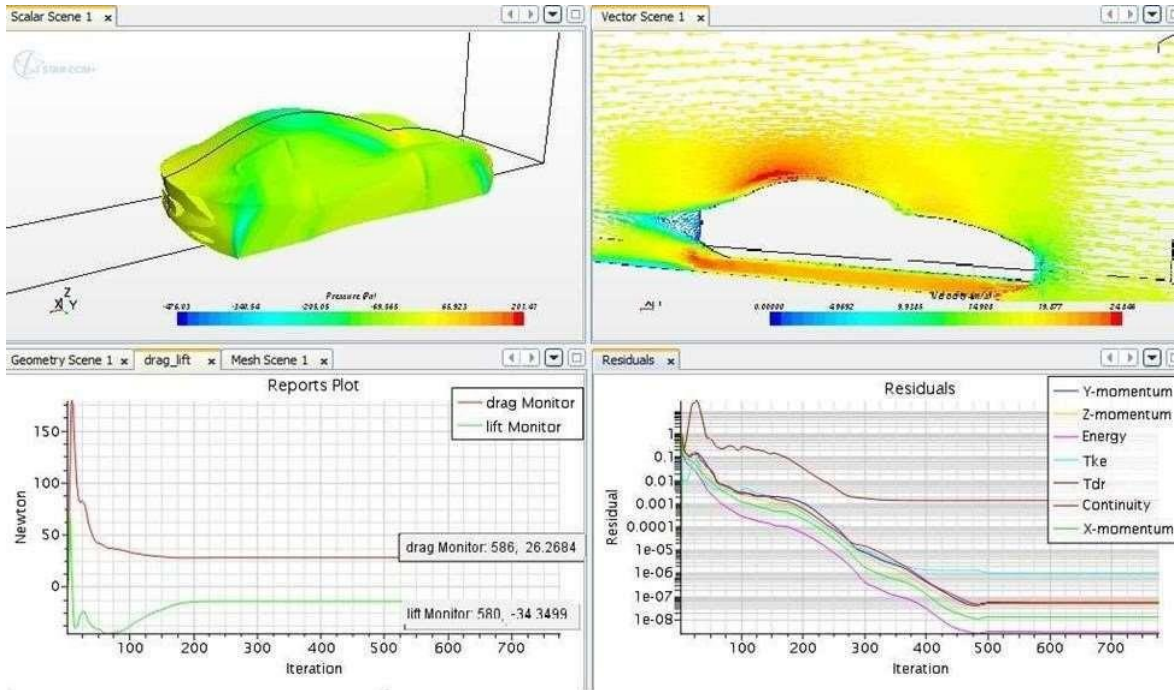


Figure 15.33. 20 Degree slope diffuser analysis results.

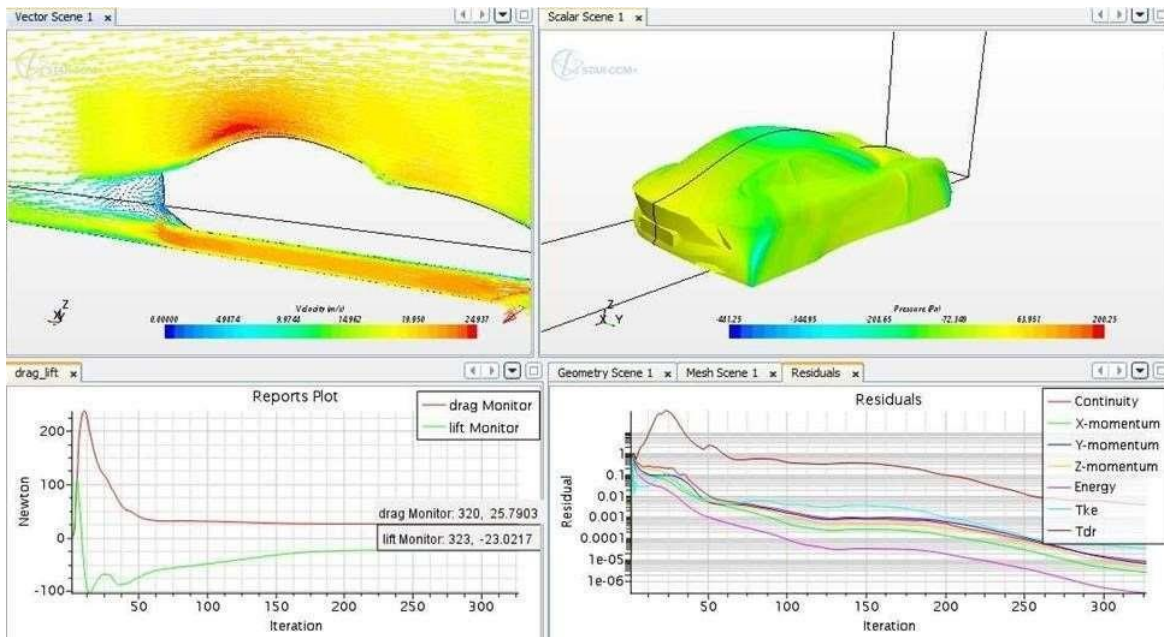


Figure 15.34. 30 Degree slope diffuser analysis results.

Table 15.2. Drag and lift forces according to different angles.

	<b>Drag Force</b>	<b>Lift Force</b>	<b>Drag Coefficient</b>
<b>10 Degree</b>	28,0214N	-14,1049N	0,117641
<b>15 Degree</b>	26,4940N	-24,5986N	0,111228
<b>20 Degree</b>	26,2685N	-34,3499N	0,110282
<b>30 Degree</b>	25,7903N	-23,0217N	0,108274
<b>Flat Ground</b>	33,6727N	21,2706N	0,141366
<b>15 Degree</b>	26,6087N	-19,9111N	0,11171
<b>Improved</b>			
<b>Diffuser</b>			

The analyzes were carried out at a speed of 60 km / h and the wheels were neglected due to the ease of analysis. When we interpreted the data, it seems that 30 degree inclination is more beneficial. However, it is accepted that the angle that can be applied in the vehicle body and depending on the position of the chassis is 15 degrees, and it is decided to use the vertically oriented developed diffuser from the lift force and appearance aesthetic. Below is a zebra pattern from the analysis of the surface continuity of the diffuser.

### 15.3. Chassis Design

With the profile form of the vehicle being square and rectangular, some hand-applied calculations were performed to determine thickness and, with these calculations being

crosschecked in motorering-based computer programs, the determined profile of 30×50×2mm was found to be resistant enough to use in design.

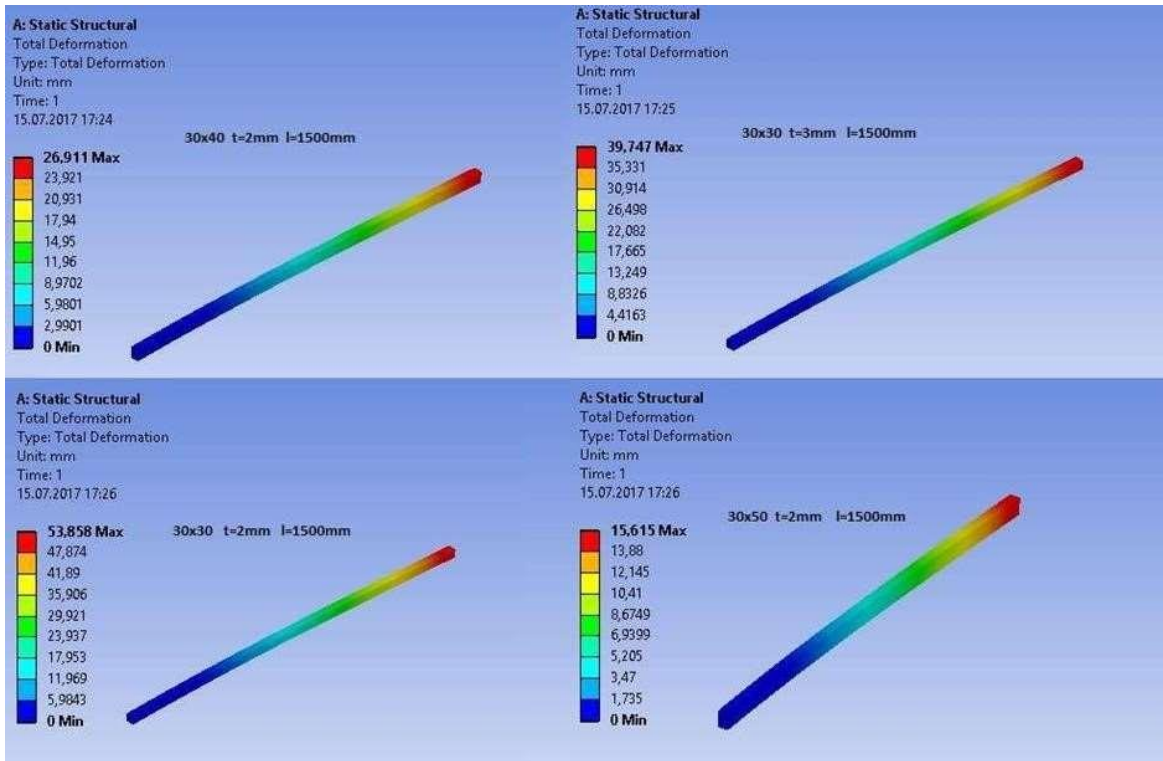


Figure 15.35. Strength analysis of profiles with different dimensions.

Calculations for resistance and weight were performed among 1500mm aluminum profiles, which was the peak height of the chassis. Comparisons that used 100 N forces on edges that are vertical, horizontal and double-edged were performed. Results of these comparisons are as follows:

Table 15.3. Comparisons of analysis results.

Box Section (mm)	Horizontal Deformation (mm)	Vertical Deformation (mm)	Dual Deformation (mm)	Horizontal Stress (MPa)	Vertical Stress (MPa)	Dual Stress (MPa)	Weight (kg)
30x30x2	-	53,858	76,168	-	77,727	152,89	0,93072
30x30x3	-	39,747	56,215	-	57,096	111,34	1,3462
30x40x2	42,52mm	26,911	50,315	62,724	51,702	113,31	1,0969
30x40x3	31,165mm	19,471	36,749	45,468	37,214	81,776	1,5955
30x50x2	35,137mm	15,615	38,446	54,547	38,39	92,264	1,2631

Chassis type has been chosen staircase chassis type because of the ease of production. The analysis, Design stages and improvements are given below.

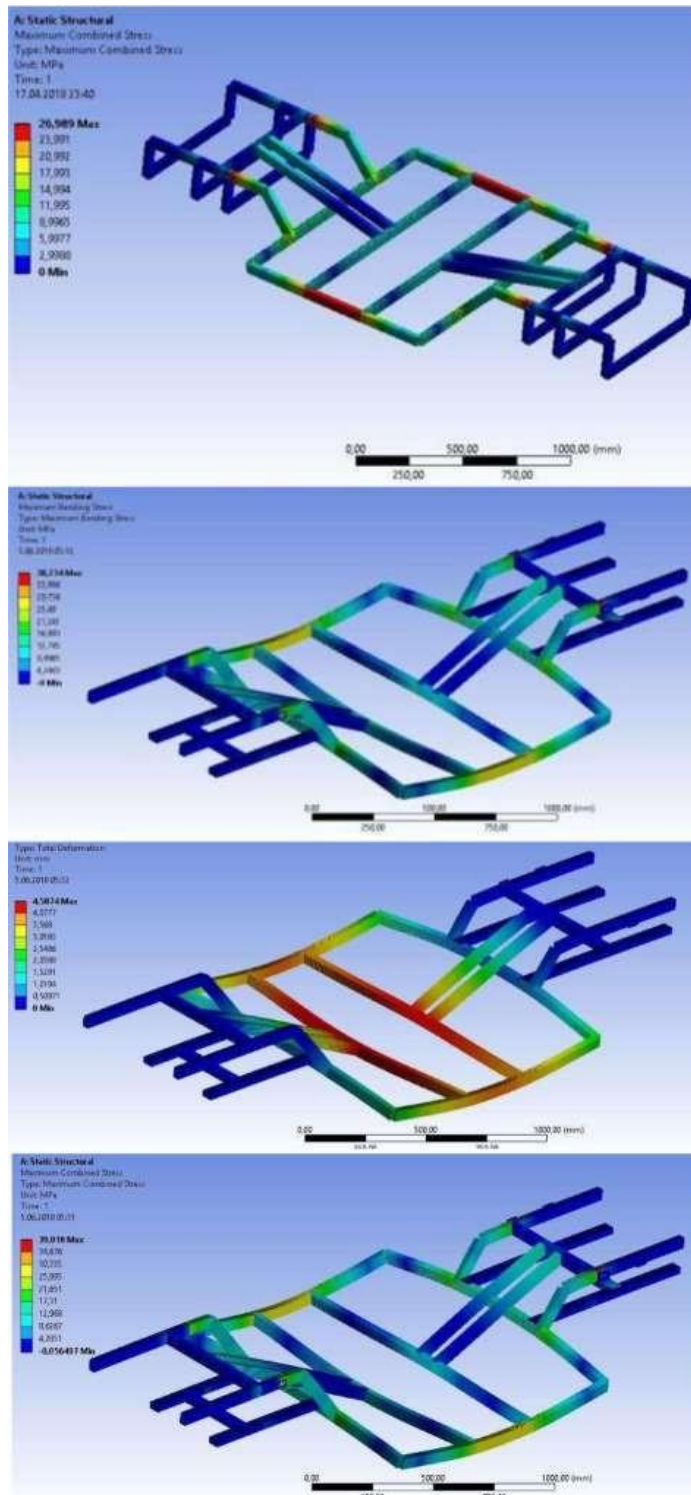


Figure 15.36. Analysis results of chassis.

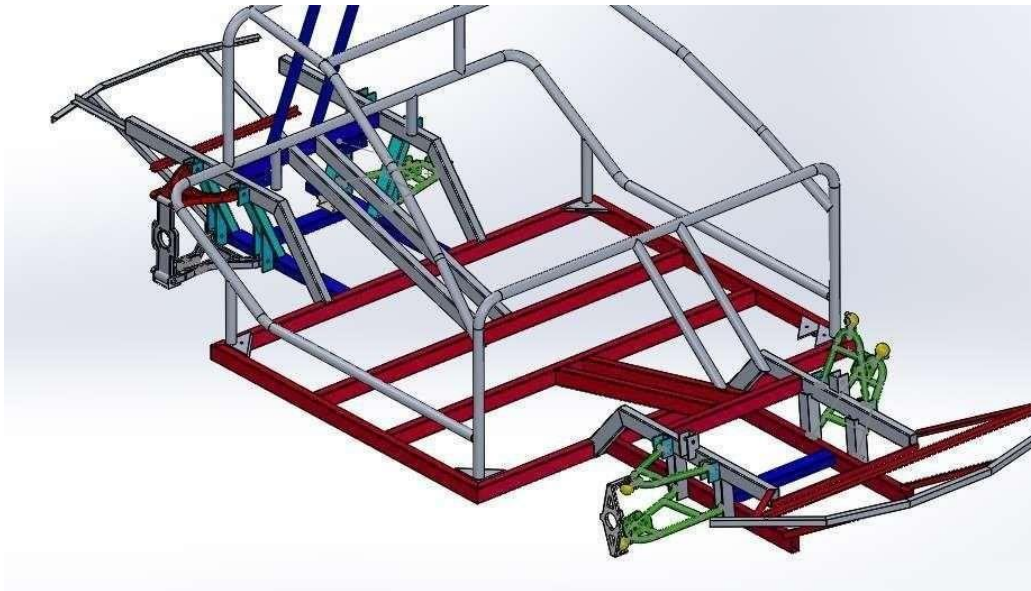


Figure 15.37. Final design of chassis.



Figure 15.38. Production phase.

### Headlamp Design

A more elegant appearance has been processed by using curved surfaces in the headlights. For this purpose, the way of forming a mold has been made. While creating the mold with expanded foam, the outer surfaces have been obtained in different ways in accordance with their geometry. We also decided to make the headlight frame carbon fiber to take advantage

of the ease of styling and lightness and other. The interior design of the headlights has also been redesigned in accordance with their geometry.

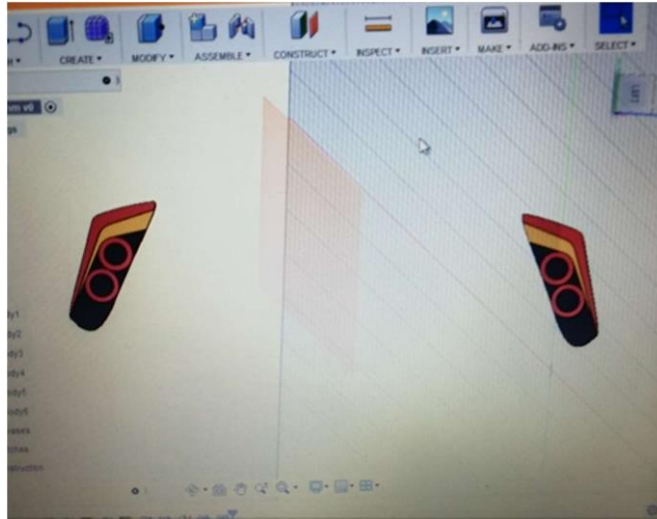


Figure 15.39. Led Design.



Figure 15.40. Molding Phase of Headlights.

$V=50\text{km/h}$   $m=250\text{kg}$

Drag Force= 35,209N Lift Force=21,434N Friction from the Ground=22,42N

**4000 meters Energy required to complete a straight road at 50 km/h**

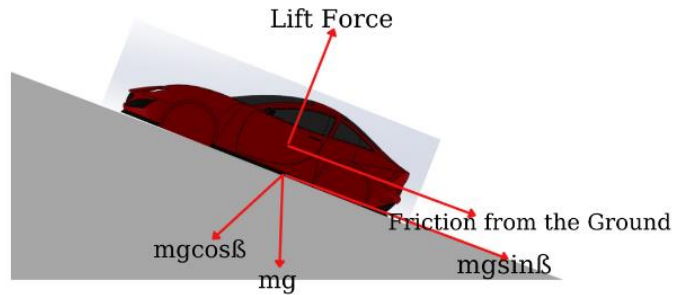
Friction from the Ground= $(g*(m-\text{Lift Force}))-0,01$

$F_{\text{net}} = \text{Drag Force} + \text{Friction}$

=57,629N

=57,629N\*4000m=230,516J

**Engine power required to reach 50km/h on a 6% slope**



$$F_{net} = ((m - \text{Lift Force}) * g) \sin \beta + \text{Friction} * \cos \beta + \text{Drag Force}$$

$$= 134,15 \text{ N} + 22,38 \text{ N} + 35,209 \text{ N}$$

$$= 191,74 \text{ N}$$

$$P = F * V$$

$$= 191,74 \text{ N} * 13,9 \text{ m/s}$$

$$= 2665,19 \text{ W}$$

**Max speed that can be climbed on 6% slope with 1.5kW motor**

$$P = F * V$$

$$F_{net} = 142,09 \text{ N} + 22,38 \text{ N} + 12,943 \text{ N}$$

$$= 177,41 \text{ N}$$

$$1500 \text{ W} = 177,41 \text{ N} * V$$

$$V = 8,45 \text{ m/s}$$

$$= 30,43 \text{ km/h}$$

30 km/h için;

$$F_{net} = 146,25 \text{ N} + 22,38 \text{ N} + 12,943 \text{ N}$$

$$= 181,58 \text{ N}$$

$$1500 = 181,58 * V$$

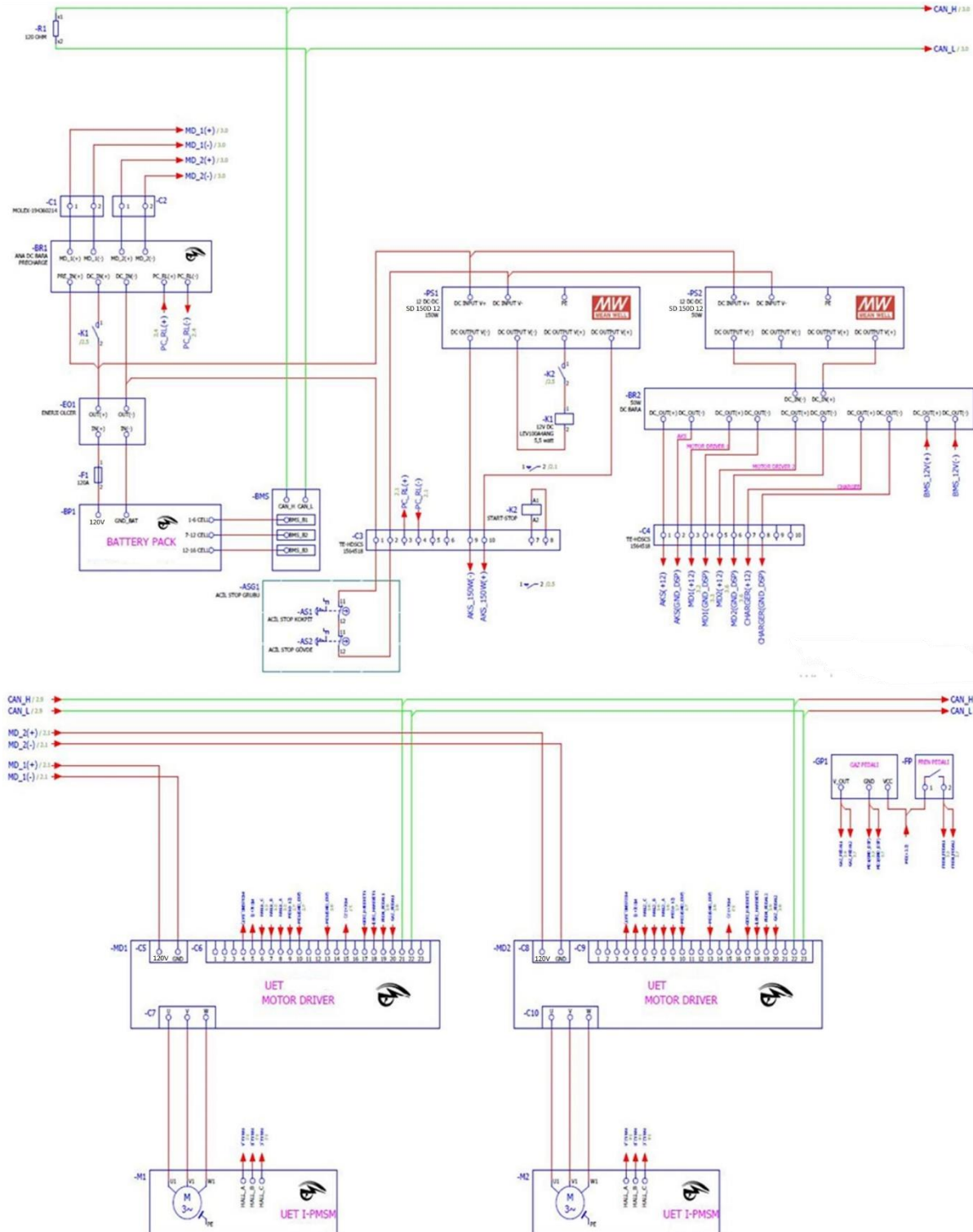
$$V = 8,2 \text{ m/s}$$

$$= 29,73 \text{ km/h}$$

## 16. Fuel Cell

## 17. Fuel Cell Control System

## 18. Vehicle Electric Scheme



## 19. Unique Design by Team

### 19.1. Control Arm Made of Metal Reinforced Composite Material

One of the most expected parameters in electric vehicles is efficiency. The most important factor affecting efficiency is weight. In the automotive industry, weight reduction works are carried out without compromising the structural expectations of the parts on the vehicle. In this study, a control arm design and production made of composite material with high strength/lightness ratio has been made. Composite materials generally consist of binders and reinforcing elements. In this study, aluminum is used as a metal material, and epoxy resin and carbon fiber fabric is used as binder.

When the expectations of composite material are compared, it is seen that it can be used easily without mechanical expectation especially in external visual parts, but it is less used for structural parts. It has been seen in literature research that structural expectations can be met by using reinforced materials.

In this study, the upper control arm in the rear tool was designed and manufactured with composite material. The present upper control arm is shown in the Figure 19.1. In the present design, the control arm is made of aluminum. The aluminum reinforced composite control arm is shown in the Figure 19.2. In this design, aluminum sheets are laid between carbon fiber fabrics. While the main body has a composite structure, the bushing regions are decided to be aluminum. The connection of the bushings with the main zone is made by mechanical bolted connection.

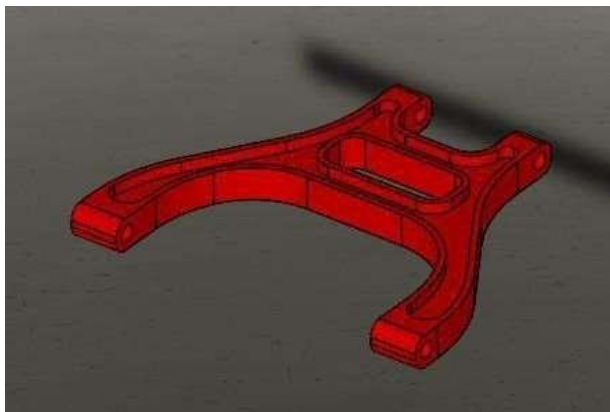


Figure 19.1. Control arm design available.

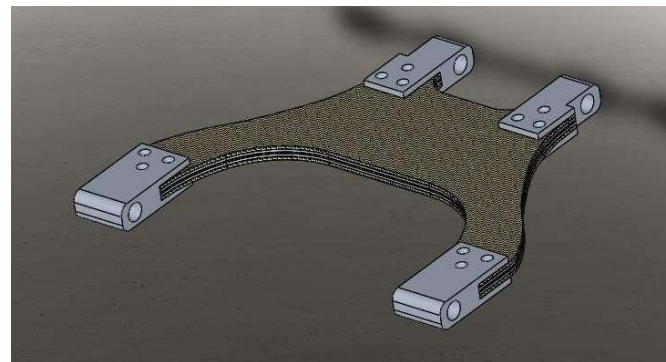


Figure 19.2. Control arm designed from composite material.

The thickness of the aluminum sheet material used is 1.5 millimeters. Two layers of sheet metal were used as reinforcement.

Material information is needed to construct a finite element model of composite design. Figure

19.3 shows the mechanical properties of the carbon fiber material. Carbon fiber fabrics react differently to the longitudinal and transverse forces. For linear static analysis, it is sufficient

to enter the poison ratio, elastic modulus and density of the material. These three properties are used for the finite element model.

Parameter	Value
Density $\rho$ [Kg/m <sup>3</sup> ]	1750
Longitudinal Young's modulus $E_L$ [GPa]	230
Transverse Young's modulus $E_T$ [GPa]	40
Transverse Poisson ratio $\nu_{TT}$ [-]	0.2
Longitudinal-transverse Poisson ratio $\nu_{LT}$ [-]	0.256

Figure 19.3. Properties of carbon fiber material.

<i>Material</i>	Tensile Strength (GPa)	Tensile Modulus (GPa)	Density (g/ccm)	Specific Strength (GPa)
Standard Grade Carbon Fiber	3.5	230.0	1.75	2.00
High Tensile Steel	1.3	210.0	7.87	0.17

Figure 19.4. Comparison of carbon fiber and steel.

In Figure 19.4, the material properties of a standard grade carbon fiber compared to steel were compared. It is seen that carbon fiber material is very low in density and high in resistance.

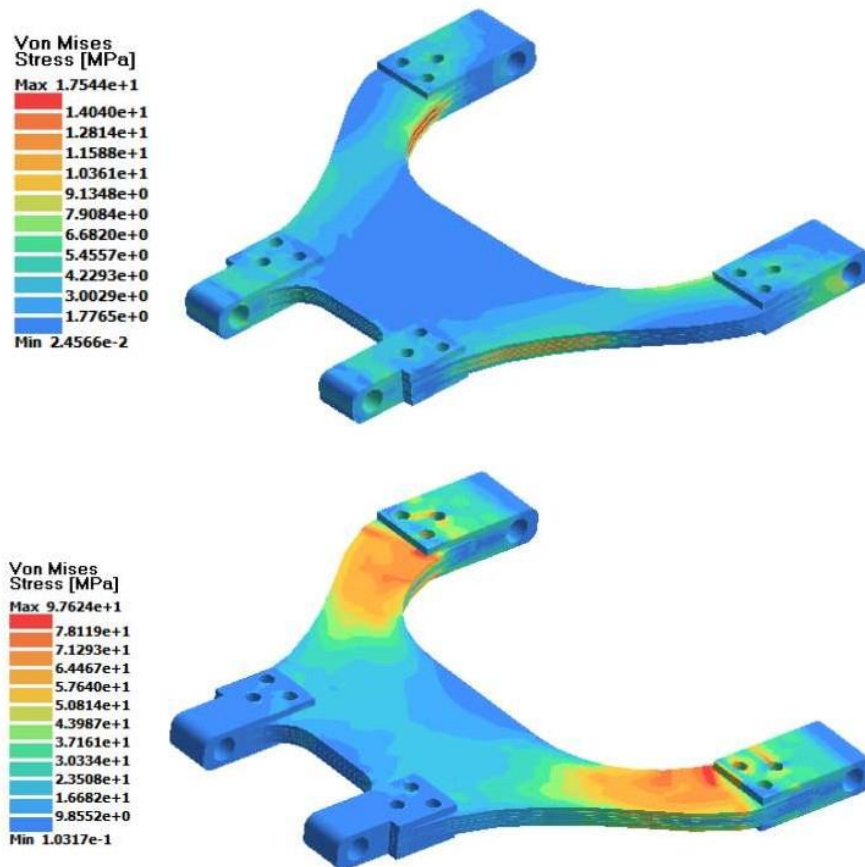


Figure 19.5. Stress distribution of the composite control arm.

Stress values were determined by the control arm to the force in the bending and pulling directions. In Table 19.1, these values are compared with the aluminum control arm.

Table 19.1. comparison of aluminum and composite control arm.

	<b>Weight (gram)</b>	<b>Bending Stress (Mpa)</b>	<b>Tensile stress (Mpa)</b>
<b>Control arm design available</b>	430	96.29	10.4
<b>Control arm designed from composite material</b>	390	97.6	17.5

As shown in Table, it is understood that the composite control arm is 10% lighter than the previous design and there is no significant loss in resistance.

The realization of the design started with the cutting of 500x600 mm wide carbon fiber fabric and aluminum sheets. The cut fabric and aluminum sheets are laid one by one according to the design sequence as shown in figure 19.6.

As shown in Figure 19.7, perforations are made on the aluminum sheets. The reason for this is to gain weight and to epoxy resin transfer to the surface between other surface. At the

same time, the roughness of the surface of the aluminum sheet is ensured by scratches in order to prevent any slip effect.

When the manual tilting process was completed, the composite plate was subjected to hot air for curing and hardening of the epoxy resin and left under pressure for 1 day. This flat plate was then cut with the help of water jet in accordance with the final form. Finally, the production was completed by mounting the bushings to the composite main body on the vehicle.



Figure 19.6. Manually tilting the carbon fiber fabric.



Figure 19.7. Tilting the metal reinforcement.

This study was performed for the upper rear wishbones of the vehicle as well as the front upper wishbones. A total of 4 metal reinforced composite control arms were produced, resulting in a 10% reduction in weight compared to the old control arms.

## 19.2. Energy meter

The energy meter reads the battery voltage and current drawn in isolation from the battery. With these read data, it calculates the power drawn and the energy consumed by the vehicle. It logs the energy consumed via RTC to the SD card. It communicates with the vehicle via CAN communication. It displays the instantaneous current drawn, the total voltage of the battery, the instantaneous power and the energy consumed on the screen. It gives a warning to the driver when excessive current is drawn. It has 0.2% voltage and current accuracy. It was used as the original design in this vehicle. The schematic and PCB files are attached as pdf files.

Features of the card:

- Isolated CAN Communication,
- Isolated Voltage and Current Measurement,
- Internal RTC,
- SD card for logging,
- 1.3inc I2C OLED Display,
- External isolated UART Communication with PC

### 19.2.1. Microcontroller Selection

STM32F373C8T6 produced by STMicroelectronics is used. STM32F373C8T6 is especially preferred because it contains 16-bit sigma-delta ADC.

Its main features are:

- 3 x 16 Bit sigma-delta ADCs,
- 12 Bit ADCs with 1 MSPS,
- Up to 2 x comparators,
- Up to 3 x 12 Bit DACs,
- 1 x CAN 2.0B,
- 1 x USB 2.0,

### 19.2.2. Isolated Voltage and Current Measurement

In the designed circuit, the current was calculated from the voltage falling on the shunt resistor. The battery voltage was measured with voltage divider resistors. AMC1301 is used for current measurement and AMC1311 is used for voltage measurement. The gain of the AMC1301 operational amplifier is  $A_v = 8.2$  and gain of the AMC1301 operational amplifier is  $A_v = 1$ . The AMC1301 and AMC1311 output an offset 1.44V output signal. It reads differential input from two channels with the sigma-delta ADC inside the microcontroller. It takes the difference of the two channels it reads and converts it to a 16-bit number. In voltage and current measurement, positive and negative polarity signals can be read. Thus, it can be determined which of the production and consumption modes of the vehicle.

Transfer function of the current sense circuit;

$$V_{out} = (I \times R_{shunt}) \times 8.2 \quad (15.1)$$

$$V_{out} = (I \times 500\mu\Omega) \times 8.2 \quad (15.2)$$

The circuit diagram of the current sense circuit was shown in Figure 19.8.

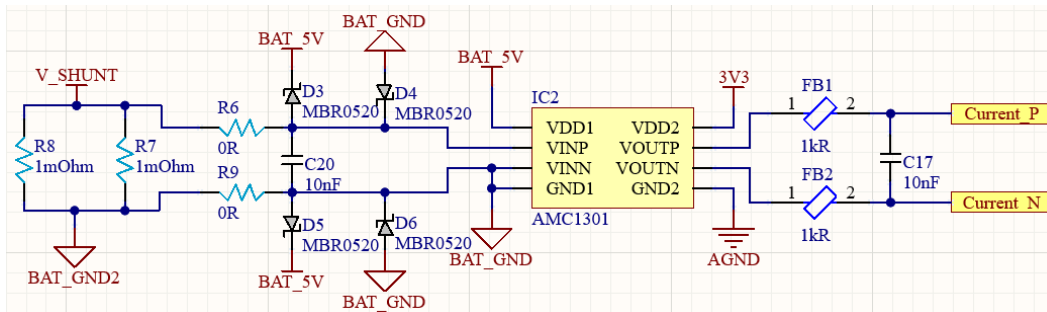


Figure 19.8. Circuit Schema Of The Isolated Current Sense

Transfer function of the voltage sense circuit;

$$V_{bat} = V_{out} \times \frac{(10k\Omega + 1M\Omega)}{10k\Omega} \quad (15.3)$$

The circuit diagram of the voltage sense circuit was shown in Figure 19.9.

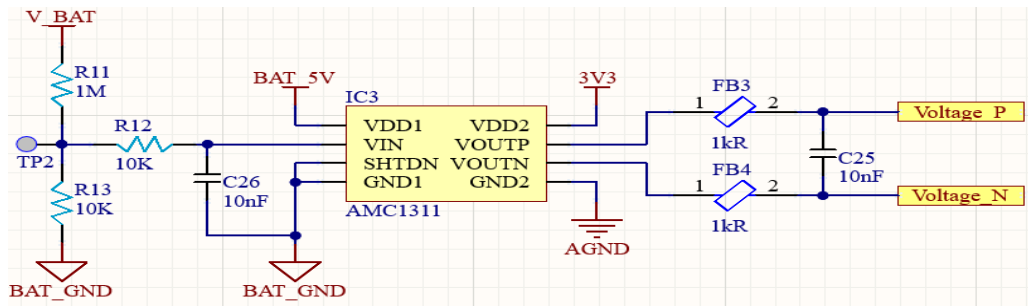


Figure 19.9. Circuit Schema Of The Isolated Voltage Sense

In order for the measured signal to be affected by electrical noise as little as possible, filter coils are used as LC low-pass filters. Analog and digital GNDs are connected to each other as a star connection with the help of a 0R resistor.

### 19.2.3. Isolated Power Supply for OPAMPs

SN6505 transformer driver, isolated 760390012 SMPS transformer and TPS76350-Q1 voltage regulator are used for isolated supply for AMC1301 and AMC1311. The power supply circuit diagram set up to read the battery voltage and current in isolation from the battery is shown in Figure 19.10.

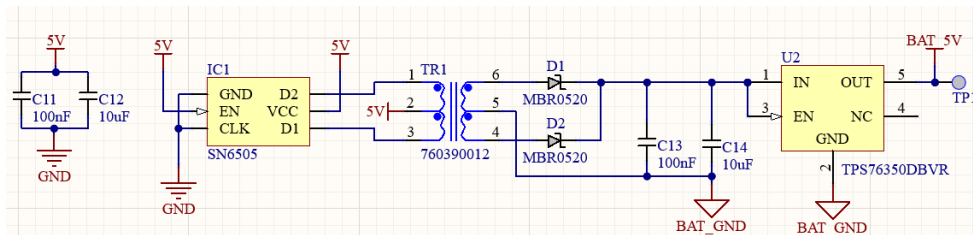


Figure 19.10. Isolated Power Supply for OPAMPs

### 19.2.4. DS3231 RTC and SD Card

RTC and SD card are used to calculate energy and keep logs. The power draw is calculated by multiplying the measured battery voltage and current. The energy consumed is calculated by integrating the power absorbed. The 4 calculated data are saved in the SD card by adding the time and date. If the system does not see the SD card at boot, it does not log. In the program, data is written to the SD card every 250ms by adding time and date information. The circuit diagram for logging is in Figure 19.11.

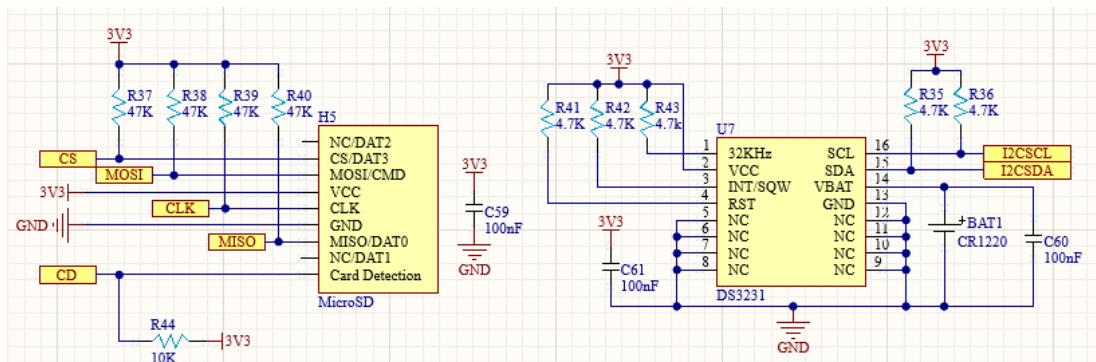


Figure 19.11. DS3231 RTC and SD Card Schema

When the logging process is finished, the .txt file created with the help of the excel program is opened. The “\*” sign is used as a separator. Excel divides the typed data into columns. If desired, these data can be graphed. Below is an example Energy-Time graph created in Figure 19.12.

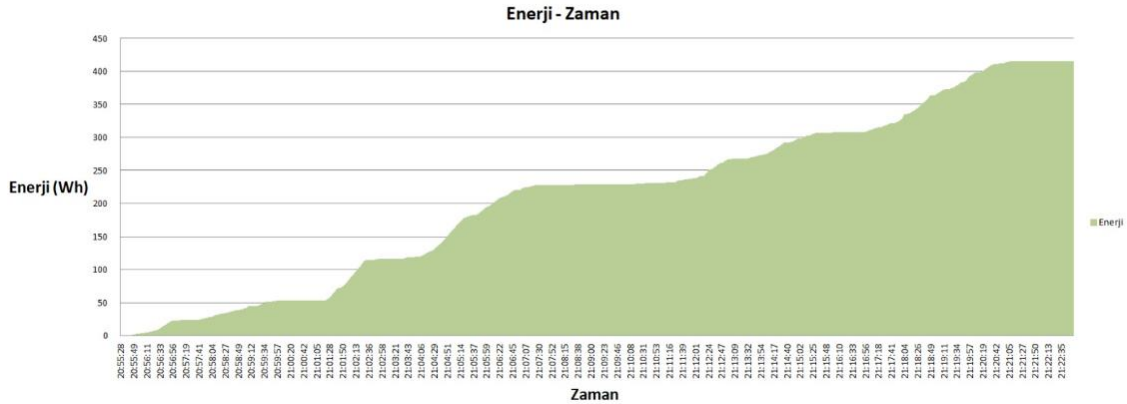


Figure 19.12. Energy-Time Graph

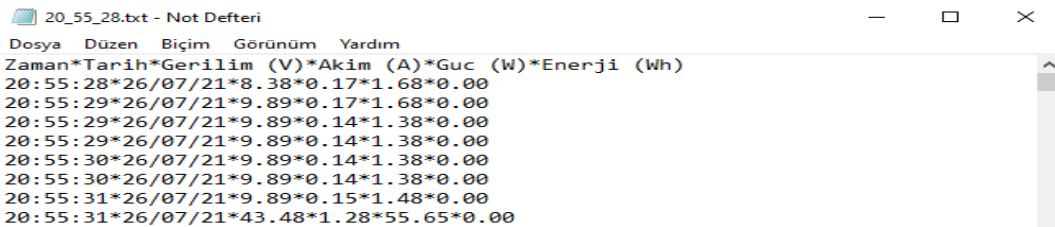


Figure 19.13. Created .txt file

### 19.2.5. Isolated UART Communication

All cards in the vehicle control system also communicate with the PC with the CH340 USB to UART converter on them. ADUM1201 UART isolator IC is used to provide isolation between vehicle and PC. Isolated UART communication circuit is shown in figure 19.14. VCU main board, VCU I/O board and energy meter use the same UART communication circuit.

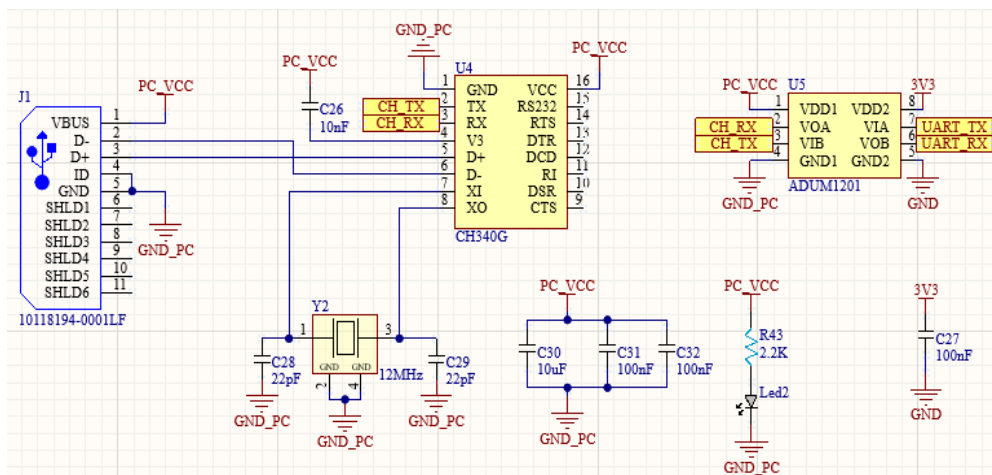


Figure 19.14. Isolated UART Communication

### 19.2.6. Regulators

To be used in the energy meter card, a 5 Volt output was obtained with the MP1482 buck converter from the 12 Volt input. The 5 Volt output from the MP1482 buck converter has been reduced to 3.3 volts with AMS1117-3.3 for the supply of the processor and other components. The mentioned regulator circuit schematic is shown in Figure 19.15.

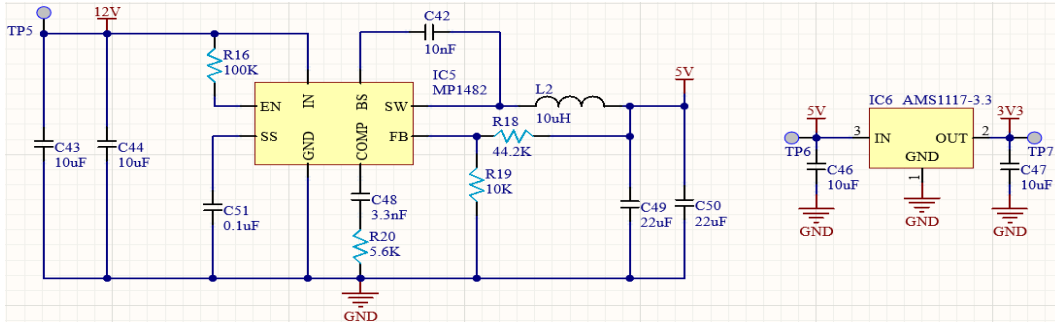


Figure 19.15. Regulator circuit

### 19.2.7. Control Algorithm

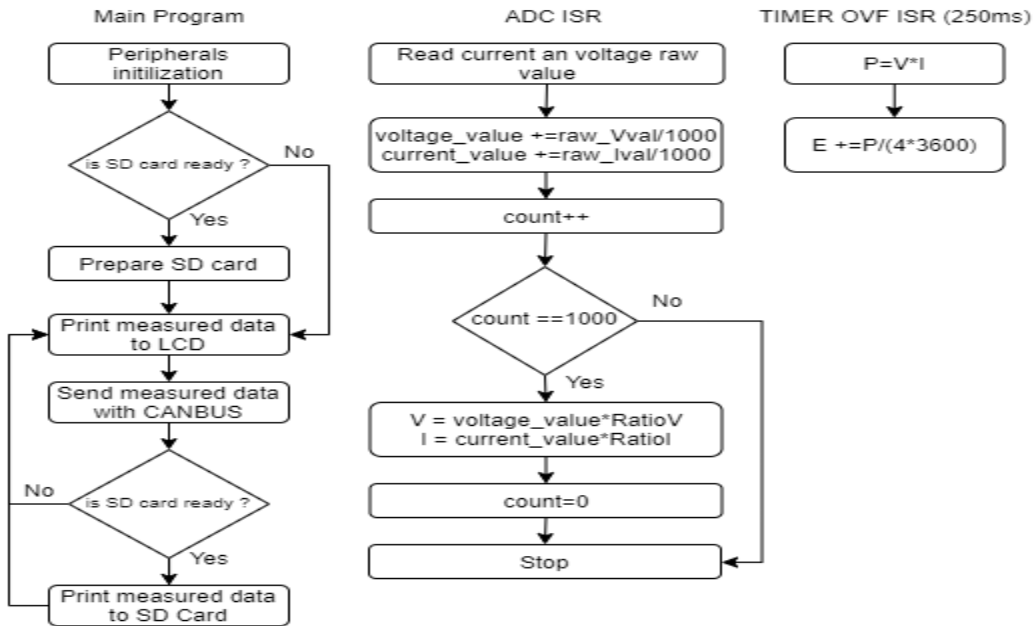


Figure 19.16. Energy meter control algorithm

## 19.2.8. Production Studies

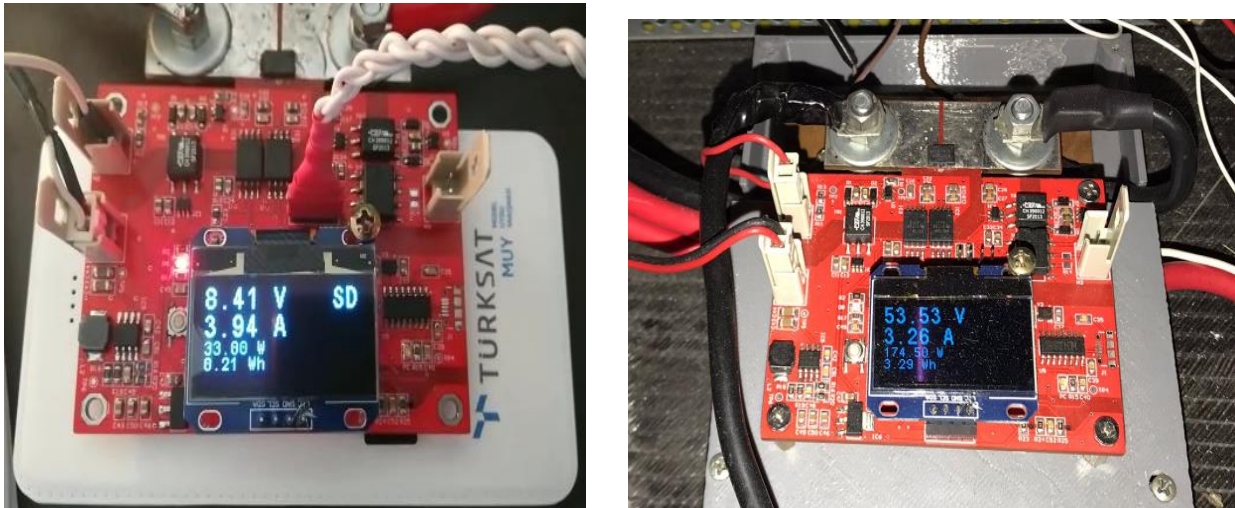


Figure 19.17. Energy Meter

<https://we.tl/t-6e7zJIUjJM>

### Comparison Table

		Previous Design	Current Design
VCU Functions	:	Telemetry ,I/O	Telemetry, I/O, Energy meter
Controller IC	:	Isolated I/O Card	Isolated I/O Card
VCU I/O Count	:	15	16
Electronic Circuit Design	:	Altium Designer	Altium Designer
PCB Card Design	:	Altium Designer	Altium Designer
PCB Card Supplier	:	JLCPCB	JLCPCB
Software Algorithm	:	STM32CUBEIDE , C Language	STM32CUBEIDE , C Language
Experimental Study	:	-	-
Dimension (PCB / Kutu)	:	100 mm/85 mm	100 mm/90 mm

### 19.3. Cost Calculation

Product	Quantity	Unit	Unit Piece	Ammount
Motor	2	Piece	₹2.500,00	₹5.000,00
Motor Driver	2	Piece	₹3.000,00	₹6.000,00
Embeded Recharcing Unti	1	Piece	₹2.000,00	₹2.000,00
Battery Management System	3	Piece	₹350,00	₹1.050,00
Vehicle Control Unit	1	Piece	₹2.000,00	₹2.000,00
Battery	256	Piece	₹80,00	₹20.480,00
Chassis	30	Kilogram	₹20,00	₹600,00
Body	1	Piece	₹18.000,00	₹18.000,00
Brake System	1	Piece	₹1.200,00	₹1.200,00
Steering Wheel System	1	Piece	₹1.500,00	₹1.500,00
Shock Absorber	6	Piece	₹300,00	₹1.800,00
Harness	1	Piece	₹100,00	₹100,00
Rim	6	Piece	₹500,00	₹3.000,00
Racing Seat	2	Piece	₹3.500,00	₹7.000,00
Diffuser	1	Piece	₹1.000,00	₹1.000,00
			<b>Total</b>	<b>₹70.730,00</b>